Department of Physics

University of Strathclyde

Micro-transfer printing for visible light communications applications

Katherine Jeanne Rae

A thesis presented in fulfilment of the requirements for the degree of Doctor of Philosophy

December 2017

This thesis is the result of the author's original research. It has been composed by the author and has not been previously submitted for examination which has led to the award of a degree.

Frontispiece

Figure 1: A single μLED micro-transfer printed onto 30 μm-thick mechanically flexible glass.

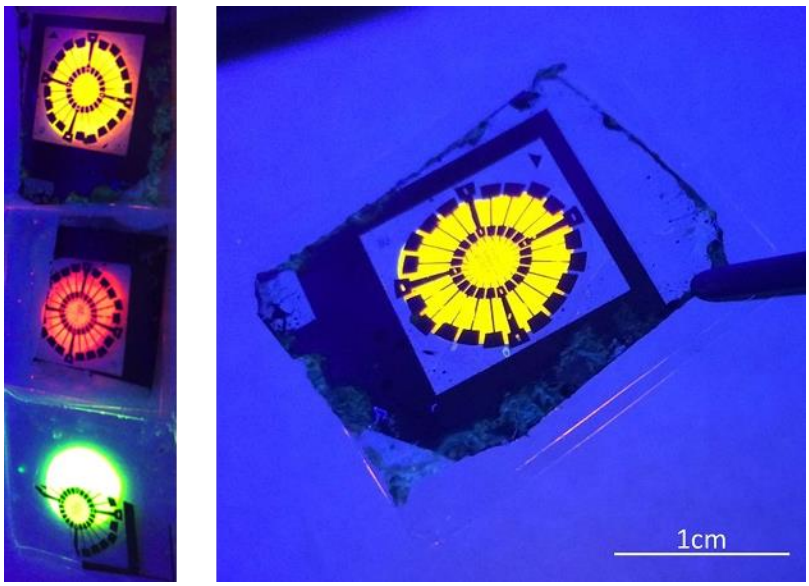

Figure 2: μLEDs integrated with colloidal quantum dot colour converters, illuminated with UV light.

Abstract

The work presented in this thesis focuses on the transfer printing of InGaN-based blue-emitting light emitting diodes (LEDs) onto various non-native substrates for visible light communications applications. The controlled mechanical integration of photonic structures onto non-native substrates using micro-transfer printing (μTP) techniques is paving the way to high-performance, heterogeneous and multi-functional integrated photonic devices.

2μm-thick 100μm x 100μm LEDs are transfer printed onto these non-native, capability-enhancing, substrates using a modified nano-lithography system. Blue-emitting μLEDs in this thin, transfer printable format, were integrated into an array of green-emitting μLEDs to create a dual-colour μLED on a single chip. This chip is then electrically and optically characterised and demonstrated to examine its potential for data communications applications. The same blue-emitting μLEDs are also integrated with colloidal quantum dot (CQD) colour-converting structures. This yields integrated red, green and orange colour-converting structures all pumped by the blue-emitting transfer printed μLEDs. The μTP technique is finally used to fabricate an integrated optical transceiver device.

Acknowledgements

This PhD has been incredibly fun, and one of the best things I have done and I am certain I would never have completed it, or got so much out of it without the support of the people I need to thank here! I would like to firstly acknowledge my supervisor, Professor Martin Dawson, for giving me the opportunity to do my PhD at the IoP and for all his guidance and encouragement. This is something I will always be grateful for. I must also acknowledge my funding from EPSRC (EP/K00042X/1).

I would also like to thank my second supervisor, Dr Nicolas Laurand for all his help and support throughout my time here, you have always been such a great supervisor.

In particular, I would like to thank Dr Benoit Guilhabert, Dr Enyuan Xie, and Dr António Trindade. Everything I know about cleanroom fabrication, transfer printing and LEDs I have learned from the three of you! Thank you so much for taking the time to teach me and support me over the past four years, your encouragement has really been invaluable.

I would like to acknowledge the help I have had from Dr Tony Kelly, Dr Scott Watson, and Shaun Viola at Glasgow University with modulation bandwidth measurements. A big thanks must also go to Mohamed Islim and Eric Yin at the University of Edinburgh for all their help with data transmission measurements, especially when working with challenging devices like mine! Also, to Dr Pavlos Manousiadis, for working with me on the optical transceiver, thank you. Thank you to Dr Jonathan McKendry for your support with all of these measurements and device characterisation.

Chapter 0. Acknowledgements

Thank you to all the students and staff at the IoP, this really has been such a great experience and the IoP is full of wonderful, inspiring people and I wish you all success in whatever you do and thank you for everything. I have made some great friends here, in particular Giuseppe Cantarella and Luke McLellan: thanks for all the chats and fun times over the past 4 years. To Dr Brynmor Jones, I will miss our chats over countless teas. Also Paul Hill, you have made this PhD so fun - thanks for all the teas, trivia, emotional support and cruciverballing!

A huge thank you to Dr Caroline Foucher, I really could not have done this without your support and friendship, Je miss you!

Most importantly, I need to thank my friends and family. Without your love and unconditional support this would never have happened. To Becky, Roddy, Sarah, and Marieke, I am so glad we have all been doing our PhDs together, you have made this an incredibly fun four years and I know you are going to do amazingly! Thanks to Tommy, Sukie and Granny for your support and interest in my PhD, I will always be so grateful to have you as my family. To Gábor: thank you for being there even when I have been a stressy mess, szeretlek. Finally Mum, Dad and Susie: you are the people who have made me who I am, who have been there for every emotional crisis and drama throughout this PhD and my entire life. You inspire me, are my constant supporters, and I love you. Thank you.

List of Figures

List of Figures

List of Figures

List of Figures

List of Figures

List of Figures

List of Figures

Abbreviations

$\mathbf{a_0}$	Lattice constant
AC	Alternating current
AFM	Atomic force microscopy
APD	Avalance photodiode
B	Bimolecular recomination coefficient
BER	Bit error rate
BW	Modulation bandwidth
CQD	Colloidal quantum dot
DC	Direct current
e	Electronic charge
$\mathbf{E_C}$	Conduction band energy
$\mathbf{E_F}$	Fermi energy level
$\mathbf{E_g}$	Material bandgap
EQE	External quantum efficiency

$\mathbf{E_V}$	Valence band energy
$\mathbf{eV_D}$	Potential barrier
$\mathbf{f}/\nu/\omega$	Frequency
FEC	Forward error correction
h	Planck's constant
ICP	Inductively coupled plasma
IFFT	Inverse fast Fourier transform
IQE	Internal quantum efficiency
IV	Current-voltage
k	Boltzmann's constant
L or l	Length (or width of quantum well)
λ	Wavelength
LED	Light-emitting diode
m	Mass
$\mathbf{m^*}$	Effective mass
μ**LED**	Micro-LED
μ**TP**	Micro-transfer printing
MOCVD	Metal organic chemical vapour deposition
MOVPE	Metal organic vapour phase epitaxy
MQW	Multiple quantum wells

n	Electron concentration or refractive index
NA	Numerical aperture
NLP	Nanolithography probe
OFDM	Orthogonal frequency division multiplexing
OOK	On-off-keying
p	Hole concentration or momentum
PAM	Pulsed-amplitude modulation
PDMS	Polydimethylsiloxane
PET	Polyethyleneterphalate
POF	Polymer optical fibre
PR	Photoresist
PSS	Patterned sapphire substrate
QAM	Quadrature amplitude modulation
RF	Radio frequency
RIE	Reactive ion etch
SEM	Scanning electron microscope
SOI	Silicon-on-insulator
SNR	Signal-to-noise ratio
T	Temperature

τ	Carrier lifetime
VCSEL	Vertical cavity surface emitting laser
VLC	Visible light communications
$\mathbf{V_D}$	Turn-on voltage
WDM	Wavelength division multiplexing

Contents

Contents

Chapter 1

Introduction

1.1 Motivation and aims

In this chapter, the background and motivations of this thesis are initially presented. The work involves the transfer printing of blue-emitting indium gallium nitride (InGaN) light - emitting diodes (LEDs) onto various unconventional substrates for visible light communications (VLC) applications. Transfer printing means the LEDs are no longer constrained by the properties of their growth substrate and we can instead tailor-make substrates to give the LED the capability we desire. InGaN-based LEDs will therefore be introduced in this chapter. The history and invention of high efficiency LEDs will be discussed, with a focus on the emergence of the blue InGaN-based LED and how these devices have impacted our world in the years since their production began. The physics behind LEDs will then be discussed, and the pn junction and charge transport in LEDs introduced, before discussing how the introduction of more complex heterostructures such as multiple quantum wells impacted LED technology. The chapter will end by introducing visible light communications (VLC) and discuss how LEDs are used in this exciting, emerging field.

1.2 Light-emitting diodes (LEDs)

The LED was first discovered by H. Round in 1907 when he noticed that a silicon carbide (SiC) crystallite would emit light when contacted with two electrodes [1]. LEDs based on III-V semiconductors were then commercialised in the 1960s with red emission (based on gallium arsenide phosphide (GaAsP)) and green emission (based on gallium phosphide(GaP)) [2, 3] and became widely used as indicator lights, and as screens in pocket calculators and watches. These red and green (as well as orange) LEDs became more advanced as technologies improved and it became important to produce similarly high efficiency blue LEDs going beyond the inefficient SiC blue devices that were first introduced. This would allow light across the visible spectrum - and crucially white light - to be produced by mixing light from different LEDs.

Plagued by difficulties in growing good quality gallium nitride (GaN) films, as well as in achieving p-type GaN, progress to produce blue-emitting LEDs with the III-Vs virtually ceased from the mid 1970s. High power and efficiency blue-emitting LEDs therefore proved elusive, until work was done by scientists in Japan to produce the first high efficiency blue-emitting LEDs (for which S. Nakamura, H. Amano and I. Akasaki won the Nobel prize in Physics in 2014 [4]). While the rest of the field had given up, they continued to believe that GaN held the key to the production of highly efficient blue-emitting LEDs. Problems with growing good quality GaN were solved by metal organic vapour phase epitaxial (MOVPE) growth combined with an AlN buffer layer to reduce the effects of lattice mismatch between GaN and the sapphire substrate [5]. Magnesium (Mg) doping, activated by either electron beam treatment or thermal annealing, became the solution to growing p-type GaN [6], and in 1994 the first high-brightness blue-emitting LED was produced by Nakamura at Nichia Chemical Industries Ltd in Japan [7].

Since the invention of blue-emitting LEDs in the mid 1990s, much work has been done to improve the performance of LEDs for various applications, further developments

including the introduction of InGaN ternary alloy structures and multiple quantum well (MQW) active regions. There are two important parameters for assessing the performance of an LED: internal quantum efficiency (IQE or η_{int}) and external quantum efficiency (EQE or η_{ext}). The IQE is defined as the number of photons emitted by the LED per the number of injected charges. As will be discussed later, charges in semiconductors can combine either radiatively (with the release of a photon) or non-radiatively (with energy released as heat). The IQE is therefore a ratio of the radiative and non-radiative recombination:

$$\eta_{\text{int}} = \eta_{\text{inj}} \times \eta_{\text{r}} = \frac{P_{\text{int}}/h\nu}{I/e} \tag{1.1}$$

where P_{int} is the emitted optical power from the active region, I is the injected current, and e the electronic charge. Here, η_{inj} and η_r are the electron injection efficiency and the radiative efficiency, respectively. The latter defines the rate at which radiative recombination occurs, and can be described using the following:

$$\eta_{\text{r}} = \frac{Bn^2}{An + Bn^2 + Cn^3} \tag{1.2}$$

Here A, B, and C are the coefficients associated with Shockley Reed Hall (SRH) recombination, spontaneous radiative recombination, and Auger recombination, respectively. The SRH and Auger recombinations are both non-radiative. In this equation, n denotes the carrier density.

It is important to note here that, while true at low current densities, Equation 1.2 does not completely describe the radiative and Auger recombination rates at high current density. In this case, the B and C coefficients can be described by Equation 1.3 and Equation 1.4. In these, n^* is a fitting parameter common between them [8].

$$B = \frac{B_0}{1 + \frac{n}{n^*}} \tag{1.3}$$

$$C = \frac{C_0}{1 + \frac{n}{n^*}} \tag{1.4}$$

The IQE can also be described in terms of the radiative and non-radiative lifetimes:

$$\eta_{\text{int}} = \frac{{\tau_{\text{r}}}^{-1}}{{\tau_{\text{r}}}^{-1} + {\tau_{\text{nr}}}^{-1}} \tag{1.5}$$

where τ_{r} is the radiative lifetime and τ_{nr} is the non-radiative lifetime.

In real devices, not all photons generated in the active region are emitted, with some being trapped internally by total internal reflection or re-absorptions in either the device substrate or metal contacts. The external quantum efficiency (EQE) is defined as the number of photons emitted into free space by the LED compared to the number of injected charge carriers. It can be expressed as:

$$\eta_{\text{ext}} = \eta_{\text{int}} \times \eta_{\text{extraction}} \tag{1.6}$$

where,

$$\eta_{\text{extraction}} \approx \sum_{b=1}^{\infty} \frac{1}{2}(1-T)^{\text{b-1}} T\left[R_m^{b-1} + R_m^b\right] \tag{1.7}$$

Here $\eta_{\text{extraction}}$ is the light extraction efficiency. According to Equation 1.6, the light extraction efficiency is the ratio of the number of photons emitted into free space to the number of photons generated within the active region of the LED. Equation 1.7 is based on a mathematical model for random light emission [8]. The b term represents number of times a light ray is reflected at the exit surface and bounces around within a device before being emitted. T is the transmission coefficient of the exit surface (in

this case at the interface with air) and R is the refelection coefficient of the substrate. The model assumes we only want light emission in one direction - through the LED/air interface rather than through the substrate. Several techniques are employed during device design to increase the EQE of LED. Most commonly this involves roughening or patterning the substrate surface to reduce the probability of total internal reflection within the LED [9–11]. The model [8] which gives us equation 1.7 assumes the substrate has been roughened such that total internal reflection becomes impossible and light will always either escape the LED (at the interface with air) or be absorbed by the substrate.

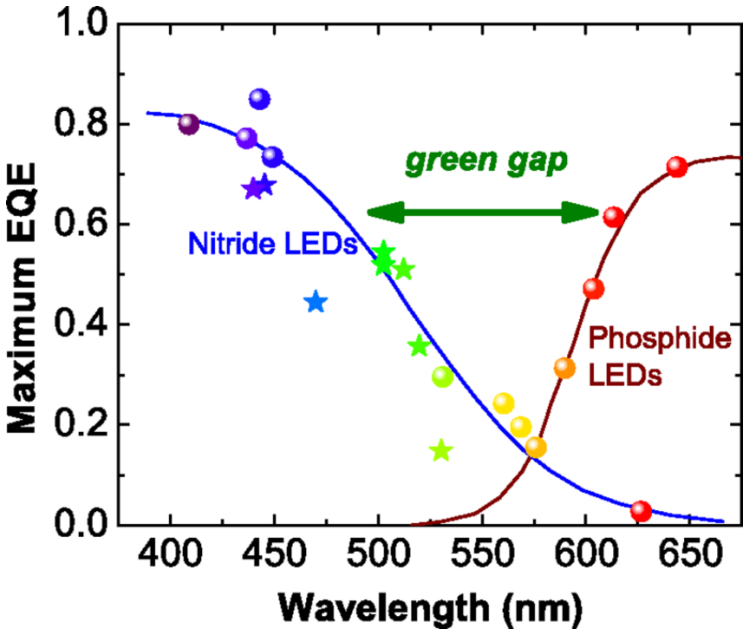

Figure 1.1: EQE versus peak wavelength for InGaN and AlInGaP LEDs. Image from [12]

Figure 1.1 shows the EQE of various commercial LEDs versus peak wavelength, as reported by Auf Der Maur et al. in 2015. In the yellow-green wavelength region, where the eye is most sensitive, the EQE is relatively low and a lack of high power LEDs in this range is dubbed the "green-gap".

The production of bright, efficient, and cheap red, green, and blue LEDs has resulted in them now being used in almost every sector of technology, some examples of which can be seen in Figure 1.2. While still used as simple indicator lights, we now see LEDs

Figure 1.2: Some applications of LEDs. Shown here are light bulbs, headlights, indicator boards, and LEDs used as display backlights. Images from [13–16]

.

in displays, car headlights, room and street lighting as well as in medical applications [18–21].

One of the most important uses for LEDs is for white light illumination, known as "solid state lighting", which is paving the way for energy efficient, low cost lighting. Figure 1.3 shows the increase in efficiency between such solid state lighting and other, less efficient, forms of lighting. In this figure, the different lighting types are compared in terms of luminous efficacy in lumens (lm) per watt (W) where a lumen is the unit of luminous flux (the optical power as perceived by the human eye, see Figure 1.1) - luminous efficacy is the amount of light per unit of electrical power. In 2014, Cree Inc. reported an LED bulb with a luminous efficacy of over 300 lm/W [22], a huge improvement on incandescent lamps with a tungsten filament (under 20 lm/W) and fluorescent lamps which tend to have luminous efficacies under 100 lm/W. Commercial white LEDs nowadays routinely have a luminous efficacy of between 100 lm/W and 200 lm/W [23]. Solid state lighting sources also tend to last much longer than incandescent

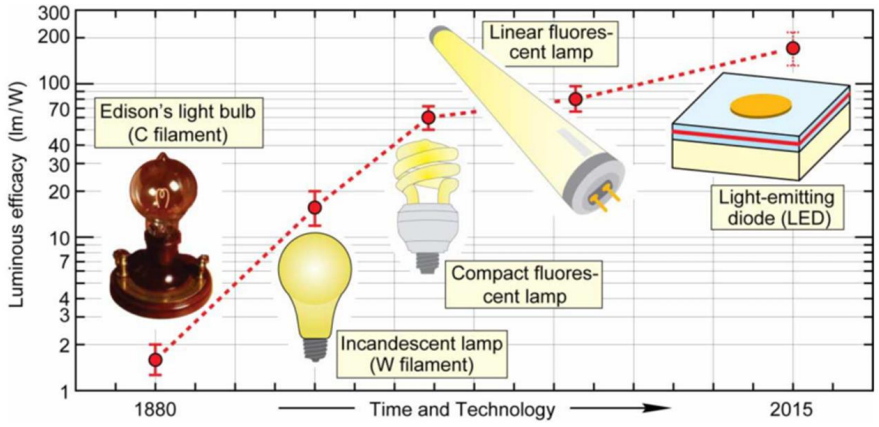

Figure 1.3: Comparison of the energy efficiency of several different types of lighting. Image from [17]

.

tungsten filament light bulbs - 35,000 hours compared to 1000 hours.

With lighting typically accounting for 15% of domestic energy consumption [24], increasing the effiency of lighting sources is important for reducing energy consumption and greenhouse gas production. Replacing conventional light bulbs with solid state lighting is predicted to save 1.9 x 10^{20} J of energy over a ten year period. It will also massively reduce CO_2 emissions, as well as reducing the emission of other harmful pollutants like sulphur dioxide (SO_2)(which causes acid rain), uranium (U), and mercury (Hg)(which is used in other energy saving bulbs and fluorescent strip lights) [17]. It is also predicted to reduce crude oil consumption by 962.4 x 10^6 barrels over the same 10 year time period [25]. The drive towards electrical efficiency and environmental sustainability has led to incandescent and halogen light sources being phased out, to be replaced with solid state lighting.

1.3 Semiconductors - Bandgap and the pn junction

LEDs are made from compound (usually group III-V) semiconductors, of which there are two main types: direct bandgap and indirect bandgap. The periodic arrangement

and size of atoms in a semiconductor leads to an electronic energy band structure consisting of a conduction band and a valence band separated by a bandgap (E_g). Free electrons, when present, can be found in the conduction band, while free holes are found in the valence band. In Figure 1.4, the conduction and valence bands are represented over the Brillouin zone, and the band diagram is therefore a plot of energy vs wavevector of the carriers (electrons) in a material.

When electrons and holes recombine across the bandgap, the excess energy E_g is released as either a photon - emitting light - or as lattice vibrations (phonons) - releasing heat. These conditions are known as radiative and non-radiative recombination respectively. As discussed in the previous section, Auger recombination is a third possibility: the transfer of energy into a third particle (e^- or h^+) but this will not be discussed here.

In a direct bandgap semiconductor, the conduction band minimum is directly above the valence band maximum (electrons and holes have the same k-vector (momentum)) and a direct radiative transition can occur, Figure 1.4 a). In an indirect bandgap semiconductor the conduction band minimum is not directly above the valence band maximum, and a photon is released along with a phonon in order to conserve momentum, Figure 1.4 b). Photonic applications favour direct bandgap semiconductors for efficient light emission and absorption.

In the case where an electron recombines radiatively with a hole to produce a photon, the photon energy (and therefore the wavelength of the photon) is determined by the energy released (E_g):

$$E_g = E_C - E_V \approx \frac{hc}{\lambda} \tag{1.8}$$

where E_C and E_V are the energy at the conduction and valence band edge respectively, h is Planck's constant, c is the speed of light, and λ is the wavelength of the emitted photon. Therefore, the colour of light emitted from an LED is dependent on the bandgap of the material it is made from. As discussed in the previous section, modern-

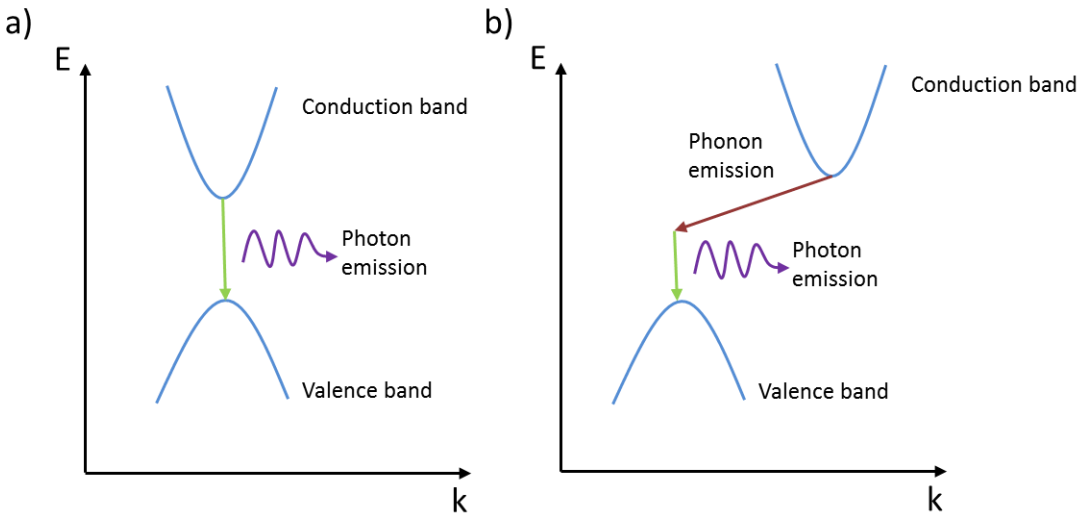

Figure 1.4: Schematic band diagrams of a) a direct bandgap and b) an indirect bandgap semiconductor.

day red-emitting LEDs are based on AlInGaP/GaAs, while blue-emitting LEDs are based on InGaN alloys, with bandgaps spanning the respective spectral regions.

Formation of alloys is generally possible between semiconductors with similar chemical and stuctural characteristics. The bandgap and lattice constant (size of the unit cell in a semiconductor material) of an alloy is intermediate between those of the parent binary compounds. Figure 1.5 shows the bandgap versus lattice constant of various common semiconductors. As we see in Figure 1.5, InP has a bandgap of 1.334 eV (corresponding to light in the IR region) and GaP has a bandgap of 2.26 eV (corresponding to green light). By changing the phosphorous concentration, the GaInP materials system can be used to emit light from red to yellow.

Similarly, GaN has a wide bandgap of 3.4 eV corresponding to an emission in the near UV, while InN has a bandgap which corresponds to emission in the near IR. By increasing the indium content, the InGaN materials system can be used to produce LEDs emitting from green/yellow to UV [27–29].

Intrinsic semiconductors contain no impurity atoms. Holes in the valence band are

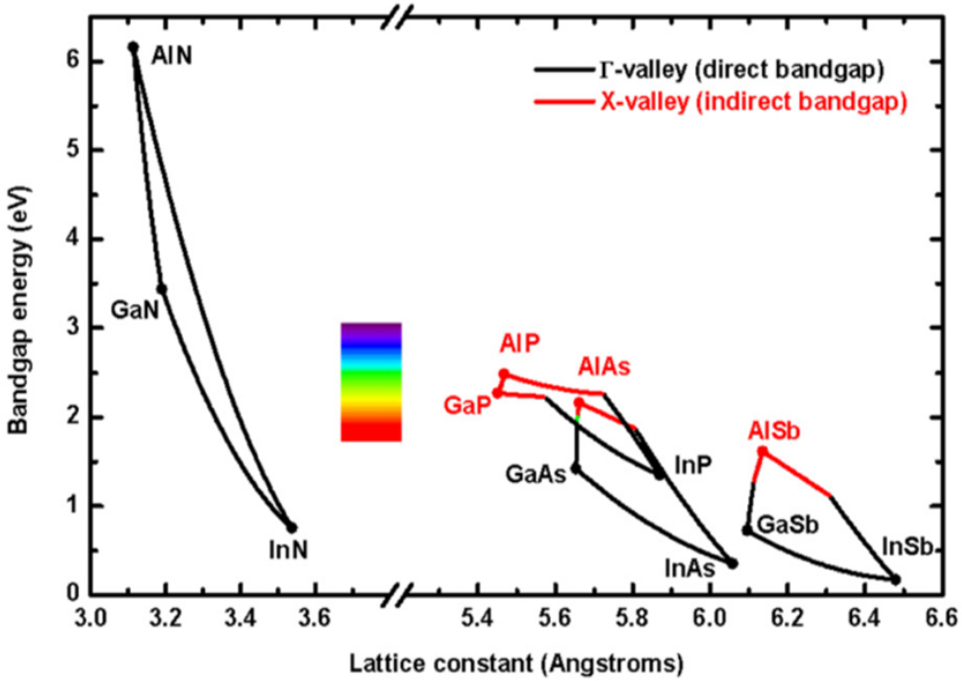

Figure 1.5: The bandgap with respect to lattice constant (in $\mathring{A}$, 10^{-10} m) of various common III-V semiconductors. Image from [26].

created when an electron is excited to the conduction band because of an input of energy (e.g thermal, optical). Under such excitation, the number of holes in the valence band is equal to the number of electrons in the conduction band and the semiconductor is neutrally charged. Intrinsic semiconductors therefore have relatively low conductivity.

To increase the conductivity of a semiconductor, impurity atoms called dopants are added to introduce extra charge-carriers into the semiconductor material. There are two types of dopant in semiconductors - n-type, where atoms with more valence electrons than the atoms in the semiconductor are added, and p-type, where atoms with fewer valence electrons than the atoms in the semiconductor are added. N-type dopants introduce electrons in the conduction band without introducing holes in the valence band, while p-type dopants introduce free holes in the valence band. Dopant atoms require the correct electron configurations to create states with appropriate energies in the bandgap of the host semiconductor. The dopant atoms must also fit the host semiconductor lattice with minimal disruption, so atoms from adjacent elements in the

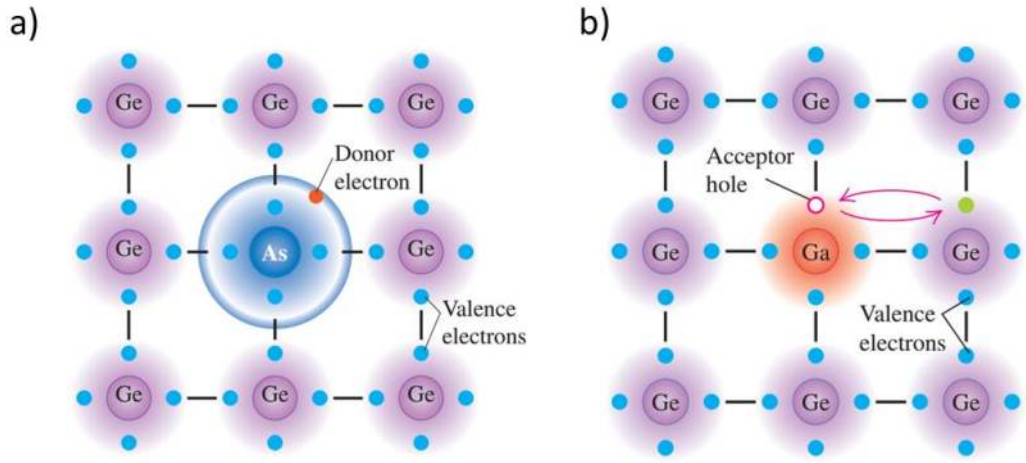

Figure 1.6: a) n-type doping, and b) p-type doping of germanium. Image from [30].

.

periodic table are preferred. For example, arsenic (As) is in group V of the periodic table and thus has five valence electrons. This acts as an n-type dopant and introduces extra electrons when added to germanium (Ge) which is in group IV of the periodic table and therefore has four valence electrons, Figure 1.6 a). Conversely, Ga acts as a p-type dopant in Ge as it is in group III in the periodic table and has three valence electrons and so creates a deficiency of electrons, introducing excess holes into the semiconductor, Figure 1.6 b). In GaN, as is used in the LEDs fabricated in this work, Si or Ge are typically used as n-type dopants with Mg used as a p-type dopant.

Semiconductors doped with n-type dopants (free electrons in the conduction band) are known as n-type semiconductors; semiconductors doped with p-type dopants (free holes in the valence band) are known as p-type semiconductors. The basis of an LED is the pn junction, which is formed at the interface between a p-type semiconductor and an n-type semiconductor. Electrons and holes recombine in an LED across the pn junction emitting photons. This will be discussed in the following section.

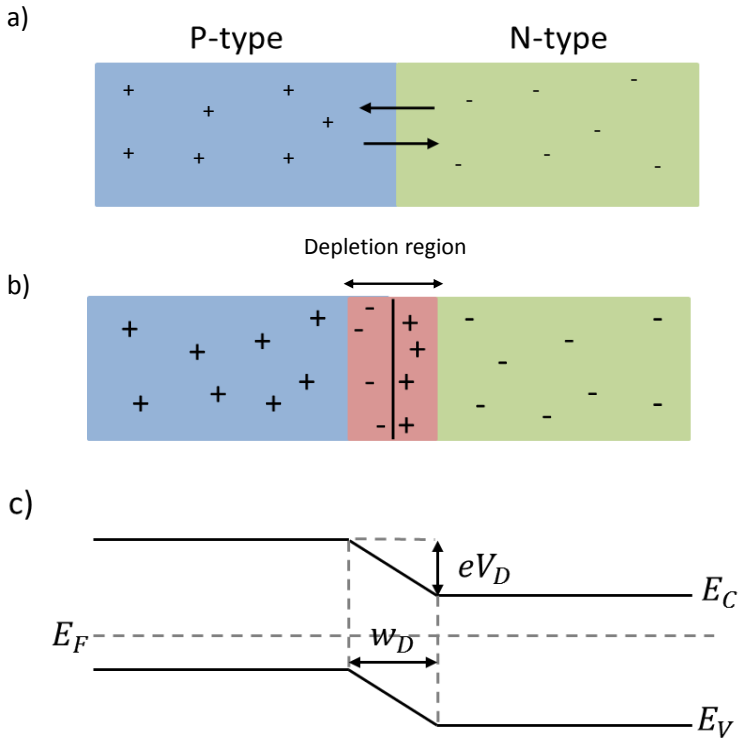

Figure 1.7: a) Schematic of the spatial configuration of a simplified pn junction, b) the pn junction under zero bias, showing the depletion region and c) the band diagram for the pn junction under zero bias, where the horizontal axis represents the distance perpendicular to the plane of the junction.

.

1.4 The pn Junction

As mentioned in the previous section, electrons and holes recombine either radiatively or non-radiatively across a pn junction in an LED. Clearly, for efficient light-emission, radiative recombination is required. Figure 1.7 shows the pn junction. When no bias is applied, there is a large excess of electrons in the n-type material and a large excess of holes in the p-type material. There is therefore a diffusion of electrons into the p-type region and similarly a diffusion of holes from the p-type region to the n-type. This leads to a region depleted of free carriers - the depletion region (shown in Figure 1.7 b)). With the absence of free carriers in this depletion region, the only carriers

that remain are those from p- or n-type dopants. These charges produce a potential across the depletion region (V_D) which is in the opposite direction to the electron and hole diffusion. In Figure 1.7 c) eV_D represents the potential barrier the charges must overcome to cross the depletion region, where e is the elementary charge.

Introducing a bias to the pn junction changes the magnitude of the potential barrier eV_D. Under reverse-bias this increases, further impeding the diffusion of charges. Under forward-bias however, eV_D decreases allowing charge to flow across the depletion region more easily. Thus a current can flow across the pn junction and light will be produced as recombination occurs. The pn junction under forward bias conditions can be seen in Figure 1.8. For light to be emitted by an LED, a forward-bias must be applied.

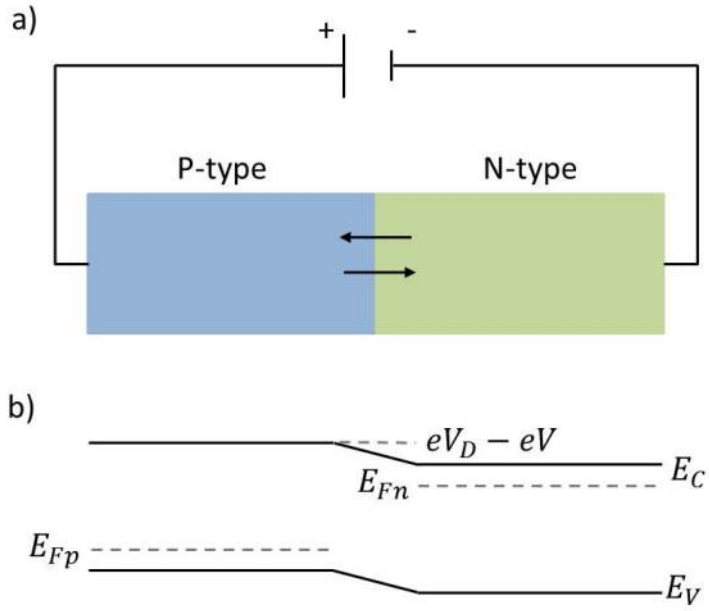

Figure 1.8: a) a simplified pn junction under forward bias, b) the band diagram under forward-bias, where the horizontal axis represents distance perpendicular the plane of the junction.

Figure 1.9 shows the ideal, and non-ideal, current-voltage (IV) characteristics of an LED. The deviation from the ideal IV characteristic can be attributed to series and parallel resistances in the diode:

$$I = I_{\mathrm{s}} e^{\mathrm{eV}/(\mathrm{n_{ideal}kT})} \tag{1.9}$$

$$I - \frac{(V - IR_{\mathrm{s}})}{R_{\mathrm{p}}} = I_{\mathrm{s}} e^{\mathrm{e(V\ -\ IR_s)}/(\mathrm{n_{ideal}kT})} \tag{1.10}$$

In these equations, R_s and R_p are the parasitic series and parallel resistance, respectively, and $\mathrm{I_s}$ is the current drawn by the device before light emission (also known as leakage current). The n_{ideal} term is an ideality factor, which is a number between 1 and 2 and increases with increasing current [31]. For the ideal diode $n_{ideal} = 1$, although with GaN-based LEDs an ideality factor of much greater than 2 (sometimes even greater than 5) has been reported [32, 33] and is thought to be a result of carrier leakage through non-ohmic contacts or trap assisted tunnelling in the active region. A high ideality factor limits the power efficiency of an LED, and so various techniques are employed at growth level to reduce the occurrences of tunnelling within the LED [34–36] and therefore reduce n_{ideal}.

In an LED, the forward-bias is increased and once a certain bias, $\mathrm{V_d}$ is reached, a current flows across the depletion region, electron-hole recombination occurs and light is emitted. This bias, $\mathrm{V_d}$, is known as the turn-on voltage i.e the voltage at which the LED "turns on" and emits light. In a good device eV_d is approximately the bandgap of the active material of the LED, this is illustrated in Figure 1.10b).

1.5 Charge confinement in LEDs

While a basic pn junction in a direct gap semiconductor functions as an LED, with the radiative recombination of electrons and holes across the aforementioned depletion region emitting light, one disadvantage is that the carriers diffuse over a relatively large volume. This results in a low concentration of minority carriers. The radiative recombination rate is given by the bimolecular recombination equation [31]:

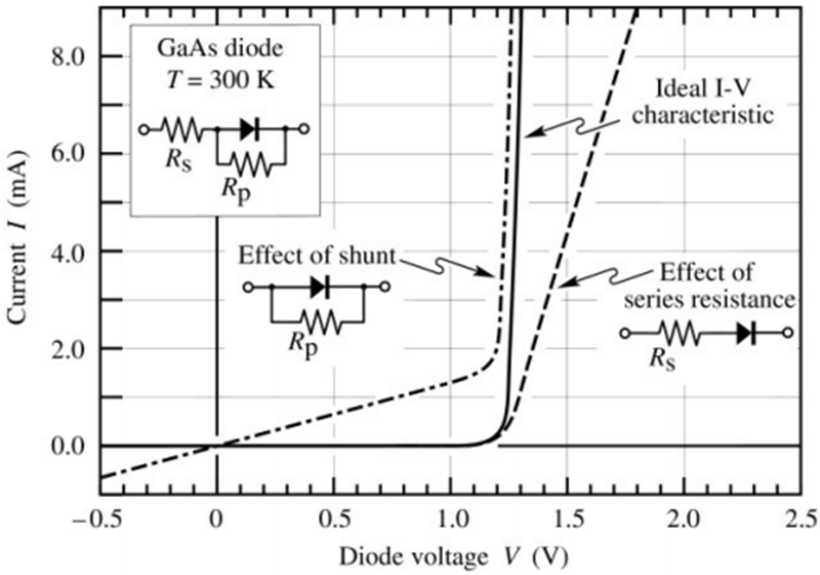

Figure 1.9: Current-voltage characteristic for a GaAs LED at room temperature. The ideal current-voltage characteristic shown in the solid curve. The effect of series resistance and parallel resistance (shunt) on the current-voltage characteristic are shown in the dashed curves. Image from [31].

$$R = Bnp \tag{1.11}$$

Here B is the bimolecular recombination coefficient, and n and p are the electron and hole concentrations respectively. This equation tells us that with low carrier concentration the rate of radiative recombination is low, and hence the efficiency of the LED is low. Most high efficiency LEDs are therefore based on a p-i-n junction. Here i indicates an intrinsic semiconductor. A p-i-n junction is therefore one where an undoped layer of relatively low bandgap is sandwiched between two larger bandgap materials heavily doped with p- and n-type impurities. This is known as a double heterostructure and can be seen schematically in Figure 1.11.

In a double heterostructure carriers become confined in the narrow intrinsic region, increasing the chance of radiative recombination occurring. If this intrinsic active region is made thin enough, it will become comparable to the de Broglie wavelength for the confined charge carriers and quantum size effects become apparent. The de Broglie

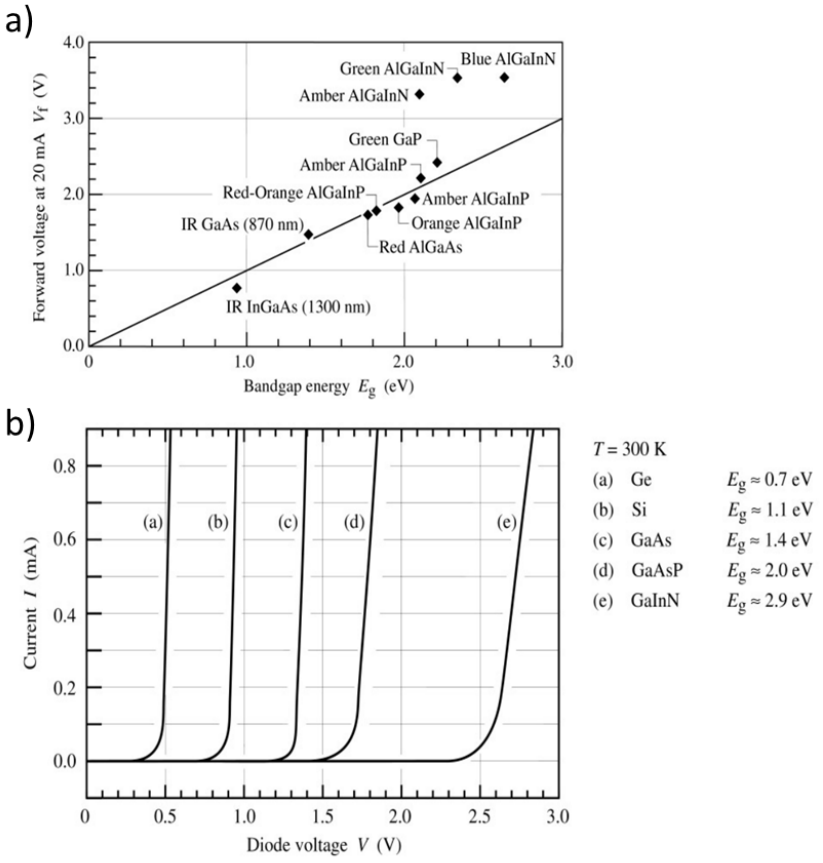

Figure 1.10: Room temperature forward voltage and current-voltage characteristics of LEDs fabricated from different materials. Images from [31].

wavelength is given by:

$$\lambda = \frac{h}{p} = \frac{h}{\sqrt{2m^* kT}} \tag{1.12}$$

where m^* is the effective carrier mass and p is the carrier momentum. For electrons at room temperature in GaN the de Broglie wavelength $\lambda \approx 10$ nm and so when a GaN intrinsic layer is ≈ 10 nm quantum size effects will occur. In this case, the active region is referred to as a quantum well.

In a quantum well the charge carriers in the low bandgap material have insufficient

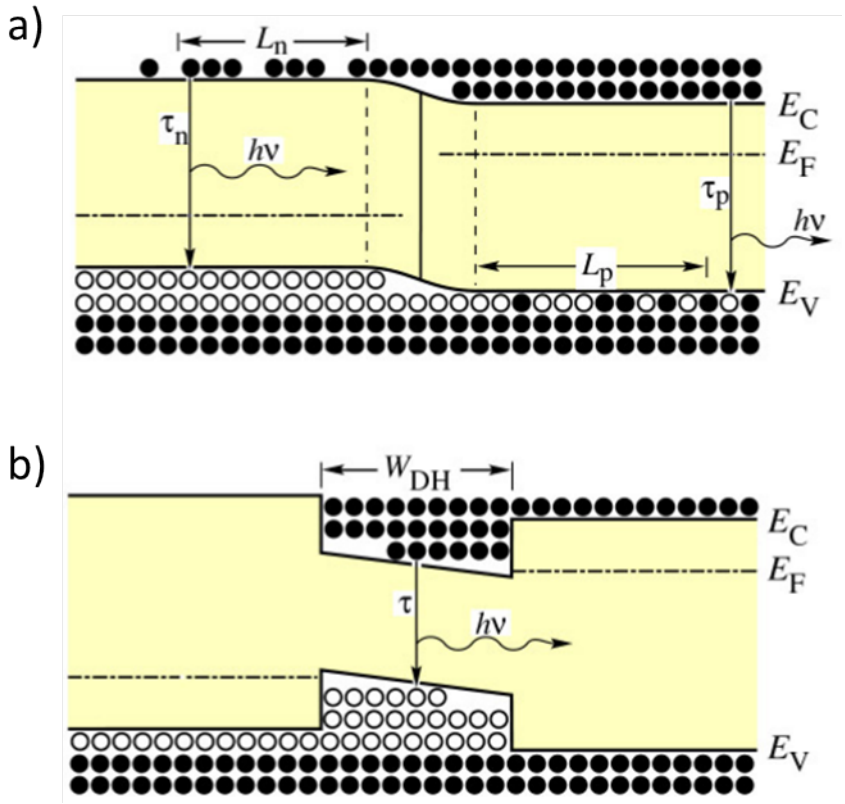

Figure 1.11: The charge distribution and energy levels in a) a pn junction and b) a double heterostructure. Here the vertical axis is energy and the horizontal axis is distance perpendicular to the junction. Electrons are shown in black, holes are shown in white. Image from [31].

energy to escape and so are confined within the quantum well. This can be explained by considering the active region as a "potential well", a schematic of which can be seen in Figure 1.12. This shows the first and second confined energy states, E_1 and E_2, within the conduction band and the equivalent first and second confined energy states within the valence band, E_1^* and E_2^*. These states are shown in red and blue respectively. Above these are shown the probability distribution functions for electrons and holes for each respective energy. E_W and E_b are the energy gaps in the well and barrier materials, respectively.

The frequency of light emitted when an electron in a quantum well transitions from the first state in the conduction band to the first state in the valence band is governed

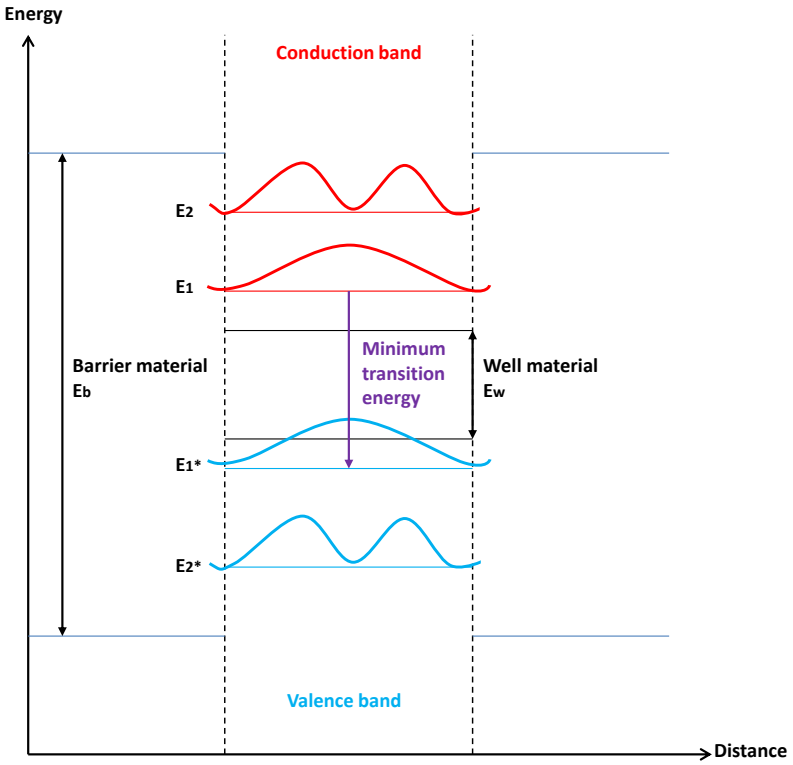

Figure 1.12: Schematic showing the first and second confined states within a potential well.

by:

$$h\nu = E_{\mathrm{W}} + E_1 + {E_1}^* \tag{1.13}$$

Because the energy states in a quantum well are quantised, the quantum well will emit light at discrete wavelengths only. The allowed energy levels within a quantum well with infinite potential barriers are given by:

$$E_{\mathrm{n}} = \frac{n^2 h^2}{8mL^2} \tag{1.14}$$

where L is the width of the potential well i.e. the thickness of the well material in a quantum well structure. As the well gets thinner, the energy levels become more

Quantity	Symbol	AlN	GaN	InN	(unit)
Lattice constant	a_0	3.112	3.191	3.545	Å
Bandgap	E_g	6.28	3.425	0.77	eV
Refractive index near E_g	n	2.15	2.5	2.9	-
Electron mobility	μ_n	300	1500	3200	cm^2/Vs
Hole mobility	μ_p	14	3	-	cm^2/Vs

Table 1.1: Properties of nitride binary alloys.

separated and occur at higher energies which, of course, affects the light emission. Therefore, altering the width of a quantum well in a p-i-n junction allows for control over the wavelength of light emitted by the LED.

Most LEDs utilise active regions with several closely spaced quantum wells, which are referred to as multi-quantum wells (MQWs). This increases the likelihood of charge carriers being confined within a potential well, and light being emitted.

1.6 AlInGaN LEDs

The LEDs used throughout the work presented in this thesis are based on the AlInGaN materials system, the lattice constant and bandgap of which are illustrated in Figure 1.5. The AlInGaN system is one encompassing three binary alloys: aluminium nitride (AlN), gallium nitride (GaN) and indium nitride (InN), and their ternary and quaternary alloys. As seen in Figure 1.5 and discussed briefly in Section 1.3, the bandgap range in the AlInGaN sytstem leads to the potential of producing LEDs emitting from the deep UV (AlN) to the IR (InN) by altering the relative mole fractions in the ternary or quaternary alloys. AlN LEDs with emission down to 210nm have been produced [37]. Some important characteristics of the AlInGaN binary alloys are given in Table 1.1.

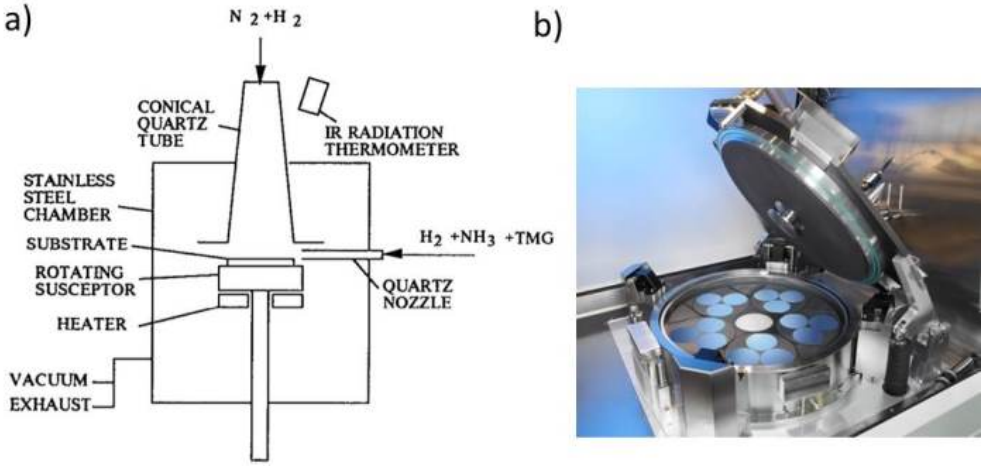

Figure 1.13: a) a schematic (image from [38]) and b) a photograph (image from [39]) of MOCVD reactors.

1.6.1 Epitaxial growth of AlInGaN LED materials

The AlInGaN LED material used in the work presented in this thesis is grown by metal organic chemical vapour deposition (MOCVD). This involves the epitaxial growth of thin films of a material on a substrate by a process involving chemical reactions using gas and/or vapour sources. The MOCVD process involves complex metal organics as precursor materials which usually have the appropriate reactivity under heating i.e. bonds between the central metal atom and organic ligands are often weak. This means these metal organics can act as metal sources for many III-V compound semiconductors - including those derived from the AlInGaN material system. The typical chemistry for compound semiconductor deposition via MOCVD is :

$$\text{Metal alkyl} + \text{Non-metal hydride} \rightarrow \text{Compound} + \text{Hydrocarbon} \tag{1.15}$$

To grow III-nitrides, vapours containing gallium, aluminium and indium are created by introducing trimethylgallium ($Ga(CH_3)_3$, TMG), trimethylaluminium ($Al(CH_3)_3$, TMA) , or trimethylindium ($In(CH_3)_3$, TMI) into the reaction chamber. These metal organic molecules are flowed over the growth substrate which has been heated to

>1000°C, where they react with ammonia gas (NH_3) which provides the nitrogen source. The precursor molecules fragment on approaching the hot substrate, and an ordered array of the desired III-nitride is deposited on the substrate surface. Hydrogen is used as a carrier gas for the metal organic sources, with the ammonia normally in large excess.

By varying the composition of the precursor molecules in the reaction chamber, the properties of the growth material can be controlled. The desired material then builds up in layers on the growth substrate.

The reaction takes place inside a stainless steel chamber, as in Figure 1.13 a) for the case of GaN growth, designed to withstand the high growth temperatures and to be un-reactive with either the precursor molecules or reaction by-products.

1.6.2 Suitable substrates for AlInGaN growth

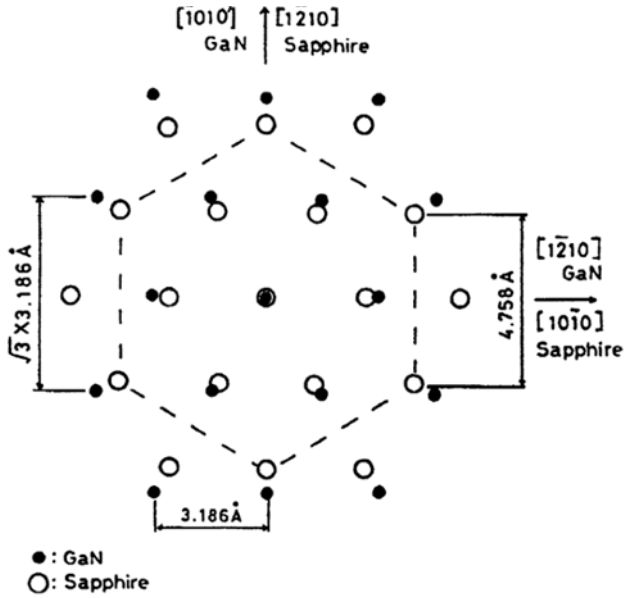

Figure 1.14: The crystal structure of GaN, in this case grown on sapphire (001). Image from [40].

The GaN used in the LEDs throughout this work has a wurtzite crystal structure, as

illustrated in Figure 1.14. When growing semiconductor materials it is vitally important to choose a substrate with as little lattice mismatch to the semiconductor material as possible. This concept of lattice mismatch was briefly touched upon in Section 1.3 in relation to introducing appropriate dopant atoms into a host semiconductor lattice. In an ideal case, when growing blue-emitting InGaN-based LED epilayers, a single crystal GaN substrate would be used and there would be no lattice mismatch between substrate and growth material. However, bulk GaN is difficult and expensive to make and so c-plane sapphire (16% lattice mismatch for blue-emission) is conventionally used as a growth substrate [41]. While this lattice mismatch introduces a relatively high concentration of 10^8 cm^{-2} - 10^9 cm^{-2} threading dislocations in the GaN film, in contrast to most other semiconductors the presence of so many defects does not rapidly degrade the electrical or optical properties of GaN LEDs [42, 43].

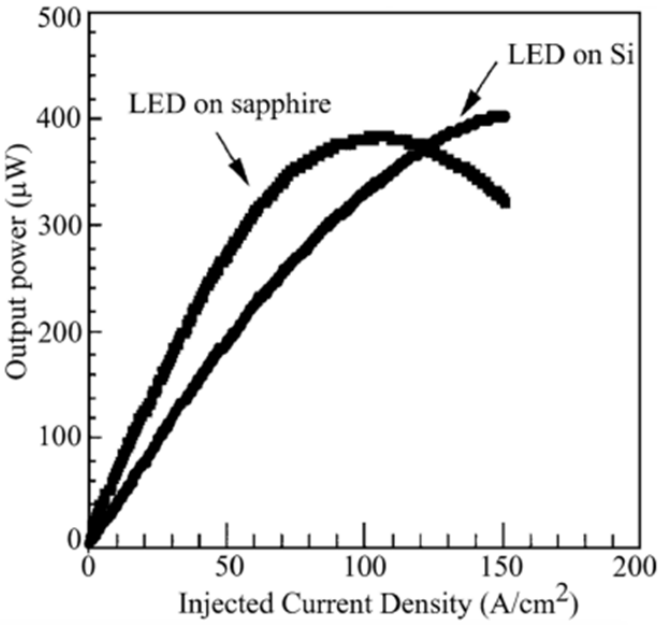

Figure 1.15: The power vs. current characteristics of a GaN-on-sapphire LED and a GaN-on-Si LED, adapted from [44]

.

The blue-emitting InGaN-based LED material used in this work is not grown on a sapphire substrate but rather on a (111) orientation silicon (Si) substrate. A schematic

of the LED wafer can be seen in Figure 2.9 in Chapter 2. Silicon substrates are much cheaper than sapphire ones as well as having the potential for large scale GaN-on-Si production on large wafers and for integration of Si electronics on the same chip. GaN-on-Si wafers are therefore of great interest to the semiconductor industry. Another advantage for LED fabrication from GaN-on-Si is that, because Si has a higher thermal conductivity than sapphire (1.5 $Wcm^{-1}K^{-1}$ and 0.35 $Wcm^{-1}K^{-1}$, respectively), LEDs grown on Si can be driven to higher current densities than those grown on sapphire but otherwise fabricated identically, as seen in Figure 1.15. This has been reported in literature by *Egawa et.al.* [44]. They also report that when the injected current density reaches 120 A/cm^2, the output power is greater in the GaN-on-Si LED than in a comparable GaN-on-sapphire device. The slower rise in optical power in the GaN-on-Si device, as in Figure 1.15 can be attributed to the absorption of the emission by the Si substrate.

A few major drawbacks, however, exist when growing GaN-on-Si. Si forms a highly stable native-oxide when exposed to an oxygen environment. This must be removed before MOCVD growth of GaN, and due to its amorphous nature the Si oxide can leave the Si surface rough causing problems with growing high-quality GaN on the Si surface. During the MOCVD growth of GaN, Ga also tends to react with Si to create a Ga-Si alloy which melts into the Si roughening both the substrate and the newly-grown film. This is known as a *"melt-back"* etching process, and can degrade the GaN-on-Si as in Figure 1.16 a). High growth temperatures ($\approx 1100\ ^\circ C$) alleviate this "melt-back" issue, because high temperatures favour "layer-by-layer" growth of GaN rather than a more 3D-type growth [45]. Due to the highly reactive chemical nature of the precursors, Ga can end up etching the Si forming *"pits"* on the silicon surface, which lead to dislocations in the growth film.

Another drawback is the large lattice mismatch between GaN and Si (17%) and a large difference in thermal expansion coefficients (33%) which leads to substantial defects propagating through the GaN film, as can be seen in Figure 1.16 b). The large difference in thermal expansion coefficients means that cracks often propagate in the

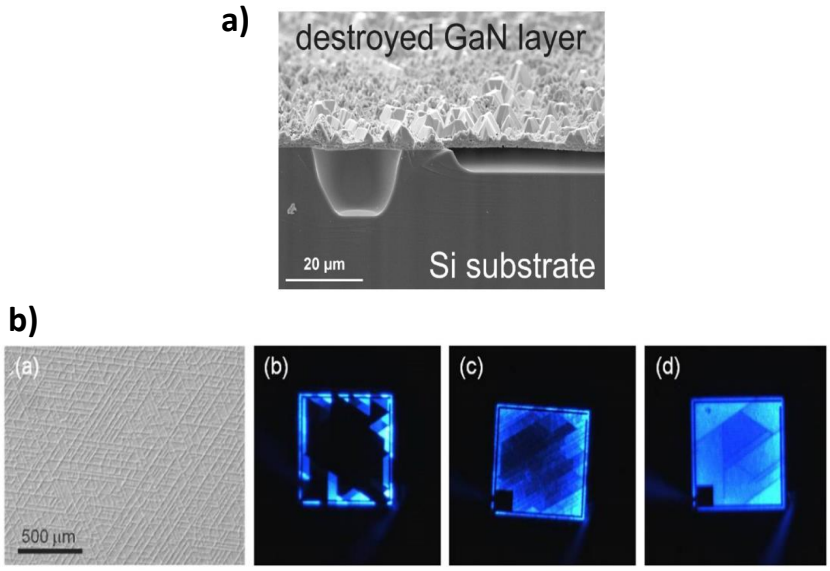

Figure 1.16: A few examples of defects occurring when GaN is grown on Si. a) "Melt-back etching" destroys GaN grown on a roughened Si substrate [26], and b) the issue of cracking due to differences in thermal expansion coefficients and their effects on LED performance [46].

grown material, because the wafer is put under tensile stress during cool-down to room temperature from the high growth temperature, see Figure 1.16 c). Wafer bowing can also be induced because of strain from this mismatch in thermal expansion coefficients. To counteract the issues caused by the lattice mismatch and the difference in thermal expansion coefficients, several methods can be deployed during growth to yield high-quality GaN grown on Si [41]. For example, growing a few monolayers of AlN and then a thicker AlGaN buffer layer before the GaN growth [45, 47, 48]. A SiN_x interlayer can also be used to decrease threading dislocations propagating through the GaN layers. These interlayers compensate for the strain effects and dislocations and bowing induced because of the difference in lattice size in GaN and Si. It is these techniques that are employed by Plessey engineers during the growth of the GaN-on-Si LED wafers used throughout this PhD. Figure 1.17 shows the emission spectrum from a 300 $\times$ 300 μm^2 LED. This was fabricated from the GaN-on-Si wafer used in this work, and we see a single peak at 450 nm.

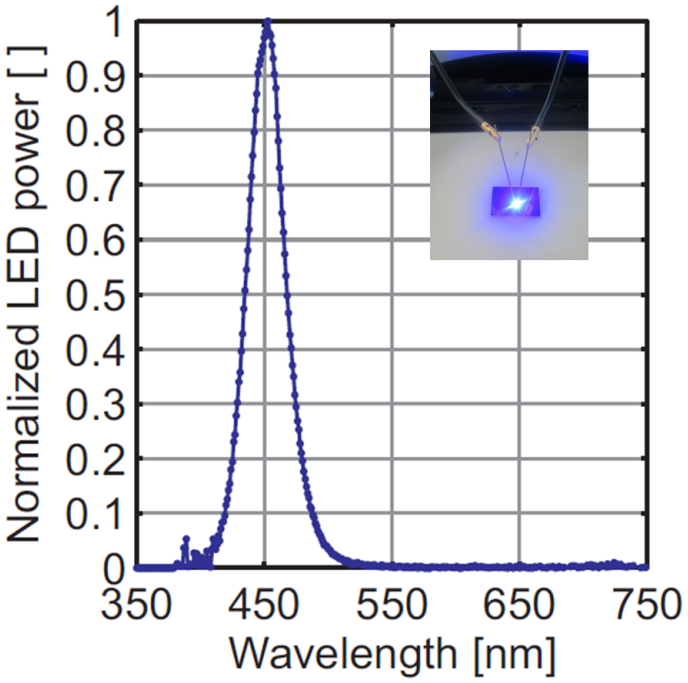

Figure 1.17: Emission spectrum from a 25 μm diameter μLED fabricated from a GaN-on-Si wafer. The inset shows a broad-area 300 $\times$ 300 μm^2 LED fabricated from a similar GaN-on-silicon wafer being probed and lighting up.

1.7 LED design, structure and fabrication

As discussed above, most high-power blue emitting LEDs are fabricated from the AlInGaN materials system, with InGaN/GaN MQWs grown on a sapphire substrate. The devices are fabricated in cleanrooms from GaN-on-sapphire LED wafers, typically containing MQWs around 3 nm-thick with an In molar fraction of 0.1-0.2 or 0.45 for blue and green emitting LEDs, respectively [43]. First the large wafer is diced into small chips, with a chip then used to produce several broad-area LEDs, usually with an emitting area of several hundred square microns. The chip is then surface treated with HCl (to remove any surface oxide) before the deposition of a thick metal current spreading layer on the top of the p-GaN side of the wafer, which acts both to inject current effectively and also as a mirror to reflect light down in so-called "flip-chip" LEDs to increase the light-extraction efficiency. The addition of this metal layer means the majority of light emitted from the LED will now be through the sapphire substrate, as seen in Figure 1.18. It is useful to note here that light is emitted from the active region in an LED in all directions, and the addition of a thinner, transparent current spreading layer will yield a top-emitting LED with light emitted up, through the p-GaN side of the LED. However, with light also emitted downwards, top-emitting LEDs have lower power than flip-chip devices. Therefore, most conventional high-power LEDs are likely to be in this flip-chip geometry.

Once coated with metal, photolithographic patterning and a series of (inductively coupled) plasma etches are used to etch down through the epistructure to access the n-type GaN - etching an n-mesa. This is required in order to be able to inject current into the pn junction.

Once this n-mesa is etched, the pn junction can be electrically accessed and the LED will emit light under an appropriate bias. Thick metal bond pads are deposited on to form the p- and n-contacts, and then thermally annealed, to allow the LED to be driven electrically via bonded wires or direct probing.

A cross-sectional schematic of an LED fabricated in this manner is seen in Figure 1.18a). Figure 1.18b) shows a section of an array of LEDs fabricated in this manner, with the p- and n-bonding pads seen in yellow/gold.

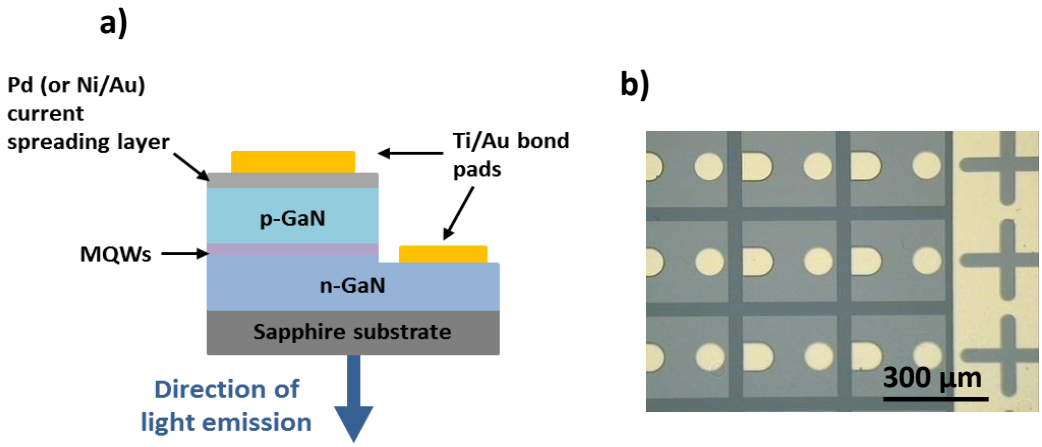

Figure 1.18: a)A cross-sectional schematic of a typical GaN-based LED on a sapphire substrate, and b) a plan view microscope image of a section of an LED array fabricated on GaN-on-sapphire. Nine LED pixels, with Pd current spreading layers, and Ti/Au p- and n-bonding pads are shown.

1.8 Micro-LEDs

LEDs patterned via photolithography such that they form an array of separate small-size LEDs each with dimensions of under 100 μm are known as micro-LEDs (μLEDs). This contrasts with the typically larger high power, broad-area LEDs which have a single emission area ranging from 300 x 300 μm^2 to 1 mm^2 used for conventional LED applications (such as solid state lighting). For the same area as a single broad-area device, there can therefore be an array of hundreds or even thousands of μLEDs. Figure 1.19 a) shows a plan view microscope image of an area of a blue-emitting μLED array with pixels of 84 μm diameter.

The first electrically-injected AlInGaN μLED array was demonstrated in 2000 by Jin et

al. [49]. These were 12 μm diameter disc-shaped μLEDs fabricated from InGaN/GaN LED wafer as in Figure 1.20 a). Since then, the development of wafer growth techniques as well as advances in the fabrication and bonding of such devices has lead to large arrays of μLEDs now being fabricated and several review papers on μLEDs being published [50–52].

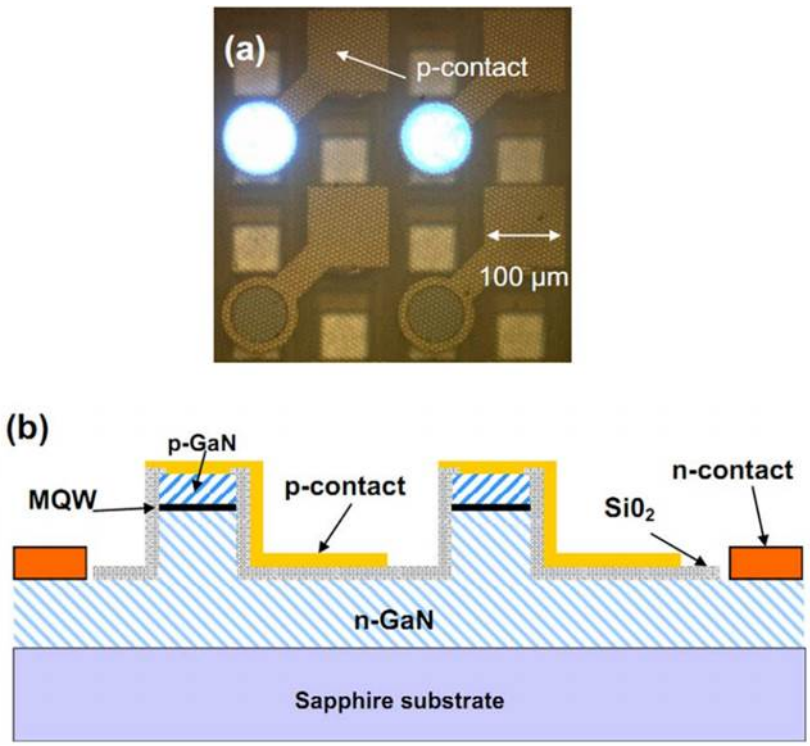

Figure 1.19: a) A plan view microscope image of a section of an 8 x 8 array of μLEDs emitting at 450 nm, each 84 μm in diameter with two pixels illuminated and b) a corresponding cross-sectional schematic of the μLED pixels at wafer level, fabricated by *McKendry et al.* [28].

First, the surface of the wafer is treated with HCl before being coated in a thick Pd current spreading metal layer on top of the p-type GaN to act as a contact/mirror. The individual pixels are then defined with photolithography and plasma etching (the details of which will be discussed in detail in Chapter 2) before the array is electrically insulated with SiO_2 to electrically isolate each pixel. Finally thick Ti/Au metal bonding pads are deposited onto the p- and n-contact of each pixel to allow the μLEDs to be electrically driven. Much of the μLED work at the Institute of Photonics has also

used InGaN/GaN MQW wafers on sapphire substrates. The fabrication is outlined in [28, 53]. A simple cross-sectional schematic of two μLED pixels fabricated from this array can be seen in Figure 1.19 b). These μLED arrays can be designed to be bonded onto printed circuit boards (PCBs) or onto complimentary metal oxide semiconductor (CMOS) boards to be electrically addressed.

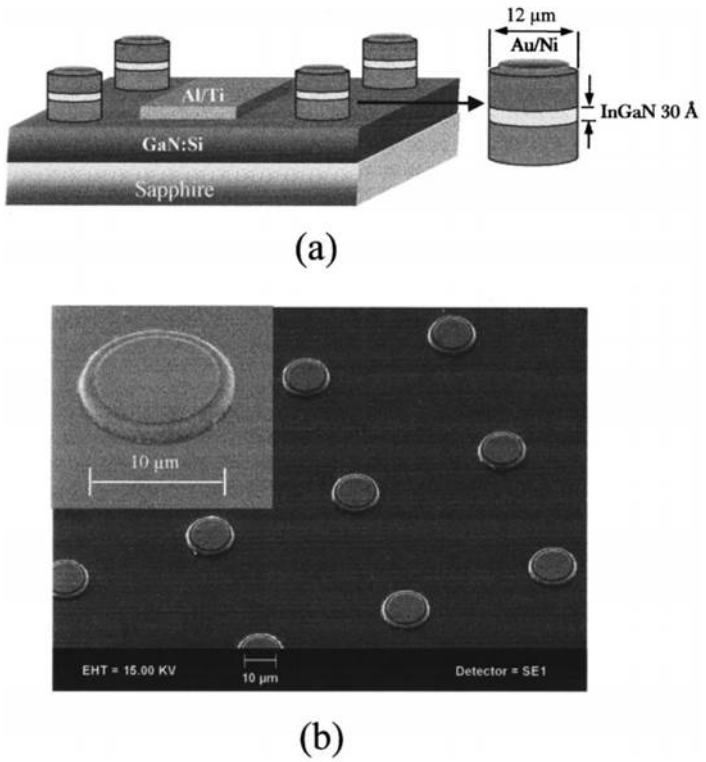

Figure 1.20: a) A cross-section schematic and b) an SEM image of the first demonstration of an electrically-injected AlInGaN μLED, from [49].

1.8.1 Characteristics and advantages of μLEDs

Small μLEDs offer several advantages over conventional broad-area LEDs. The optical power density of a μLED will be higher than that of a broad-area LED with an identical epitaxial structure. This means that an array of interconnected μLEDs can be more efficient than a comparable broad-area LED with the same effective active area [54]. The smaller devices have also been demonstrated as having much shorter

optical turn-on times than comparable broad-area devices [55]. This makes them useful for applications requiring short optical pulses or high modulation bandwidths. Because of their size, μLEDs (and arrays of μLEDs) act almost as collimated light sources across short distances (comapared to larger broad-area LEDs) and can be easily coupled into fibres for communications applications [56]. They can also be operated in arrays and as micro-displays [50, 57].

Compared to larger broad-area LEDs, μLEDs have low junction temperatures. A typical 1 mm^2 GaN-based LED can have a junction temperature of $>$ 100 °C [58], while a 20 μm diameter μLED has a junction temperature just 5 °C above room temperature [59]. Many degredation processes in LEDs are temperature activated; such as increases in the p-contact resistance over long-term operation, and a decrease in hole concentration in p-GaN as Mg-H complexes are generated (removing the Mg dopant atoms). These μLEDs can also be driven to very high current densities, often $>$ 10 kAcm^{-2} compared to 100 Acm^{-2} for broad-area devices. This allows them to be driven such that they achieve high optical power and have high modulation bandwidths. Gallium nitride μLEDs are now routinely fabricated at the Institute of Photonics with modulation bandwidths of $>$ 100 MHz and optical powers of $>$ 1 mW [60]. The high modulation bandwidths of μLEDs is vital to this work and will be discussed further in Section 1.9.2.

1.9 Visible light communications

It is widely accepted that visible light communications (VLC) is an important emerging technology. With an ever increasing demand for wireless data communication, current radio frequency (RF) networks are rapidly becoming insufficient [61]. One alternative range of communication frequencies is those within the visible spectrum. If we imagine sending a Morse code signal by flashing a light on and off, we can clearly see that this is a viable way of sending information. However, to use this light as a sensible illumination source would be difficult due to it flashing on and off. VLC uses this

same concept, but the intensity of the light is modulated much faster than can be picked up by the human eye. This allows room lighting sources to be used with a dual purpose - illumination and data transmission. The intensity of a visible light source can be modulated as fast as, if not faster than, current wireless communication speeds and can therefore be used to send information and meet demands for more wireless communication bandwidth [52, 62].

Due to their cheapness, high efficiency and high power, LEDs are attractive candidates for VLC applications. The first reported use of LEDs for VLC was in 1999, when Pang et al. used modulated traffic lights to transmit information [63]. Using small μLEDs, as will be discussed further in Section 1.9.2, is of interest for VLC as they benefit from high modulation bandwidths (typically 100s of MHz, which is an order of magnitude higher than acheived by broad area LEDs) which means they can be modulated fast enough to be used for high speed data transmission, with speeds over 10 Gb/s from μLED sources being reported [64]. To achieve the high optical power required for room lighting, these μLEDs can be used in arrays (which are compatible with CMOS driver boards) or in conjunction with broad-area white light sources. The data transmission rates can be further increased by using multi-μLED systems, such as wavelength division multiplexing (WDM) [65,66] where multiple discrete wavelengths of light are used to transmit multiple data streams simultaneously (this will be discussed at length in Chapter 3). Spatial multiplexing can also be used to increase the data rate from μLED sources. This relies on the spatial separation of several transmitters and receivers to send multiple streams of data simultaneously [67], with data rates of 7 Mbps achieved using this technique with a specially designed array of μLEDs [68]. In the remainder of this chapter, the basis of VLC with a focus on the aspects pertaining to the work presented here will be discussed.

1.9.1 Modulation bandwidth

When deciding the viability of an LED device for VLC applications, one of the first things we look into is the modulation bandwidth. This tells us how quickly the light intensity can be modulated without distorting the signal. When measuring the modulation bandwidth of an LED in this work, the setup in Figure 1.21 is used to test the frequency response of the LED.

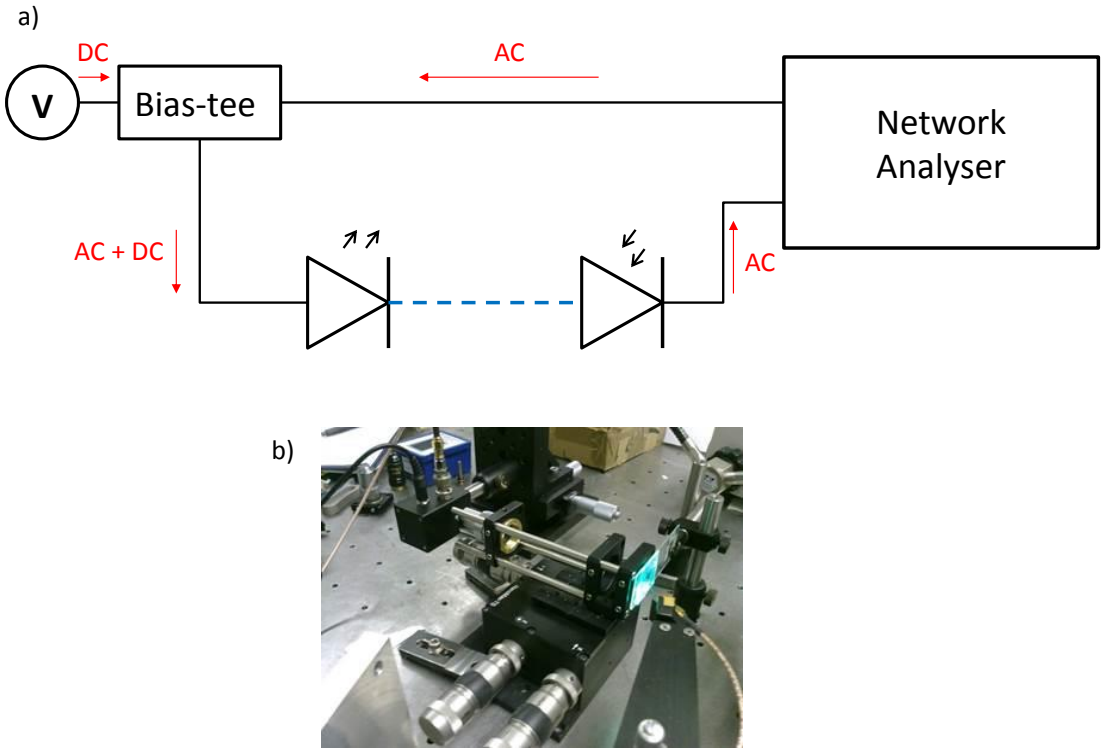

Figure 1.21: a) A schematic of the setup for measuring modulation bandwidth. The LED is shown to the left and the photodiode to the right. A photograph b) showing the LED being modulated and directed at an APD is also shown.

The LED is sent two electrical signals simultaneously: a DC signal and an AC signal. The DC signal comes from a DC power supply, while the AC component is a modulated signal sent from a network analyser (Agilent Technologies 8753ES Option 011). The DC and AC components are both voltage driven, with a modultion about a fixed current

generating the AC signal. This modulated signal is a sine wave of fixed amplitude and is combined with the DC signal using a three-terminal bias-tee and sent to the LED. A three-pin ground signal probe (Cascade Microtech, ACP40-A-GSG-125) is used to directly probe and drive the LEDs. This probe has a bandwidth of 40 GHz, with the signal pin placed on the p-pad and the two ground pins on the n-pad to drive the LED. This setup allows the LED to be driven and modulated, emitting light with modulated intensity.

The emitted light from the LED is then imaged onto a photodetector and the AC part of the signal recieved at this photodetector is fed back into the input port of the network analyser. This signal is then compared to the original AC signal that was sent to the LED, and a frequency response graph is generated. A typical example of the frequency response of the μLEDs used in this thesis is shown in Figure 1.22.

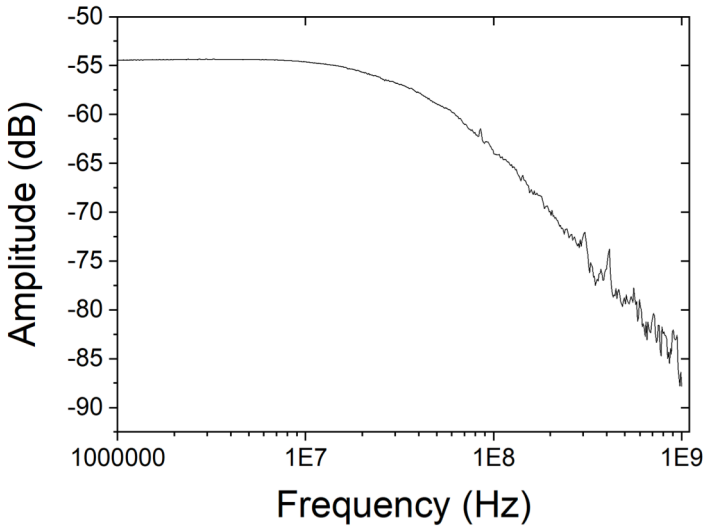

Figure 1.22: A typical frequency response of the blue-emitting μLEDs used throughout this work, as measured with the setup in Figure 1.21. The μLEDs used here are blue-emitting InGaN-based 100 $\times$ 100 μm^2 pixels (fabricated as in Section 2.6) transfer printed on a glass substrate, driven at 6 mA.

It is important to note that all the modulation bandwidths quoted in this thesis are electrical-to-optical (-3 dB) bandwidths. The electrical-to-electrical bandwidth (-3 dB) is defined as the frequency at which the electrical power has dropped by half at DC. The ratio of electrical output power to the electrical input power (in dB) is given by:

$$R_E = 10\log_{10}\frac{P_{out}}{P_{in}} = 10\log_{10}\frac{(I_{out})^2/R_{out}}{(I_{out})^2/R_{in}} \tag{1.16}$$

$$R_E \propto 10\log_{10}\left[\frac{I_{out}}{I_{in}}\right]^2 \tag{1.17}$$

At the electrical-to-electrical 3 dB point, the ratio of powers is equal to $\frac{1}{2}$:

$$\left[\frac{I_{out}}{I_{in}}\right]^2 = \frac{1}{2} \tag{1.18}$$

or

$$\frac{I_{out}}{I_{in}} = \frac{1}{\sqrt{2}} \tag{1.19}$$

Thus the electrical-to-electrical bandwidth can be defined as the frequency where the output current is $\frac{1}{\sqrt{2}}$ of the input current. Due to the linear light output/ current relationships of the LED and detector, the electical-to-optical bandwidth is given by:

$$R_O = 10\log_{10}\frac{P_{out}}{P_{in}} \tag{1.20}$$

$$R_O \propto 10\log_{10}\frac{I_{out}}{I_{in}} \tag{1.21}$$

Hence the (-3 dB) electrical-to-optical bandwidth (the point at which the ratio of output to input power has reduced by half) is given by:

$$\frac{I_{out}}{I_{in}} = \frac{1}{2} \tag{1.22}$$

Therefore, the electrical-optical bandwidth is defined as the point at which the output current has dropped by $\frac{1}{2}$. It follows that the electrical-to-optical bandwidth corresponds to a -6 dB electrical-to-electrical bandwidth [69].

The amplitude of the output power of an AC modulated LED is a function of the frequency of the AC signal, and defines the frequency response (which is shown in Figure 1.22). As defined above, the electrical-to-optical bandwidth is taken to be the frequency at which the response (optical power) has dropped by 50% (-3 dB) of its initial frequency value. In the frequency response shown in Figure 1.22, the -3 dB point corresponds to 146 MHz. The frequency response, P(ω), and the -3 dB modulation bandwidth, $f_{\text{-3dB}}$, are given by:

$$P(\omega) = \frac{1}{\sqrt{1 + (\omega\tau)^2}} \tag{1.23}$$

and

$$f_{\text{-3dB}} = \frac{\sqrt{3}}{2\pi\tau} \tag{1.24}$$

where ω is the frequency and τ is the average carrier lifetime.

1.9.2 Modulation bandwidth of micro-LEDs

Small μLEDs have been shown to withstand very high current densities up to $>$ 10 kAcm^{-2} DC. As μLEDs are driven to higher current density, the modulation bandwidth increases, as is demonstrated in Figure 1.23 with smaller devices being able to be driven harder. This has been explained as being due to a current density dependant reduction in the differential carrier lifetime τ, which is given by:

$$\tau = \frac{1}{A + 2Bn + 3Cn^2} \tag{1.25}$$

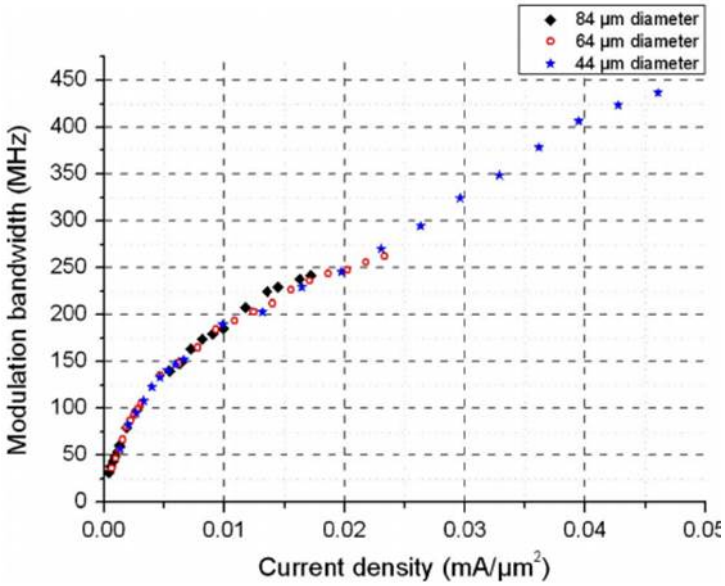

Figure 1.23: Bandwidth versus current density for LEDs of varying diameter fabricated on a single 450nm - emitting LED chip. Image from [28]

.

where n is the carrier density, and A, B and C are the coefficients of the rates of SRH recombination, spontaneous recombination, and Auger recombination, respectively [70, 71]. Smaller LEDs can be driven to higher current density, and therefore n increases with decreasing size. This means the differential carrier lifetime can become much shorter in μLEDs than large broad-area LEDs. Therefore, as we decrease the size of a μLED, we can increase the achievable modulation bandwidth [28, 72]. For this reason, μLEDs are of great interest in VLC research as they can be used for very high speed data communications, with modulation bandwidths of ≈ 1 GHz now being reported for a single μLED [73].

1.9.3 Data transmission and encoding schemes

When transmitting data with a light source, for a given signal power, the channel bandwidth limits the maximum data rate. This is shown by the Shannon limit, given in the equation below:

$$Capacity = BW \times \log_2(1 + SNR) \tag{1.26}$$

where BW is the modulation bandwidth of the channel, and SNR the signal-to-noise ratio.

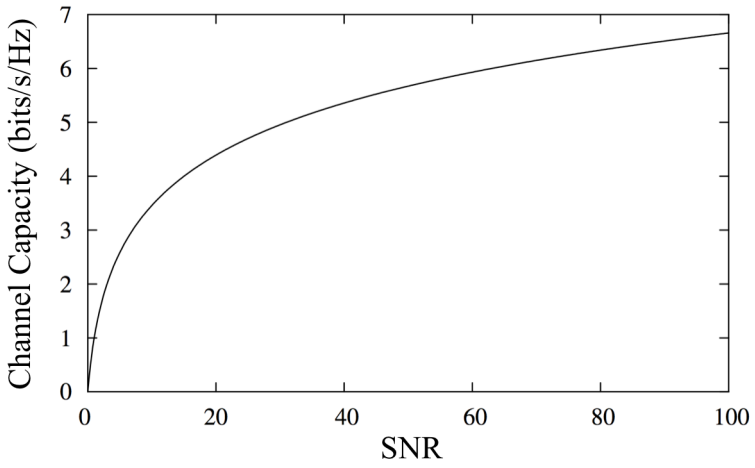

Figure 1.24: Channel capacity as a function of SNR, from [74].

When this function is plotted graphically, as in Figure 1.24, we see that increasing the SNR gives diminishing increases in capacity. At sufficiently low power, as with μLEDs, the SNR is low and the capacity increases linearly (as at the lower end of the curve in Figure 1.24) and the Shannon limit can be approximated as:

$$Capacity \approx BW \times Power \tag{1.27}$$

Therefore there are two ways of increasing the channel capacity i.e. the number of transmitted bits per second. One is to increase the SNR by increasing the power, but this becomes an issue for battery powered or mobile devices. The other alternative is to use more bandwidth. Data encoding schemes can help with this, and multiple levels can be introduced to make the most of available bandwidth. This is what will be discussed in the following.

Amplitude modulation

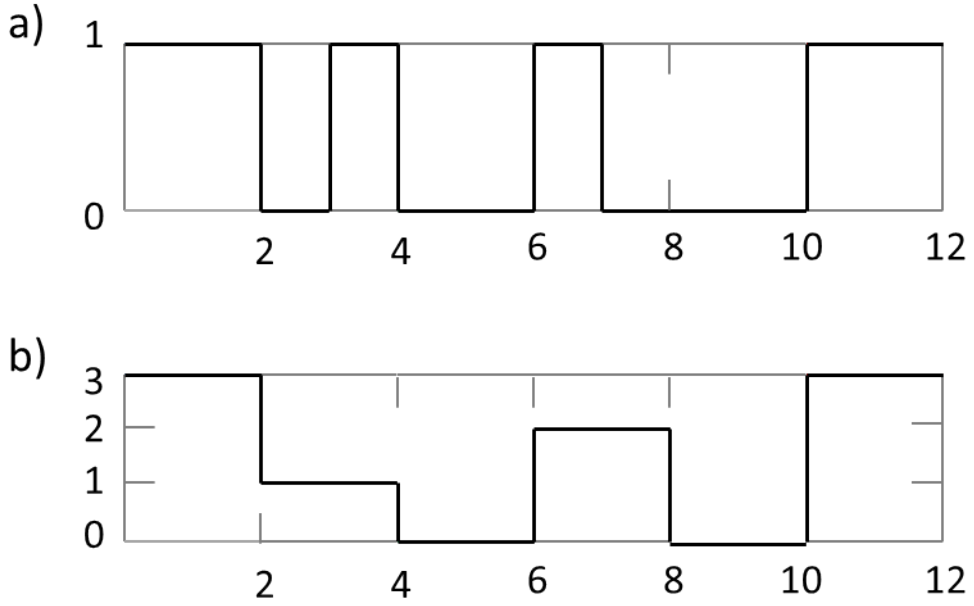

Figure 1.25: The time waveforms of a) OOK and b) 4-PAM for a binary input sequence of 110100100011 for the same data rate.

As discussed at length in the previous few sections, VLC relies on the ability to modulate the intensity of a light source to transmit information. When transmitting data optically, the simplest way of encoding this data is in the amplitude (intensity) domain. Data encoding schemes falling into this category are on-off keying (OOK) and pulsed amplitude modulation (PAM). This sub-section will discuss these amplitude modulation data encoding schemes for VLC.

Figure 1.25 a) shows the basis of OOK as a way of encoding data. A stream of bits is transmitted in a binary form, i.e. to send the bit 1 the optical source is driven at a specific current, and to transmit the bit 0 the optical source is switched off. The modulated signal is generated, in most cases, by the use of an electrical wave signal in the shape of the bit stream to modulate the intensity (amplitude) of the optical emission. This explanation is rather simplified, in many real-life OOK systems, data is sent as a small signal modulation on a DC intensity i.e. not between a specific current

and zero current, but rather between two non-zero intensities.

Because OOK has only two levels with which to send information, the data transmission rates are limited by how quickly the source can be turned on and off. A more complex, but faster, way of transmitting data is to introduce more levels at intermediate stages between on and off. This is known as pulsed amplitude modulation (PAM), and is shown schematically in Figure 1.25 b). PAM makes use of the ability to vary the amplitude of individual pulses in a regularly timed sequence of electromagnetic pulses. This is done by varying the drive voltage or optical power of the light emission. The relationship between the number of bits transmitted and the number of discrete levels is given by:

$$M = 2^{\mathrm{m}} \quad \text{or} \quad m = log_2 M \tag{1.28}$$

where m is the number of bits to be encoded, and M is the number of levels [75]. For example 4-PAM has 4 different levels, while 8-PAM has 8 different levels.

A third modulation scheme, partially based on amplitude modulation is Quadrature Amplitude Modulation (QAM). Here the data is encoded through both the amplitude and phase of the signal, which tends to be sinusoidal. The amplitude of two sinusoidal waves with the same frequency, but 90^0 out-of-phase with each other is modulated. Therefore such phase modulation schemes use the available bandwidth more efficiently than modulating with amplitude only.

Usually QAM is represented by a constellation diagram, with the number of constituent points representing the allowed levels for encoding data. The more points in the constellation, the more bits per symbol it is possible to encode. Figure 1.26 shows a 16-QAM constellation, with the amplitude, phase and data information shown to encode two possible bit streams.

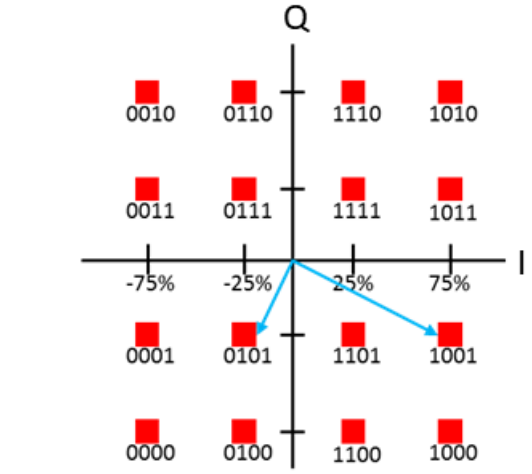

Amplitude	Phase	Data
-25%	225°	0101
75%	337°	1001

Figure 1.26: Schematic of a 16-QAM constellation and a table with two possible combinations of amplitude, phase and data. This QI (where Q is phase, and I is amplitude (or intensity)) diagram shows 4 different amplitude levels, allowing for 16 QAM levels.

Frequency modulation

Another way of transmitting a bit stream, where each bit is represented by a different condition (e.g. different voltage levels) is to modulate data in the frequency domain. This is known as frequency division multiplexing. Orthogonal frequency division multiplexing (OFDM) is a high level data encoding scheme used to increase the data transmission speeds from optical sources compared to those that can be achieved with amplitude modulation schemes like OOK, PAM and QAM. OFDM [76, 77] modulates the data carriers orthogonally, increasing the bit stream transmitted by an optical source.

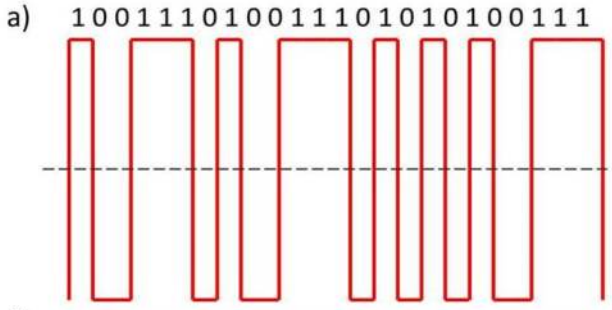

b)

C1	C2	C3	C4
1	0	0	1
1	1	0	1
0	0	1	1
1	0	1	0
1	0	1	0
0	1	1	1

Figure 1.27: a) Representation of a bit stream and b) its division into sub-carriers.

In OFDM, the bit stream is initially split into smaller sub-carriers, and modulated using QAM (or another phase modulation scheme such as phase-shift keying modulation). Figure 1.27 shows a bit stream and its sub division into four sub-carriers, each represented by 6 bits. Once divided into sub-carriers, the bit stream is modulated. This modulation uses mathematical formulae to turn each sub-carrier bit stream into a sinc function, as in Figure 1.28. The sub-carriers are orthogonal and so can be distinguished from one another.

The resulting OFDM signal is made after combining these sub-carrier sinc functions with an inverse fast Fourier transform (IFFT). This converts the signal from the frequency domain (as in Figure 1.28) to the time domain. A digital to analogue conversion is performed on the resulting spikes, from the IFFT, to give the final OFDM signal. A typical OFDM signal, as in [78], is seen in Figure 1.29.

In VLC, the receiver will detect only the modulated intensity of the light emitted from the source. This means that the transmitted signal must be both positive and real. Therefore in the work presented here, OFDM is implemented using intensity

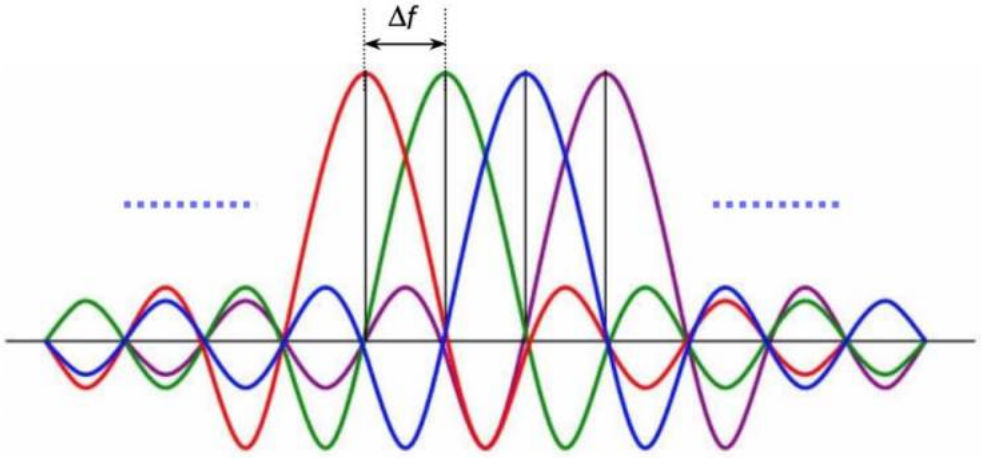

Figure 1.28: Schematic of the subcarrier signals in the frequency domain in an OFDM data encoding scheme. Here the horizontal axis is frequency, and the vertical axis amplitude. Image from [76]

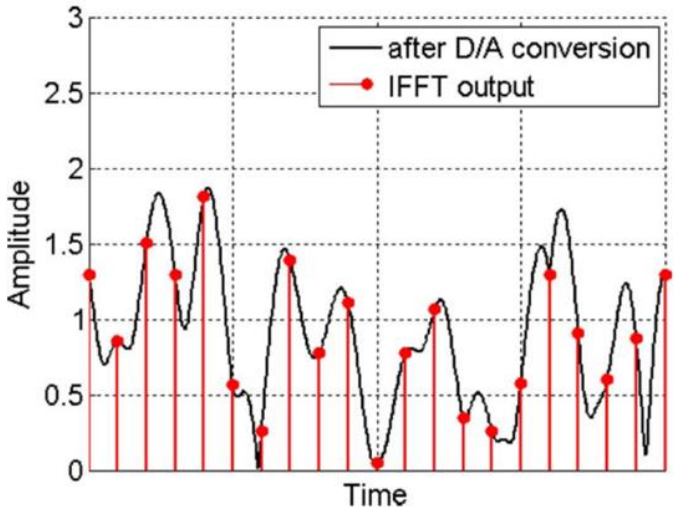

Figure 1.29: Amplitude of the signal at the output of the IFFT and the continuous OFDM signal after digital to analgogue conversion conversion. Image from [78]

modulation/ direct detection (IM/DD) which differs from conventional OFDM (which uses phase and amplitude modulation). In IM/DD, Hermitian symmetry is imposed before the IFFT to generate a real output. A DC-offset addition is used to prevent negative intensity, as outlined in detail in [79]. Figure 1.30 shows the IM/DD OFDM process for VLC in a block diagram. As previously discussed the μLEDs used for

data transmission in this work are powered with both a DC (for illumination) and AC (for communication) signal. This is done in the electrical domain by modulating the voltage sent to the μLED. The Hermitian symmetry and IFFT then are performed on this electrical signal and a real intensity modulated signal is generated. Once at the receiver (APD) this is converted back to an electrical signal.

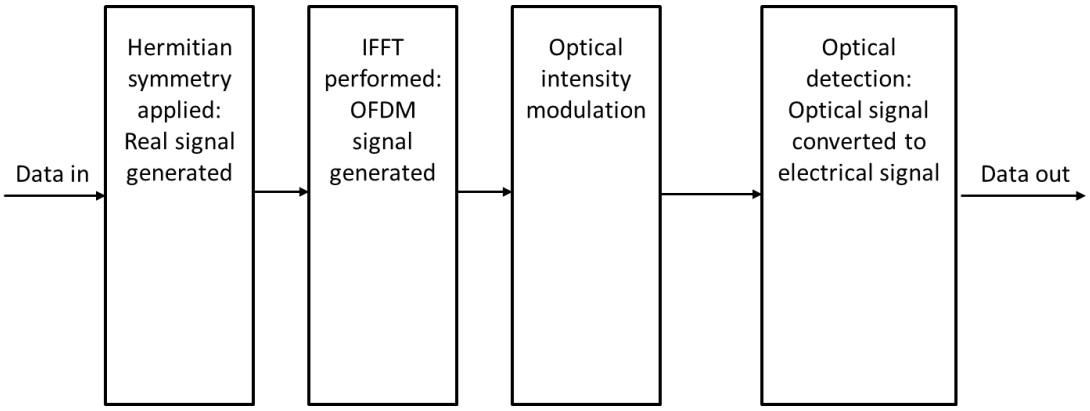

Figure 1.30: Block diagram showing the IM/DD OFDM process.

It is important to note here that the data transmitted can only be useful if it can be separated from any noise or error in the system. Forward error correcting (FEC) is a technique used to control errors in data transmission. This technique sends a redundant stream of bits along with the actual data stream, and the receiver only accepts data arriving that agrees with the redundant stream. When applied to a system, this allows the system to correct for errors up to a certain level and the signal can be transmitted error-free. The FEC level used throughout this work assumes error-free data transmission down to a bit error rate (BER) of 3.8×10^{-3}. BER is the percentage of bits that have errors relative to the total number of bits received in a transmission.

1.9.4 Decoding data from modulated light

OFDM is used to encode the data transmitted by different light-emitting devices fabricated with μLEDs in all of the data transmission experiments presented throughout this thesis. The setup for measuring the data transmission characteristics is seen in

Figure 1.31.

A modulated signal is sent to a μLED by using a bias-tee to combine a modulated AC OFDM signal from a signal generator and a DC signal from a power supply. The μLED then emits a modulated optical signal.

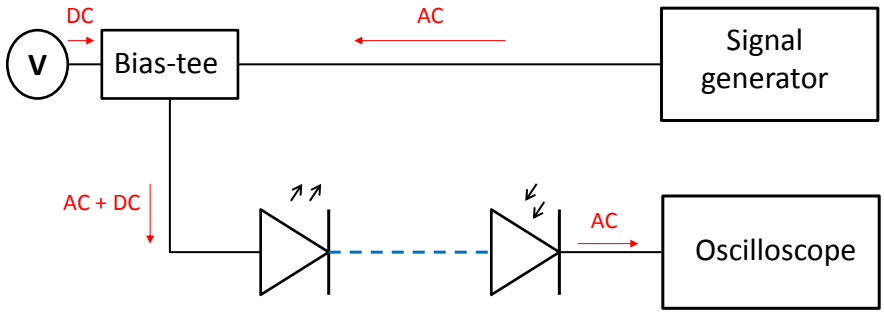

Figure 1.31: Schematic of the typical setup for measuring the data transmission rate from a μLED. the μLED is on the left and the photdiode is on the left.

This modulated optical signal is directed at a photodetector, based on a reverse-bias p-n or p-i-n junction (refer back to Section 1.4 for details). Photons absorbed in the depletion region, which is in the presence of an electric field, generate an electron-hole pair which will drift to the n- and p-type layers respectively causing a flow of electric current. An electron-hole pair generated by a photon outside the depletion region, and so not in the presence of an electric field will recombine and not contribute to any electric current. If a photon is absorbed outside, but close to, the depletion region, the resulting electron-hole pair can drift into the depletion region and contribute to the flow of current. These three situations are depicted in Figure 1.32.

In the work done in this thesis, avalanche photodiodes (APDs) are used to detect modulated light emitted by the μLEDs. APDs are p-i-n photodetectors in which the junction is biased near its breakdown voltage. This means that electrons and holes generated by the absorption of a photon collide with atoms in the crystal lattice of the n-type layer and p-type layer respectively emitting more free carriers, which causes an avalanche effect [80]. The APD is therefore used to convert the modulated optical

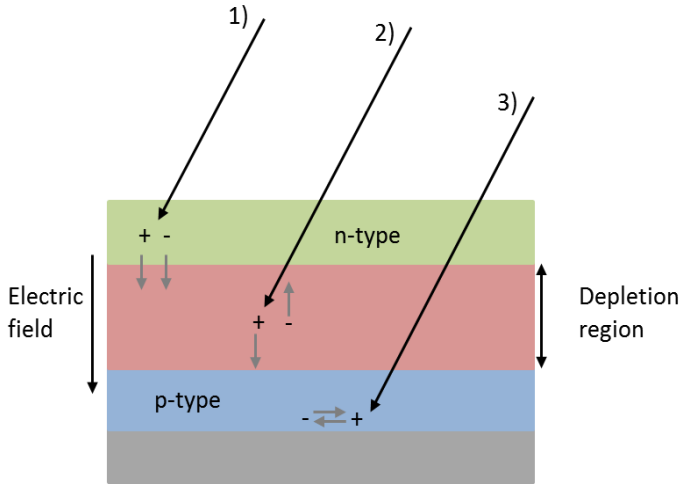

Figure 1.32: Schematic of a reverse-biased avalanche photodiode. Three incident photons are shown. 1) Diffusion of an electron and hole into the depletion region, 2) Absorption of a photon in the depletion region, causing the formation of an electron-hole pair, and 3) the annihilation of an electron-hole pair.

signal emitted by an optical source to an electrical signal. This electrical signal is sent to an oscilloscope and decoded to determine the data transmission rate.

1.9.5 Colour-conversion for white light VLC

As discussed earlier in this chapter, it is anticipated that solid state lighting will replace almost all other sources for lighting over the coming decades [17] as their cost decreases and efficiency continues to grow. With this, VLC capabilities could be added to white light room lighting sources to give them the dual-purpose VLC aims for. These illumination sources, as discussed in Section 1.9, will need to be modulated fast enough to a) not be seen to be flickering by the human eye, and b) to transmit data quickly.

Current solid-state white light sources make use of a blue-emitting GaN-based LED and a rare earth down-converting phosphor to produce white light. The most common phosphor for this is a cerium doped YAG (Ce:YAG), which is suspended in the epoxy dome covering the blue LED, as seen in Figure 1.33 a). The spectrum emitted from an LED with this blue LED/ yellow phosphor combination can be seen in Figure 1.33 b).

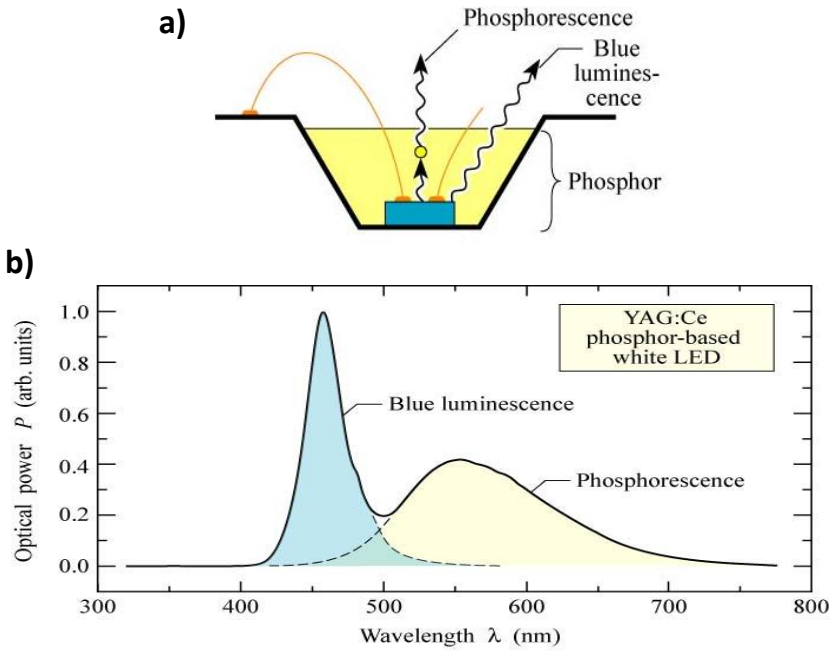

Figure 1.33: a) A blue LED combined with a yellow phosphor to produce white light, as seen in b) the spectrum of the emitted light. Images from [31].

Blue LEDs, even broad area high power ones, have modulation bandwidths on the order of < 20 MHz. These rare earth phosphors, however, have long upper state lifetimes (100s μs) and therefore cannot be modulated fast enough for VLC (according to Equation 1.24). Therefore, in order to create a viable VLC white-light source, alternative colour converting materials must be found.

Colloidal quantum dots (CQDs) have $\approx$ 10s ns fluorescence lifetimes, much shorter than rare earth phosphors, and so are more suitable for VLC applications. They can convert blue light to light across the visible range. These will be discussed in detail in Chapter 4. Fluorescent organic materials are also much faster than rare-earth phosphors. Such fluorescent materials are utilised in the work discussed in Chapter 5.

One advantage other than speed of data transmission is that CQDs are capable of producing light at a higher colour rendering index than a standard phosphor-based white light LED. Figure 1.34 show the colour rendering index for a typical phosphor-

based white LED compared to those made with CQDs and organic materials.

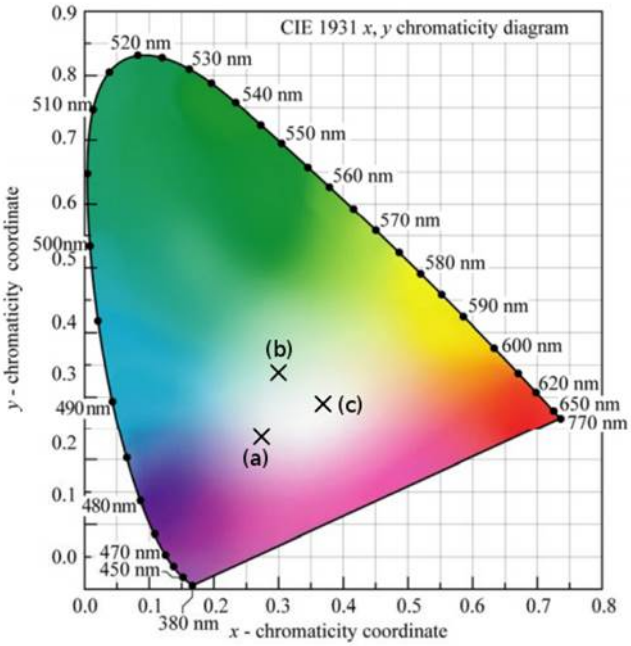

Figure 1.34: The CIE coordinates for a) a phosphor-based white LED, b) a μLED - organic material hybrid [81], and c) a μLED - CQD hybrid [82].

1.10 Summary

This chapter has introduced LEDs and the physics behind their operation. In particular, the III-V semiconductor materials have been discussed with an emphasis on the AlInGaN ternary alloys and their growth for use in LEDs. The μLED was introduced, and the specific capabilities of these discussed in detail. VLC was then introduced, with discussion on how it is used for various state-of-the-art applications. The important features of the of VLC experiments presented in this work, such as modulation bandwidth and data encoding schemes for fast data transmission, have been outlined. The concept of colour-conversion for VLC was introduced at the end of the chapter.

Chapter 2

Mechanics of Micro-Transfer Printing and Associated Device Fabrication

This chapter introduces the micro-transfer printing (μTP) technique. The technique will be discussed in detail, from its beginnings to how it is used in this work. The physical mechanisms behind μTP and how it is used to pick up and print objects will be explained before discussing how we have been using the technique at the IoP and specifically in this PhD work. The device fabrication associated with μTP will then be described. Detailed discussion of the fabrication processes and the tools used will be followed with examples of how the tools are used to fabricate μTP LEDs.

2.1 Introduction to Micro-Transfer Printing

The μTP process is a technique for the heterogeneous integration of pre-fabricated micro- and nano-scale semiconductor devices with non-native substrates. In its simplest embodiment, μTP is analogous to printing ink onto paper with a rubber stamp.

However instead of ink from an ink-pad, small semiconductor devices are picked up from their growth substrate and instead of printing onto paper, a wide range of substrates can be utilised in the μTP process. The μTP technique takes advantage of the ability to manipulate the adhesion forces at the interface between different materials during the pick-up, transport, and printing of nano- and micro-sized structures from their growth substrate to new capability-enhancing substrates. Semiconductor devices are fabricated for μTP such that they can be easily removed from their growth substrate and picked up with an elastomeric stamp. The device is then transported on the elastomeric stamp to a non-native receiver substrate and printed onto it. The stamps required for the pick up, transportation and printing of these small semiconductor devices are fabricated from PDMS (polydimethyl siloxane) or similar elastomeric material. Over the past decade or so, the Rogers group, formerly at the University of Illinois, has pioneered and optimized these stamps and the μTP process [83–85].

One example of how the μTP technique could have an impact is that it has the capacity to print compact, large area arrays of inorganic semiconductor devices onto mechanically flexible substrates, creating arrays of devices no longer limited by the rigidity of their native growth substrate. Since its conception μTP has been used to print such flexible arrays, with μTP of LEDs, VCSELs, photodiodes, and nanowire arrays onto flexible polymer substrates being reported [86–89], some examples of which can be seen in Figure 2.1. Clockwise from top left, this figure shows a flexible LED display on polyethylene terephthalate (PET) [89], an LED array integrated by μTP on PET [83], a flexible micro-needle with μTP LEDs for optogenetics applications [90], and a single LED printed on a flexible polymer substrate [90].

The μTP technique is also promising for realising the integration of III-V optoelectronic components with silicon (Si) circuitry. DeGroot et al. have recently reported μTP for integrating III-V light sources onto an SOI (silicon-on-insulator) waveguide structure [92] and *Loi et.al.* have demostrated μTP-integrated indium phosphide (InP) communications wavelength lasers onto Si substrates [93].

At the Institute of Photonics, colleagues have recently reported the μTP of micro-sized

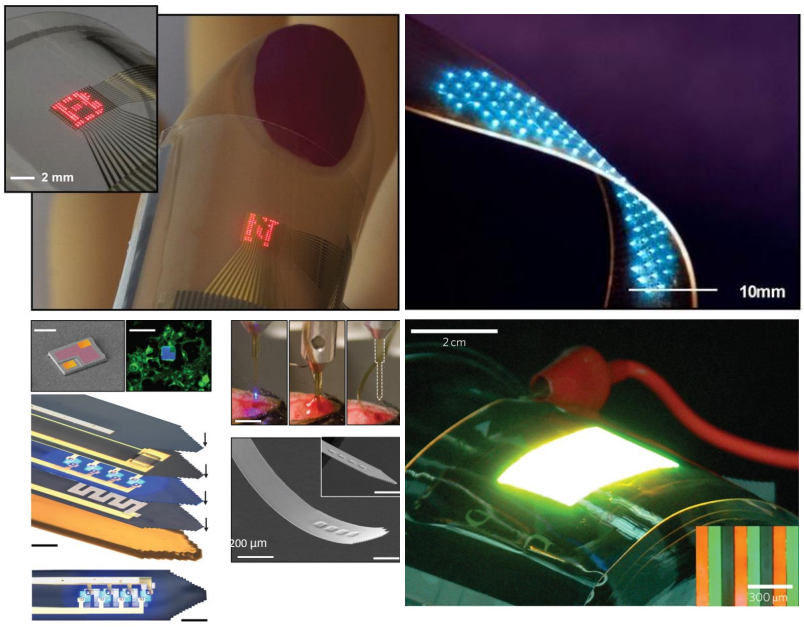

Figure 2.1: A few examples of transfer printing demonstrations on flexible substrates for various applications. Images from [83] and [89, 91]

.

LEDs with nano-scale printing resolution onto unconventional, capability enhancing, substrates [94, 95], and have more recently demonstrated μTP of InP nanowires on different rigid and flexible substrates. One advantage of the ability to print devices without the use of an adhesive interlayer, as in [95] and [96], is that μTP can be executed on rigid substrates (such as diamond) for effective heat transfer to improve the electrical performance of the μTP devices. This will be discussed further in section 4.3.1.

2.2 The Transfer Printing Mechanism

PDMS is used for stamps in μTP processes because of its viscoelastic properties. Viscoelastic materials experience both viscous and elastic characteristics under deformation. While viscous materials resist shear flow and strain linearly with time when a stress is applied, elastic materials strain when stretched and return quickly to their

initial state once the stress is removed. Viscoelastic materials exhibit time dependant strain i.e. they return slowly to their initial state. The more viscoelastic a material, the slower the return is to the initial state.

Viscoelasticity occurs in a material because of a rearrangement of the molecules within it. When stress is applied to a polymeric material, some parts of the polymer chain change position. Polymers will remain solid even when this rearrangement is happening in order to accommodate the stress, creating a built-up back-stress. When the applied stress is taken away, the accumulated back-stress causes the polymer to return to its original form, which occurs slowly. It is these viscoelastic properties that are manipulated in the μTP process to kinetically control the adhesion forces during the transfer of devices.

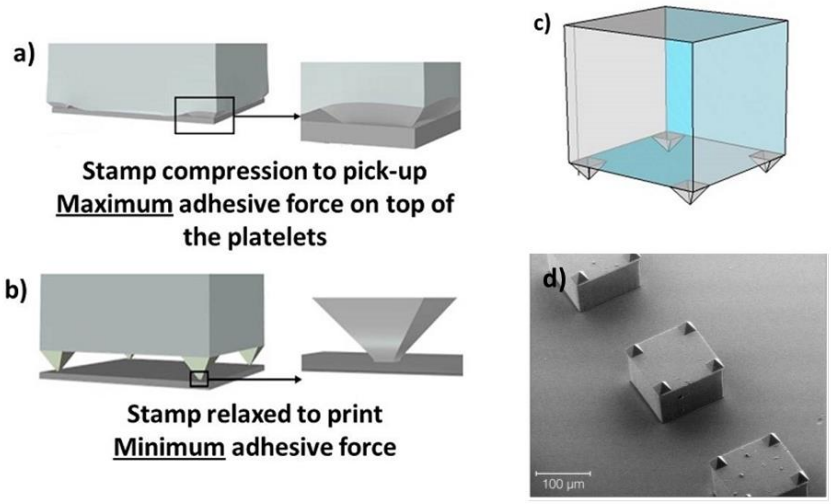

Figure 2.2: Reversible adhesion and geometry of the PDMS stamps used to pick up and print devices in the transfer printing process. The a) pick-up and b) printing conditions are shown, as is a schematic c) and an SEM image d) of the stamp.

During device pick up, the PDMS stamp is pressed into contact with the device and the PDMS conforms to the device surface Figure 2.2a). Because the PDMS is viscoelastic, and it does not return to its initial shape quickly, fast retraction of the stamp picks

up the device. Figure 2.3a) shows the mechanics for device pick-up: the stamp must be retracted quickly enough such that the adhesion between the stamp and device is greater than the adhesion between the device and the donor substrate.

To print the device onto a receiver substrate, the stamp is slowly retracted from the device, Figure 2.2b). This allows the stamp to gently peel away from the device surface and return to its original form, minimising the adhesion force [97].

While the slow retraction of the stamp minimises the adhesion force, the adhesion force between the device and the receiving substrate must be greater than that between the stamp and the top of the device for the device to be released. This requires the contact area on the top of the device to be less than that on the bottom of the device. This can be achieved with careful stamp design. Figure 2.3b) shows the mechanics for device printing: the stamp must be peeled up from the device so as the adhesion between the device and the receiver substrate is greater than the adhesion between the device and the stamp.

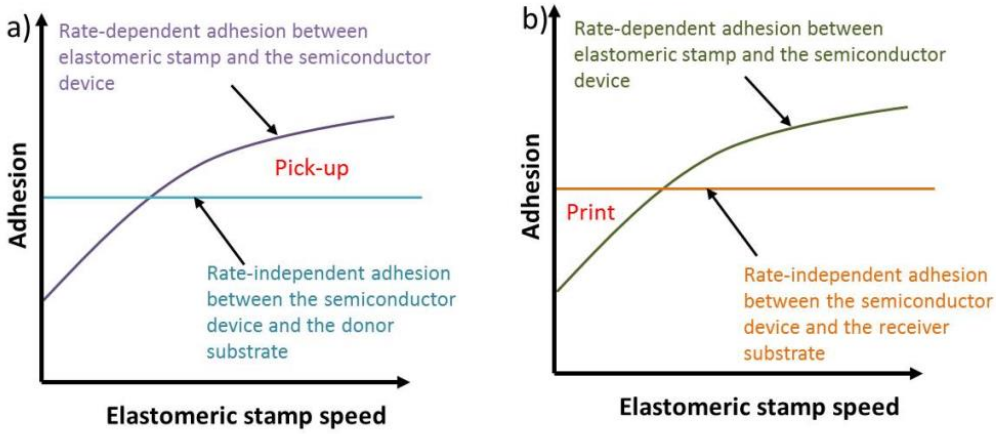

Figure 2.3: The mechanics of device a) pick-up and b) printing.

The geometry of the elastomeric stamps used throughout this PhD, and as illustrated in Figure 2.2 c), is a cubic main body with a pyramidal protrusion on each of the bottom corners.

The introduction of compressible pyramidal protrusions on the stamp means that the contact area between the stamp and device can be altered as desired [83].

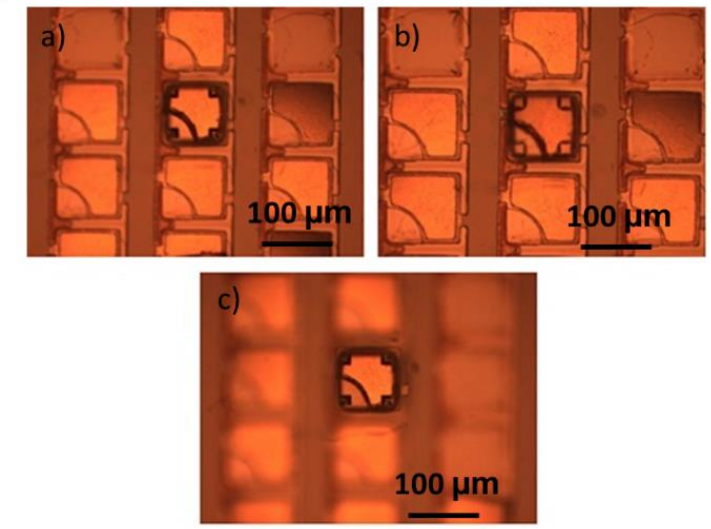

Figure 2.4: Microscope images of a section of an LED array as an LED is being picked up. a) The stamp is slowly brought into contact with the LED and compressed until "roof collapse" can be seen as in b) and, after fast retraction, the LED is picked up as in c).

During pick-up, these pyramids are compressed into the device until the stamp roof (the area between the pyramids) is collapsed ("roof collapse") maximising the contact area. This is seen in Figure 2.2 a). Once the roof of the stamp has fully collapsed, the stamp is retracted quickly away from the donor substrate. The PDMS does not have time to react and the device is pulled up with it. After device pick-up the pyramids on the bottom of the stamp push the device out and the roof relaxes back to its original shape. However, the viscoelastic nature of the stamp means the pyramid tips have enough adhesion to keep hold of the device. When the device is placed on the receiver substrate, adhesion becomes greater between the substrate and the back of the device than between the pyramid tips and the device because of the difference in surface area. This situation is seen in Figure 2.2 b). The device can therefore be released onto the receiver substrate. Microscope images of device pick up; from contact, to "roof collapse", to quick retraction of the stamp (which picks-up the device) are seen in Figure 2.4. Here we are using the system to be described in Section 2.4 below which

contains a camera allowing a top-down view through the transparent stamp as the printing process proceeds.

2.3 Elastomeric Stamp Fabrication Process

The 100 × 100 μm^2 stamps are fabricated, as in Figure 2.5, by first producing a hard mould on a Si substrate before infilling with liquid PDMS. The fact that potassium hydroxide (KOH) can be used to etch square mask features producing pyramidal recesses into the silicon is exploited to fabricate the hard mould for PDMS infilling.

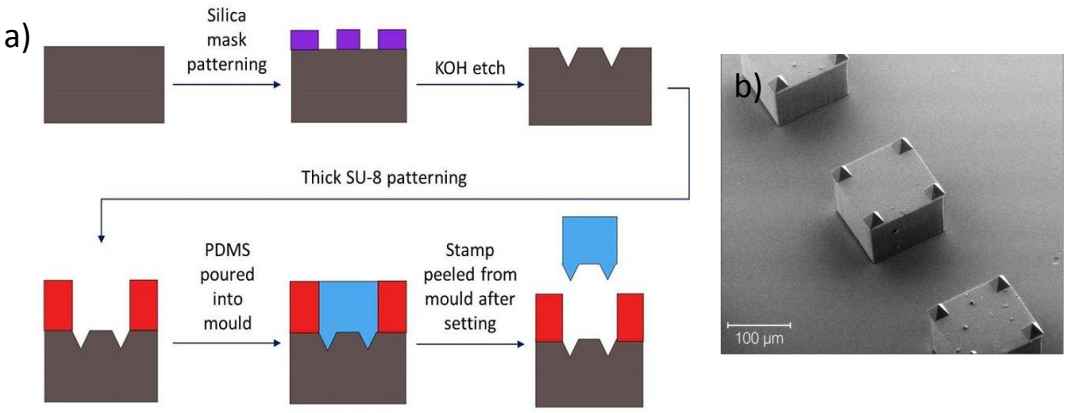

Figure 2.5: a) A schematic of PDMS stamp fabrication process on a silicon substrate (grey) and b) an SEM image of the stamps used in this work, taken from the bottom surface to show the pyramid tips.

KOH etches different Si planes at different rates and so can be used to selectively etch it in one crystal direction. Si(111) planes etch around 100 times slower compared to the other orientations, and therefore Si will be etched quickly in all directions until the Si(111) plane is reached [98]. This means that aligning mask features to certain crystallographic planes can induce different etch geometries in the Si. As just mentioned, square mask features will produce pyramidal recesses where the angle between the surface planes and recessed sidewalls is 54.7°.

The stamp fabrication process begins by masking a Si wafer with a layer of SiO_2 before pattering with features correctly aligned to expose the desired crystallographic planes. The protective SiO_2 is etched through, see Figure 2.5, and the Si (100) planes are exposed and wet etched using an alkaline potassium hydroxide (KOH) solution, creating the pyramidal protrusions. Full details on the etching mechanism involved in this KOH wet etch of Si can be found in Section 2.6.4.

After building a hard mould for the main body of the stamp with SU-8 (a photoresist), liquid PDMS is poured into the mould and allowed to solidify overnight. The PDMS can then be peeled from its mould, completing the fabrication process. .

PDMS is transparent, conformable, and non-toxic and so ideal for stamp fabrication. It is made of long siloxane polymer chains which, combined with its high molecular weight, make it unusually highly viscoelastic [99]. PDMS comes as a two-part liquid compound that will cure, over time, at room temperature. It is supplied as a PDMS base material (RTV615A, Silicone solutions) and a curing agent (RTV615B, Silicone solutions) When mixed with the appropriate curing agent, the polymer chains in the PDMS base material increase in length, increasing the viscoelasticity of the PDMS. The flexibility (or rigidity) of the PDMS stamps can therefore be tailored by adapting the ratio of PDMS base material to curing agent to give the best pick-up/release characteristics. To fabricate the stamps used in this work, the PDMS base material is mixed with its curing agent in a weight ratio of 8:1, poured into the mould and left to set overnight. Once set, the stamp is peeled from the hard mould for use in the μTP process.

2.4 Micro Transfer Printing with a Modified Nanolithography System

For the μTP presented in this work, a modified nanolithography system (Nanoink NLP 2000) is used to pick-up, transfer and print 100 μm x 100 μm InGaN-based blue-emitting

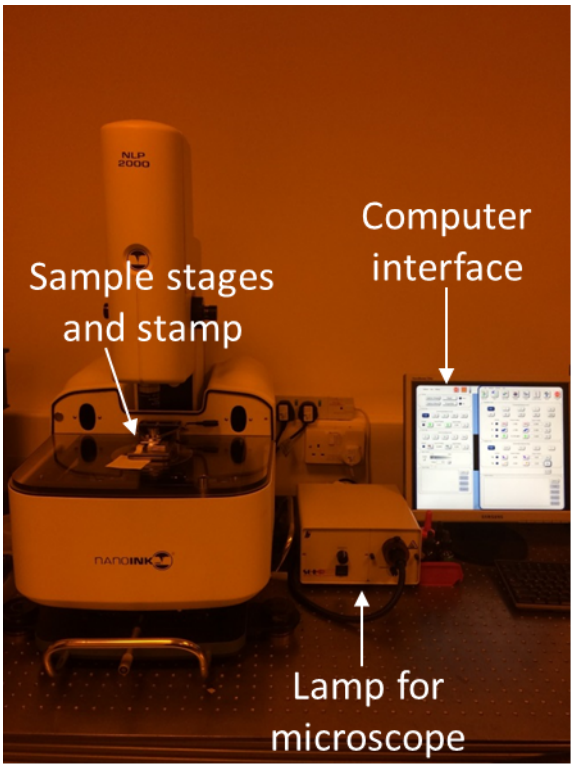

Figure 2.6: The NLP setup in the lab. Sample stages, and the computer interface can be seen.

μLEDs (see Section 2.5 for details). The NLP was designed to ink different areas of a substrate via an atomic force microscopy (AFM) tip. This tip could be dipped in liquid-filled reservoirs and the liquid precisely deposited onto a sample, with nanometre precision, through the positioning of very accurate piezoelectric sample stages. This system has large area scalability, and is capable of printing over an area of 10 cm x 10 cm. The NLP piezoelectric stage positioning is controlled by a computer interface, seen in Figure 2.6. The magnified image of the samples on the stage can be seen in real-time through an integrated microscope system of magnification 20×.

This NLP tool has been modified for μTP to hold the elastomeric stamps (fabricated as in Section 2.3) in the place of the AFM tip the machine originally held. Because the PDMS stamp is transparent, the printing process can be viewed and recorded through it with the integrated microscope on the NLP system. The modifications to the NLP

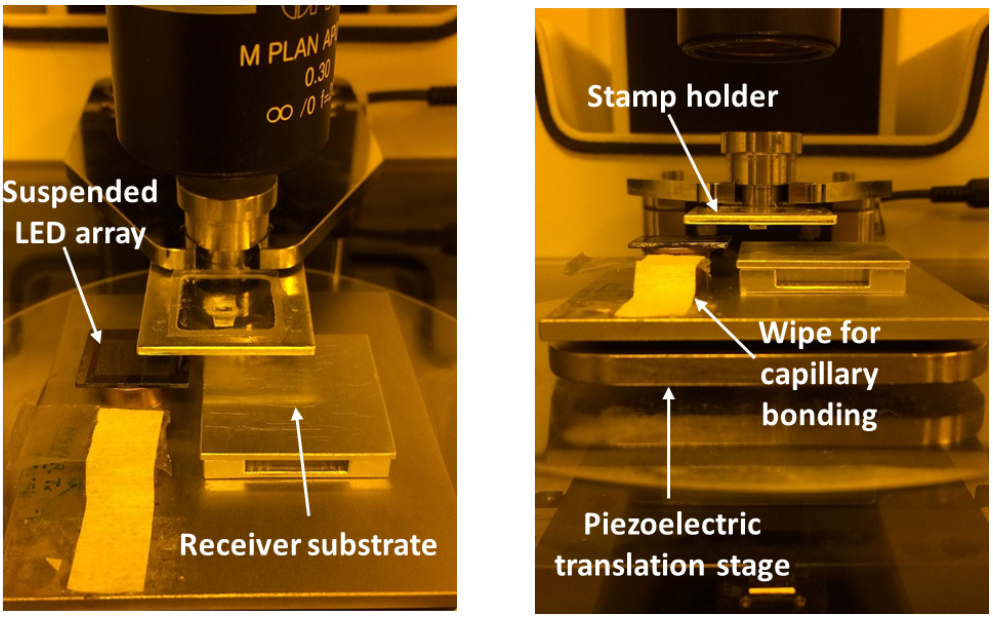

Figure 2.7: NLP toolhead modified for the μTP process.

tool for μTP can be seen in Figure 2.7. The stamp holder can be seen, above the positionable sample stage. Instead of picking up liquid from a reservoir and inking it onto a reciever substrate, the system is now used to pick up semiconductor devices and "print" them onto a reciever substrate, taking $\approx$ 30 s per pick-up and printing step. This, combined with the piezoelectric stages which move the sample staging, allows for nanometre printing precision which has been reported down to $\pm$25 nm by Trindade et al. at the Institute of Photonics [94] using this NLP tool. As demonstrated in this work, the NLP has the potential to print large area arrays of closely packed LEDs with very high placement precision. This is, to our knowledge, the most precise μTP system yet developed - compared to previous best printing precision between 3 μm and 1 μm [100, 101]. A data sheet for the NLP tool can be found in the appendices at the end of this thesis.

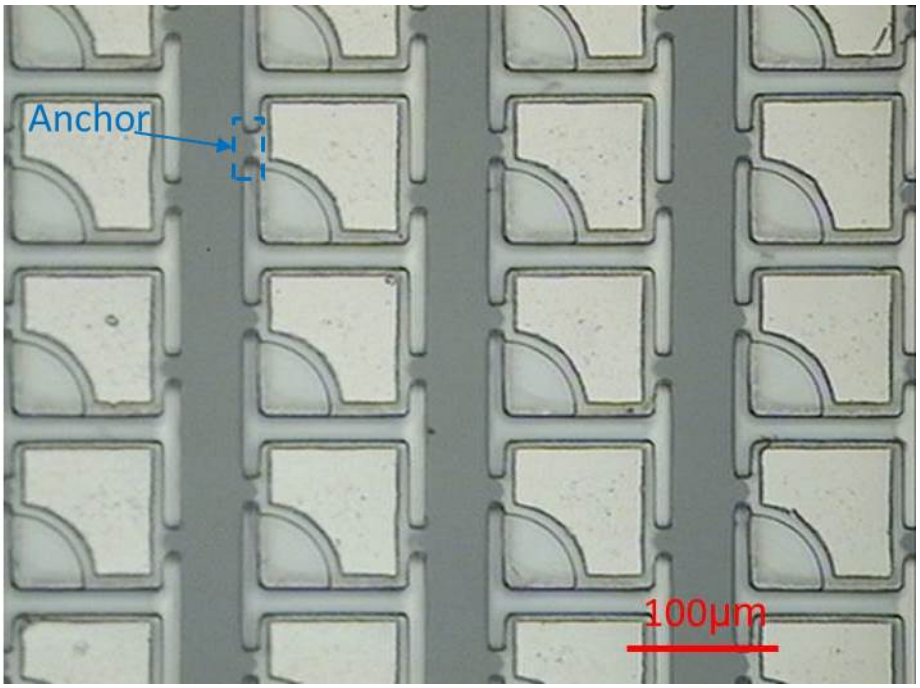

Figure 2.8: Microscope image of a suspended LED array. The anchors attaching the devices to the growth wafer are shown upper left and bottom right for each μLED. The n-mesa is lower left in each case and of quarter disk format.

2.5 Suspended LED Fabrication Process Flow

For the work presented here, arrays of ultra-thin (2 μm thick) 100 μm x 100 μm GaN-based μLEDs were fabricated for the μTP process that are easily removed from their growth substrate (Figure 2.8). The underlying silicon substrate is removed, leaving an array of μLED membranes suspended on sacrificial anchors designed to break when a force is applied with the PDMS stamp during device pick up.

A plan view image of a section of an array of these μLEDs, suspended in air by sacrificial anchors is seen in Figure 2.8. The μLED pixels match the size of the PDMS stamp used in the μTP process. The μLED fabrication is described in the remainder of this chapter, after a description of the fabrication tools and techniques used.

The rest of this chapter will now describe the process flow of μLED fabrication. For

simplicity, Figure 2.10 shows the process flow for the fabrication of a single one of these ultra-thin suspended μLEDs from a fabricated array of thousands (supporting anchors are not shown).

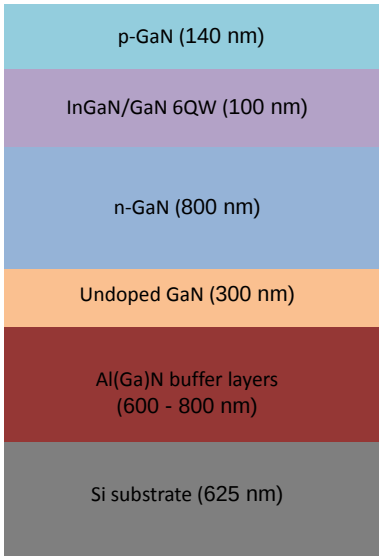

Figure 2.9: Schematic of the as-grown GaN-on-Si wafer used for suspended μLED fabrication.

The μLEDs are fabricated from a GaN-on-Si(111) wafer, grown by Plessey semiconductors. A (not-to-scale) schematic of this wafer is shown in Figure 2.9.

This wafer is first diced into 1.5 cm x 1.9 cm chips to match the photolithography masks used in the process. The array of μLEDs is then fabricated on one of these chips.

The first step in the μLED process is to etch an n-mesa to access the n-GaN layer and therefore the pn junction. This is done with an inductively coupled plasma (ICP) etch. Once the n-mesa is etched, a protective layer of SiO_2 is deposited with the plasma enhanced chemical vapour deposition (PECVD) tool.

A deep reactive ion etch (RIE) is then performed through the protective SiO_2, InGaN LED epilayers, and 7 μm into the Si substrate. This is done to define the supporting anchors and will allow KOH to access and attack the Si substrate during the following

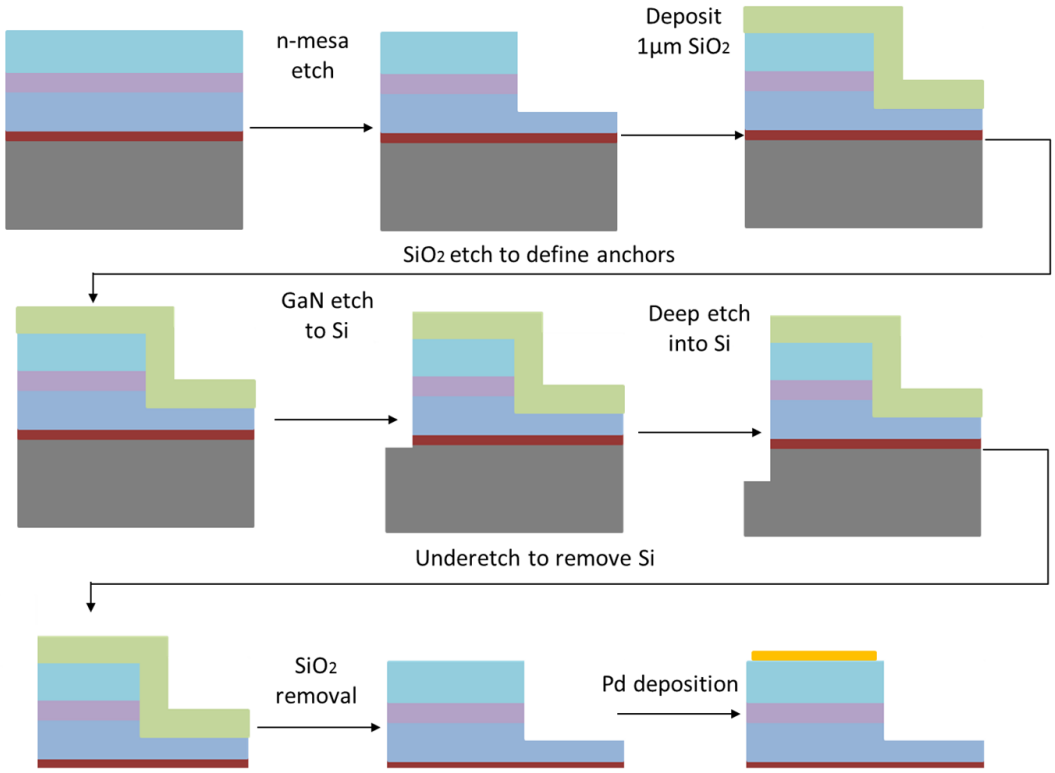

Figure 2.10: μTP μLED fabrication process flow for μTP. The respective layers are Pd (yellow), SiO_2 (green), p-GaN (teal), MQWs (purple), n-GaN (blue), AlGaN buffer layers (red), and Si substrate (grey).

wet etch process.

The Si substrate is removed from underneath the μLED pixels using a hot KOH underetch. This leaves just the InGaN μLED epilayers suspended on two sacrificial anchors, as indicated in Figure 2.8.

Once the μLEDs are suspended, a 90 nm Pd layer is deposited on the sample with the electron-beam (e-beam) deposition tool. This is then patterned and etched in an RIE process to define the current spreading layer. The metal is then annealed at 305°C to form a contact on the p-type GaN with low resistivity, completing the suspended μLED fabrication process, and the μLEDs are ready for μTP.

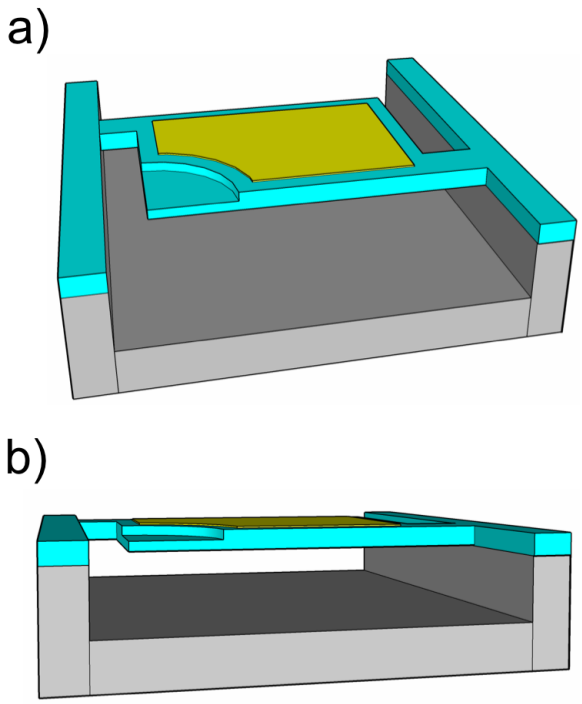

Figure 2.11: a) and b) Schematic representation of a suspended μLED pixel seen from two different angles. This μLED is 2.4 μm thick, and 100 x 100 μm in size.

Figure 2.11 shows a schematic of a single suspended μLED as fabricated in the process seen in Figure 2.10.

2.6 Cleanroom processes for LED fabrication

2.6.1 Photolithography

Photolithography is a common technique in the semiconductor industry for pattern definition. It uses light to transfer patterns from chrome and glass masks to photosensitive materials known as photoresist (PR). Upon exposure to UV light, the chemical composition of PR changes and reacts with a corresponding developing solution differently to unexposed PR. Therefore with a patterned mask placed between the PR

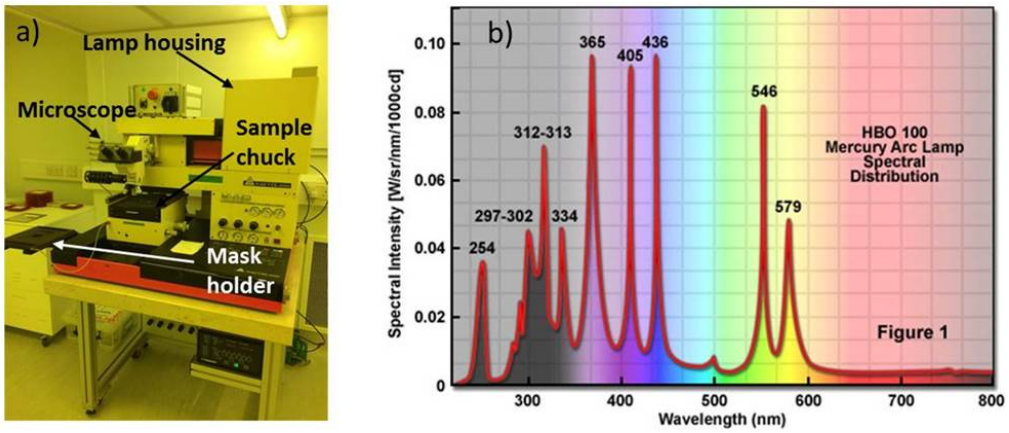

Figure 2.12: a)Photograph of the MA6 mask aligner used for photolithography and b) a typical spectrum of a high pressure mercury vapour arc-discharge lamp [102].

coated sample and the UV light, blocking certain areas from being exposed, the PR becomes patterned. This PR acts as a protective mask in subsequent etching steps.

There are two types of PR, positive and negative. Positive PRs are changed by exposure to UV light such that they will dissolve in suitable developer. The areas to be removed are therefore unmasked during UV exposure. Conversely, negative PR becomes cross-linked upon exposure to UV light, while the unexposed regions will be washed away in developer. This means that regions on a sample to be covered with the resist pattern are left exposed to the UV light by the mask. For most of the steps in the μLED fabrication process outlined here, the pattern is defined with a negative PR (Microresist Technology, MA1410).

In regular photolithography, such as that used throughout this work, the resolution (R) is given as :

$$R \propto \frac{\lambda}{NA} \tag{2.1}$$

where NA is the numerical aperture of the mask aligner, and λ the wavelength of the light.

In the cleanroom we use a Karl Suss MA6 mask aligner, a photograph of which can be seen in Figure 2.12 a). This consists of lamp housing, a microscope system, and

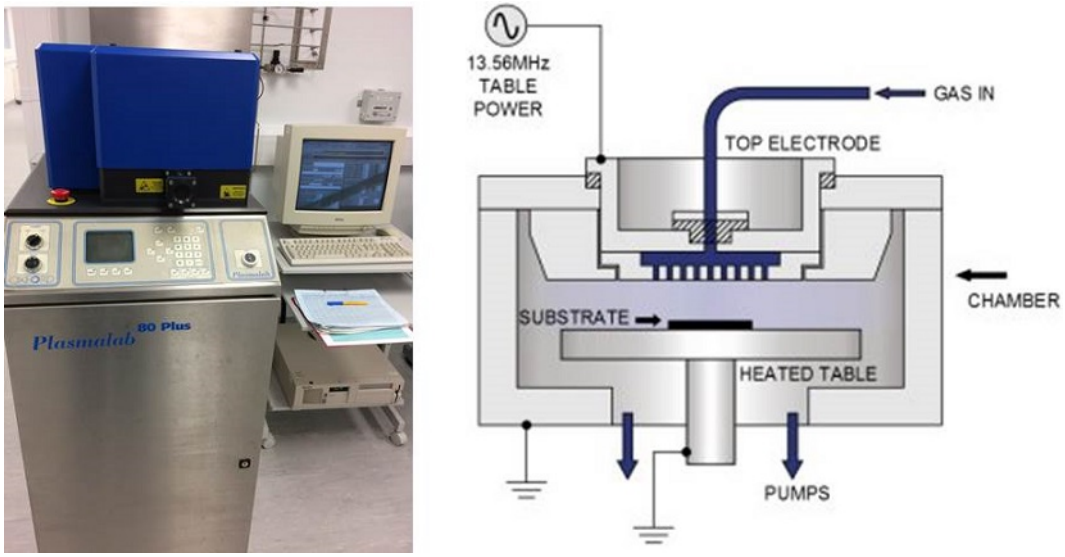

Figure 2.13: Photograph of the PECVD machine used in the cleanroom, and a schematic diagram of the chamber. Schematic taken from [103].

sample chuck and mask holder. The microscope in this mask aligner is used to view both the mask and the sample simultaneously and align the pattern on the mask to the desired area on the sample (usually with the help of pre-patterned alignment marks). The sample chuck can be moved in the x, y and θ direction to give precise alignment.

The lamp housing accommodates the UV light source - a high pressure mercury discharge lamp - and the associated electronic circuitry. A typical mercury arc-discharge lamp spectrum is seen in Figure 2.12 b). The wavelength of this lamp centres around 350 nm-450 nm and so the minimum resolvable feature size for patterns made with this mask aligner is 2μm (see Equation 2.1).

2.6.2 Plasma Enhanced Chemical Vapour Deposition

In our cleanroom, an Oxford Instruments plasma enhanced chemical vapour deposition (PECVD) tool [103] is used to deposit dielectric layers, such as silicon dioxide (SiO_2) and silicon nitride (SiN_x), on samples for use as an insulation layer or a hard mask for subsequent etching steps.

The PECVD chamber consists of two electrodes; one heated bottom electrode on which the sample sits, and an RF driven top electrode. Gas is injected into the chamber via a "showerhead" on the top electrode and a plasma is generated between the two electrodes, see Figure 2.13.

The PECVD system is primarily used to grow SiO_2 on the surface of samples. This is done via an interaction between silane (SiH_4) and oxygen (O_2) which are injected separately into the PECVD chamber through the showerhead on the top electrode. The bottom electrode, on which the sample is placed, is heated to 300°C and the following surface reaction occurs:

$$SiH_4 + O_2 \rightarrow SiO_2 + 2H_2 \tag{2.2}$$

This leaves a layer of amorphous SiO_2 on the sample surface [104].

In the suspended μLED fabrication process, after etching the n-GaN mesa, the sample is coated in a 1 μm thick layer of SiO_2. This is done with a 170 sccm SiH_4 and a 750 sccm N_2O (to provide the oxygen as in Equation 2.2) flow at 300°C. This SiO_2 layer acts as a protective hard mask in subsequent etch steps, as described in section 2.6.3. It also supports the fragile LED epilayers during the underetch to remove the silicon substrate (see section 2.6.4).

2.6.3 Plasma Etching

Plasma etching is used for its anisotropic nature and the production of vertical sidewalls. In a plasma etch, a material is exposed to gaseous etchants which remove the exposed surface by either physical bombardment or chemical reactions [105]. In our cleanroom facilities at the IoP, we have two different types of plasma etch tool: reactive ion etch (RIE) and inductively coupled plasma etch (ICP).

Reactive Ion Etch

An RIE chamber contains two parallel platens between which a plasma is initiated, see Figure 2.14. This plasma is initiated by exciting the reactive gases within the vacuum chamber with radio-frequency (RF) electromagnetic fields (typically 13.56 MHz). These RF fields generate highly reactive ions from the process gases, and these ions etch the surface of the sample using a combination of physical (due to the kinetics of ion bombardment) and chemical reactions. The RIE etch is known for the production of vertical sidewalls, due to the anisotropic nature of this etch and the directionality of the ion bombardment, while chemical bonds from the exposed material are broken by the chemical etch process.

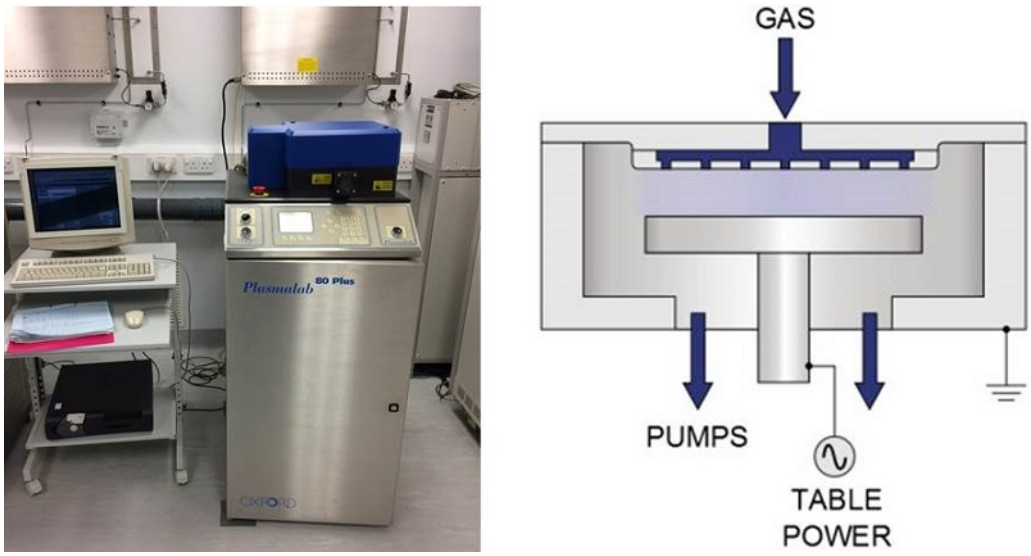

Figure 2.14: A photograph of the Oxford RIE tool used in the cleanroom and a schematic of the workings of a typical RIE machine [106].

Inductively Coupled Plasma Etch

The ICP tool is a modified RIE system with an inductively coupled plasma source and a radial induction coil design, as seen in Figure 2.15. Varying magnetic fields generated in the coil by induction can generate higher density plasmas than the RIE system,

resulting in faster etching rates. In the photograph in Figure 2.15, we see the sample loading chamber at the front of the machine. The sample is loaded into the ICP via this chamber on a silicon carrier wafer and then (after pumping down) the carrier wafer and sample are automatically loaded into the ICP chamber and the etch process is initiated.

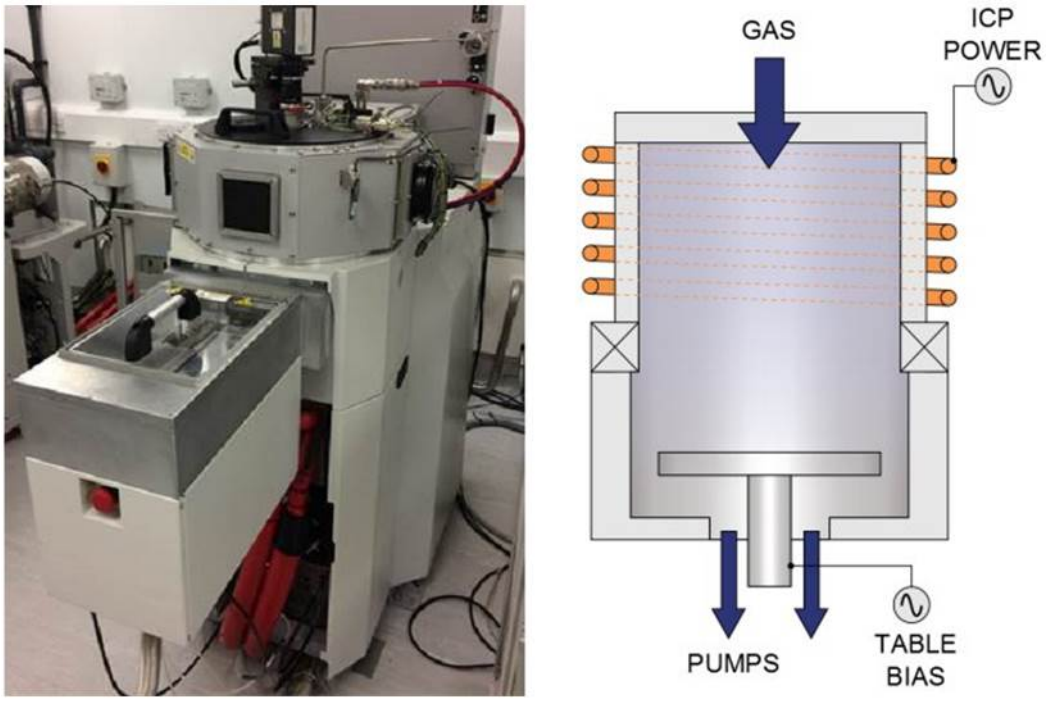

Figure 2.15: Photograph of the ICP used in our cleanroom and a schematic of a typical ICP machine [107].

Plasma etch: suspended LED fabrication

In order to suspend the devices on supporting anchors, the silicon substrate must be accessible to the KOH used in the under-etching process. The SiO_2 masking layer is etched by an Ar and CHF_3 containing RIE etch. This etch is done with a platen power of 200 W at room temperature. The ICP is then used during a room-temperature deep etch step to etch through the GaN epilayers, define the anchors (see Figure 2.8), and access the underlying Si. A Cl_2 flow at a rate of 50 sccm is sent into the chamber

between a coil power of 700 W and a platen power of 300 W to strike the etch-plasma. The third stage in the deep, anchor-defining, etch process is to etch ≈ 7 μm into the Si substrate. An RIE etch containing Ar (10 sccm), O_2 (10 sccm), and SF_2 (60 sccm) is used for this. These deep etch steps deep etch allows a subsequent KOH wet-etch to penetrate the Si substrate and under-etch the devices, suspending them on the defined supporting anchors. This KOH underetch will be described in the following section.

2.6.4 Wet chemical etch

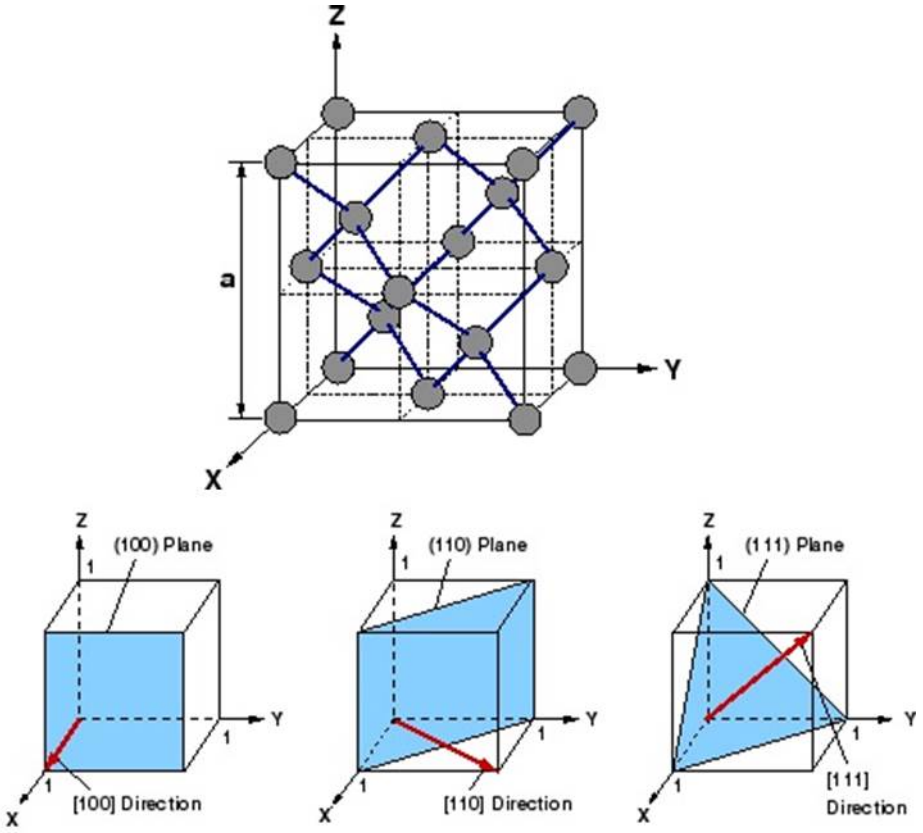

Figure 2.16: The crystal structure of silicon. The main crystallographic planes in silicon are shown in blue in the bottom three images. Images from [108].

Wet etch methods are typically faster than the dry etch methods discussed in Section 2.6.3, but they have less controllable etch rates. While dry etch processes are used for their isotropic etching and therefore the production of vertical sidewalls, wet etches can

be used to exploit anisotropy, such as that certain crystallographic planes of materials etch faster than others in certain chemical etchants. This is illustrated by the etching of pyramidal recesses through a square mask in the stamp fabrication process as discussed in Section 2.3.

Si has a diamond cubic crystal structure, as seen in Figure 2.16, with the main crystallographic planes relevant to this work shown in blue.

The low-index planes - (100), (110), (111) - and their position in the crystal lattice are represented in Figure 2.16. This allows an anisotropic etch to occur when fast etching planes are exposed to KOH.

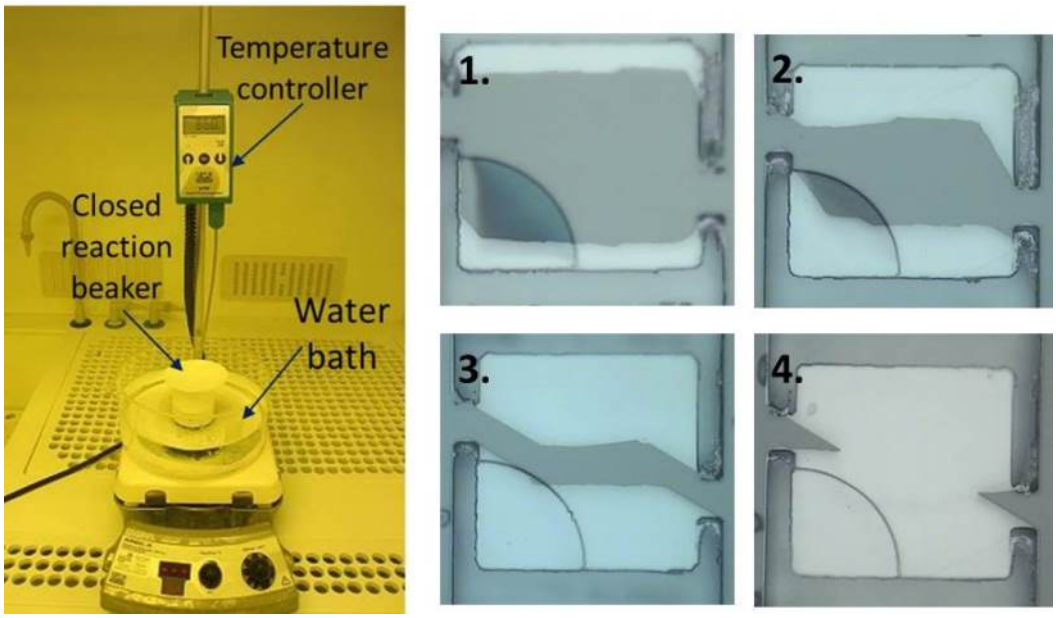

Figure 2.17: a) The setup used in the wet underetch process. b) Microscope images of a single 100 μm x 100 μm LED at 10 minute intervals during the underetch process proceeding from images 1-4.

During the LED fabrication itself, the LEDs are under-etched to remove them from their Si(111) growth substrate. The mask is aligned such that the KOH etch progresses normal to the (110) plane and the (111) planes effectively stop the etch preventing unwanted lateral etching [109]. The under-etch is done using a hot KOH solution, 60:40 KOH and deionized water at 85°C, using the recipe from [110]. The devices are placed

into this solution for around 45 minutes until completely suspended on their anchors. A setup of this underetch process can be seen in Figure 2.17 a). The temperature of the water-bath can be precisely maintained at 85°C using the temperature controller. This is important to keep the etch rate constant. Equally important is the constant agitation of the KOH solution throughout the 45 minute etch with the etch reaction beaker kept covered to help maintain a constant temperature and minimise evaporation of the etchant. The progress of the etching of the fast-etching planes can be seen in Figure 2.17 b) at 10 minute intervals during the underetch, with the dark areas showing where there is (still) underlying Si, and the lighter areas where the Si has been etched away.

Once fully underetched, the LEDs are left suspended on the two supporting anchors as previously described. An image of these fully underetched LEDs can be seen in Figure 2.8. During GaN LED wafer growth on Si, a few monolayers of SiN_X are formed between the Si and III-V materials, this acts as an etch stop and leaves a smooth undersurface on the μLED platelets for μTP.

2.6.5 Wet chemical etch: Wafer bowing

As discussed in Section 1.6.2 there is a significant lattice mismatch when growing GaN-on-Si wafers, such as those used for the suspended μLED fabrication. Another significant challenge when growing III-nitride LED epilayers on Si is that the sequential MOCVD growth required to produce the LED MQW epilayer structure creates multiple competing compressive and tensile strains between layers. Strain compensation engineering is done at growth level to account for this and grow high quality LED epilayers. There is also a large difference in thermal expansion coefficients between GaN and Si, which must be compensated for during growth (as discussed in Section 1.6.2). Also, dopant impurities for n - and p -type GaN, Si and Mg respectively, introduce large tensile strain into the material [111, 112]. To address this tensile strain and consequent cracking, the inclusion of AlN and AlGaN layers has proven effective. These graded

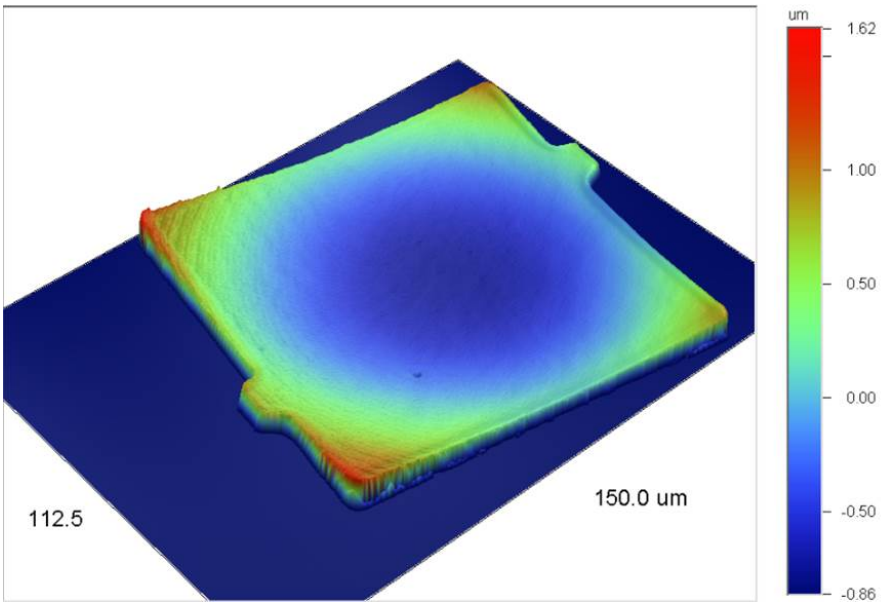

Figure 2.18: A 100 μm x 100 μm LED platelet imaged on an optical profiler, the colour scale shows the varying heights across the platelet.

strain compensation layers however mean that subsequent GaN layers are highly compressively strained. The idea of these AlN and AlGaN strain compensation layers is to introduce enough compressive strain into the structure to counteract the tensile strain introduced in the various ways outlined above. The larger in-plane lattice constant of GaN compared to AlN means the strain compensation layers of AlGaN will be under compressive strain when grown on relaxed AlN substrate-to-epi interfacial layers. This compressive stress induces convex bowing of the Si wafer counteracting concave bowing (caused by the difference in thermal expansion coefficients) upon cooling down after growth. During growth, continual compressive strain is introduced by the growth of the AlGaN buffer layer and the subsequent Si-GaN layer bowing the wafer. The thick silicon substrate acts to counteract this bowing, and pull the wafer flat. However, the Si substrate must be removed to suspend the devices for μTP and this causes the strain compensation to relax, bowing the device. This bowing of the device is seen in the optical profiler image in Figure 2.18. Only the central part of the device is in contact with the receiver substrate.

2.6.6 Electron Beam Deposition

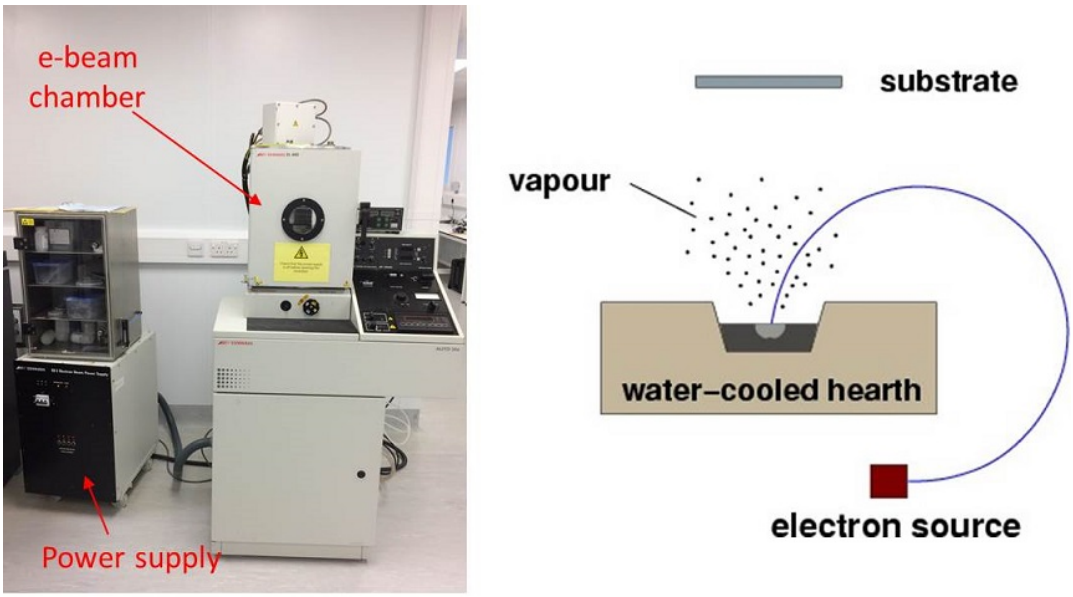

Figure 2.19: The e-beam deposition tool used in this process and a schematic of metal deposition.

Metal deposition during the LED fabrication process can be done with an electron-beam evaporation(e-beam) system. Here, a tungsten filament is heated when a current is passed through it, causing thermionic emission of electrons from the filament. The electron beam is then accelerated by a set of magnetic plates and directed towards a crucible containing solid pellets of the desired metal. The high energy in this beam of electrons causes the metal to heat up, evaporating the metal, and coating the surface of the sample. Figure 2.19 shows this pictorially. By controlling the current supplied to the filament, the deposition rate can be controlled.

A 90 nm Pd current spreading layer is deposited on the 2 μm-thick LEDs after under-etching to allow charge to be efficiently and evenly injected into the p-type GaN. Once deposited, the current spreading layer is etched in an RIE process and covers most of the top surface of the p-type GaN as shown in Figure 2.8.

2.6.7 Sputter Deposition

To deposit metal thicker than around 100 nm, as is required for bonding pads and metal tracks to address the μLEDs, a metal sputter deposition tool is used. This is a physical vapour deposition technique where metal is transported from a large area solid metal target under positive ion bombardment and coats samples in said metal.

In a high-pressure vacuum chamber, argon gas is turned into a plasma of Ar^+ ions. These ions strike the negatively charged target which contains the metal to be evaporated. As a result of these collisions, metal atoms are ejected from the target and arrive at the sample.

After the deposition of an electrical insulation layer, thick metal tracks are deposited via sputtering to electrically address the μLEDs after μTP. These are of 50 nm/200 nm Titanium/Gold (Ti/Au) in all of my devices presented in this thesis, but 50 nm/ 300 nm Ti/Aluminium (Al) for some test samples. One fully addressable μLED array on glass, with Ti/Au tracks can be seen in Figure 2.20. These tracks go from the p- and n-pads on the μLEDs themselves, out to large bonding pads, seen in Figure 2.20 in the outer two rings of bonding pads.

2.7 Summary

In this chapter, the μTP technique has been introduced. The mechanics behind μTP have been discussed, including the adhesion forces required for the pick-up and printing of μLED devices from their native substrate to non-native substrates. The elastomeric stamps required for μTP have been discussed, including the fabrication process used to produce the stamps used for the μTP in this work. The NLP system used to facilitate the μTP in the work presented in the following was also discussed. The latter part of this chapter focussed on the cleanroom fabrication tools and techniques required for the fabrication of the suspended arrays of 100×100 μm^2 μLEDs used in this work.

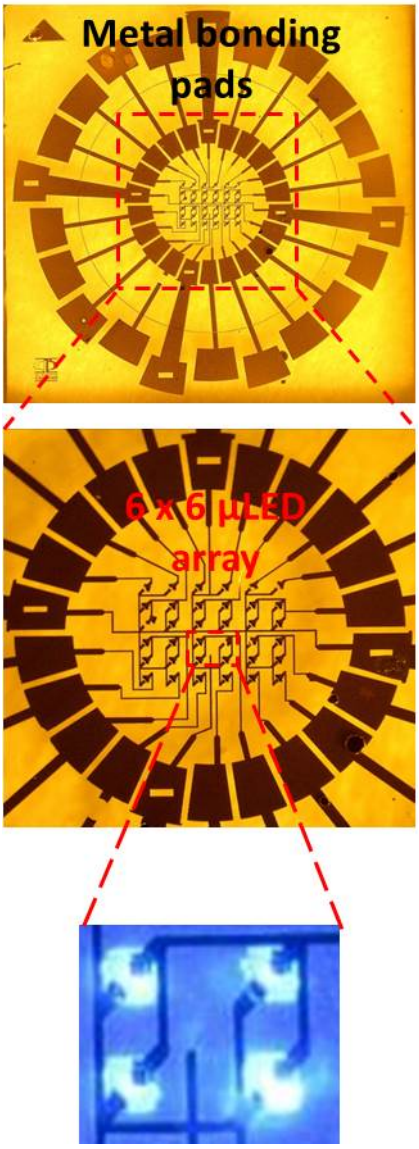

Figure 2.20: a), b) Layout of the metal tracks for a 6x6 array of μTP μLEDs. The μLEDs are printed within the dashed red box. c) A close-up photograph of the μLED array printed on glass. Each μLED is 100×100 μm^2.

Chapter 3

Dual-Colour Integrated μLED Device

In this chapter, a μTP-enabled integrated dual-colour μLED device is introduced, comprising a 2 x 8 array of alternating green- and blue-emitting InGaN-based μLEDs on a single chip. First the motivations behind this dual-colour device are explained, before going on to describe how the device is fabricated. A description of the characterisation of the dual-colour device will then follow - first the two different coloured μLEDs are characterised separately, then the dual-colour device is characterised with both μLEDs driven simultaneously.

This dual-colour μLED device is designed for VLC applications, and so the characterisation of the device for such purposes will also be explored here. The modulation bandwidth of the device is measured, both for the two μLEDs separately, and for the combined dual-colour μLED device. The device is demonstrated in two different data transmission regimes which will be described, with data transmission rates measured under various driving conditions.

3.1 Multi-Colour VLC

As introduced in Section 1.9, due to their low cost, high efficiency, and high power, GaN LEDs have been crucial in enabling the development of solid state lighting. They also benefit from high modulation bandwidths, making them attractive candidates for VLC applications. This chapter deals with the fabrication and characterisation of an integrated dual-colour LED device for VLC.

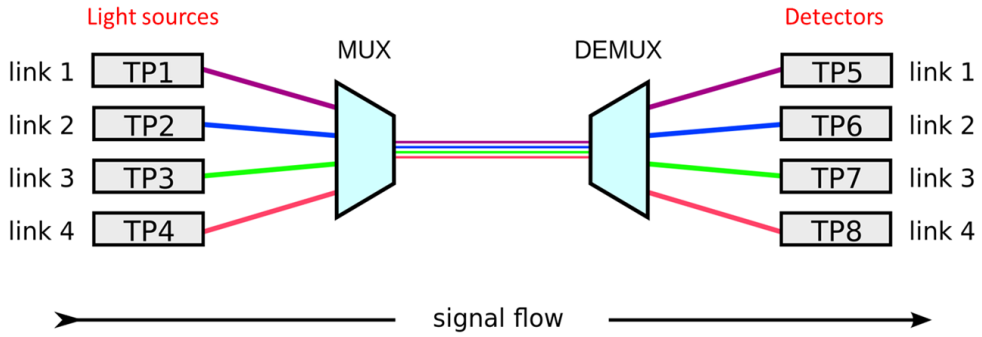

Figure 3.1: Wavelength division multiplexing. Here TP means transponder. MUX and DEMUX mean multiplexed and demultiplexed, respectively. Image from [113].

In VLC it is often advantageous to have multiple different light sources with different emission wavelengths. This is because with one light source, only one stream of data can be sent at any one time. Multiple sources with multiple discrete wavelengths can be used to send multiple streams of data simultaneously, as shown schematically in Figure 3.1. This approach is often used in fibre-optic technology, at near IR wavelengths, and is known as wavelength division multiplexing (WDM). Multi-colour communications are also widely utilised in VLC research with work being done to increase the capacity of low-cost LED plastic optical fibre (POF) links using WDM [114, 115] with results of combined data rates of 11 Gbps having been reported from four LEDs (red, blue, green and violet) along 10 m of POF. Free-space multi-colour VLC has also been demonstrated, with over 10 Gbps demonstrated over 1.5 m from three different LEDs of different wavelengths [64, 116]. The dual-colour integrated μLED device presented

in this chapter allows for the implementation of such multi-colour communications on a single chip. It is fabricated by μTP blue-emitting μLEDs, fabricated as in Section 2.5, onto a pre-fabricated array of InGaN-based green-emitting μLEDs on a sapphire substrate, see Figure 3.2 c).

3.2 Micro-Transfer Printing for Dual-Colour Integration

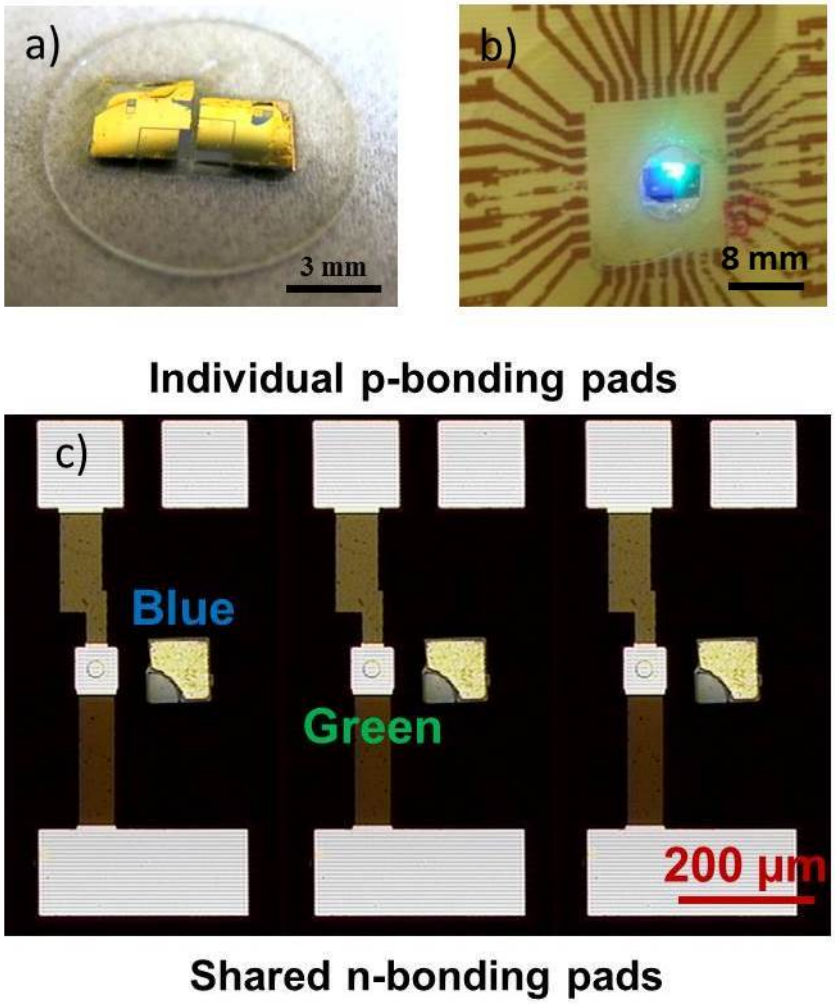

Figure 3.2: a) Two separate (blue and green)LED chips diced and placed as close as possible to each other, b) the separately fabricated μLEDs lit up, and c) the dual-colour integrated chip fabricated by μTP.

Conventionally, in order to have two different colour LEDs next to each other, the

LEDs are first fabricated on separate chips (as seen in Figure 3.2a)). Mechanical dicing tools are then used to dice the chips as close to the LED pixels as possible and then the two LEDs are placed in close proximity. In this technique the separation between the pixels is limited by current dicing techniques to >1 mm and, by eye, these can be seen to be two different light sources rather than one. The μTP technique provides a solution to this - we have nanometre printing precision and therefore little limitation on the separation of pixels (limited only by the size of the supporting anchors ($\approx$15 μm)) and so effective color-mixing is possible. This is illustrated in Figure 3.2 and we can see that the pixels are much closer together when using μTP compared to using more conventional dicing techniques - 15 μm compared to $\approx$1 mm.

3.3 Dual-colour Integrated LED Device: Fabrication

The first steps for the demonstration of this 2 x 8 dual-colour μLED array on a single chip are the separate fabrication of green μLEDs on their sapphire substrate and the integration of ultra-thin blue μLEDs onto the green-emitting μLED chip. The fabrication process and performance of the μLEDs of each colour will be described in this section. It is useful to note here that blue-emitting μLEDs are printed onto an array of green-emitting μLEDs rather than the other way round because high-power GaN-on-Si technology is to our knowledge, to date, all blue emitting.

3.3.1 Fabrication: Green LED Array

A 2 x 4 array of green-emitting flip-chip μLEDs is fabricated from a commercial 520 nm InGaN epistructure grown on a sapphire substrate. The layout of a section of this array can be seen in Figure 3.3. In order to achieve high injection current density and therefore high modulation bandwidth, each disk-shaped green-emitting μLED is designed with a small diameter of 20 μm. The μLEDs are fabricated following the conventional process for InGaN-based μLEDs, as described in [28] and in Section 1.8,

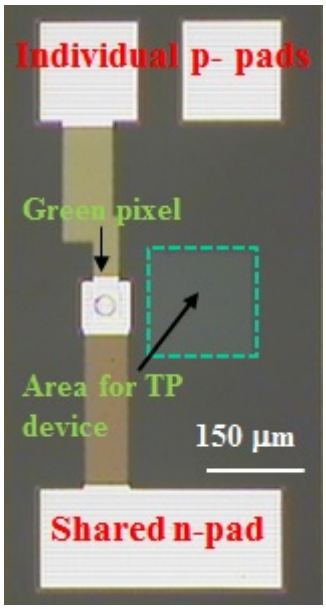

Figure 3.3: Layout of the green-emitting μLED chip before transfer printing.

with an additional deep etch step down to the patterned sapphire substrate (PSS). This additional step is to compensate for height differences between the blue and green μLEDs in further μTP processing.

Following the conventional μLED fabrication process, a 100 nm - thick Pd current spreading layer is deposited on the LED chip (following an HCl acid treatment to prepare the substrate). The pixels are then defined with an etch down to the n-GaN before electrically isolating the pixels from each other with approximately 160 nm of SiO_2. Ti/Au 50 nm/200 nm metal tracks and boding pads are then deposited to electrically address the green-emitting pixels, as seen in Figure 3.3. The areas where the blue-emitting μ LEDs are to be printed, indicated in the dashed blue box in Figure 3.3, are etched down to the PSS. This allows for the height of the blue-emitting μLED ($\approx$ 2.4 μm), levelling out the device post transfer printing.

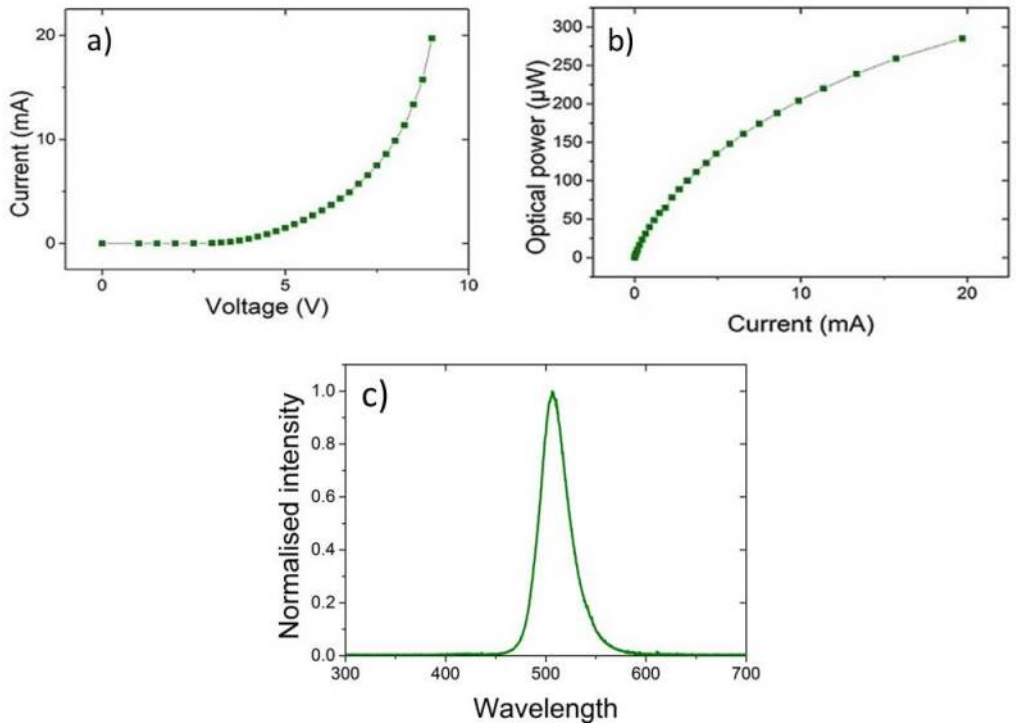

Figure 3.4: IV, LI, and spectral characteristics (spectrum taken at 1 mA) of the green-emitting μLED pixels in the dual-colour device.

Characterisation: Green μLED Array

Figure 3.4 shows the measured electrical and optical performance of this green μLED. The μLED begins to emit light at around 3.5 V, and the LED achieves over 0.27 mW of optical power at 20 mA. The emission wavelength peaks at 510 nm, as seen in Figure 3.4 c). It is important to note that for this power measuerment, and all power measurements in this work, we mean the forward directed power - as measured directly with a power meter (Thorlabs PM100D).

The modulation bandwidth of the green-emitting μLED was measured with the setup as described in Section 1.9.1 (Figure 1.21). The μLED was driven with a combination of AC and DC signals: the DC signal is sent from a conventional DC power supply, and the AC signal from a network analyser. Both signals are combined at a bias-tee and sent to the μLED. The frequency response of the signal detected arriving at an avalanche

photodiode (APD)(Hamamatsu S8664-50K) (see Figure 1.22) is then compared with the original AC signal to give the modulation bandwidth. The ability to drive the μLED to a high current density means an electrical-to-optical (E-O) bandwidth over 400 MHz can be achieved, as is seen in Figure 3.5. These measurements were all taken by directly probing the μLED p- and n-pads.

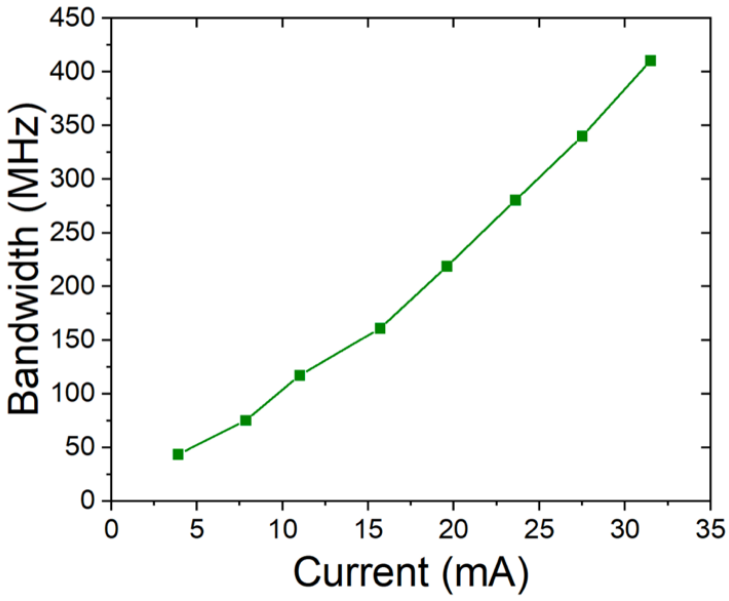

Figure 3.5: Modulation bandwidth characteristics of the green-emitting μLEDs in the dual-colour device.

3.3.2 Fabrication: Blue-Green LED Integration

Once the green-emitting μLED array has been fabricated and characterised, blue-emitting μLEDs are transfer printed into the array onto the PSS areas designated in the green-emitting μLED array fabrication process, as detailed in section 3.3.1. It is not possible to print directly onto the PSS because it is so rough, and so the sample must first be cleaned in an oxygen plasma and coated in a thin layer of the transparent photoresist SU-8 (Gersteltec Engineering Solutions GM1050 SU-8). This fills the holes in the PSS, planarising the the receiver surface and allowing μTP to proceed. This SU-8 layer is neither baked nor exposed to UV light between spin coating and the μTP process, leaving the SU-8 tacky and aiding the release of the μLEDs from the stamp

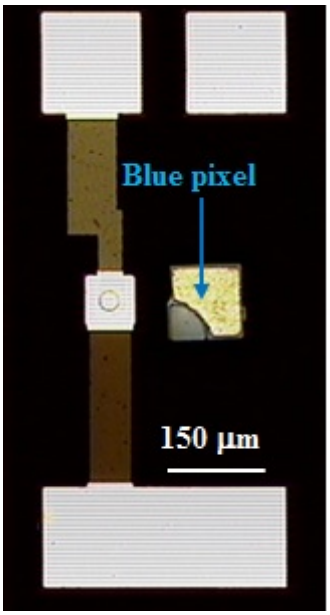

Figure 3.6: Plan view optical micrograph of the layout of the dual-colour μLED chip after transfer printing.

during μTP.

Once the array has been populated with μTP blue-emitting μLEDs, as in Figure 3.6, the blue-emitting μLED must be made electrically addressable. A 6 μm thick layer of SU-8 is spin coated across the chip surface. This acts to insulate the device. Openings in the SU-8 are then patterned to access the p-bond-pads, n-bond-pads and the p- and n-contacts on the μTP μLED.

A 50 nm/200 nm layer of Ti/Au is then deposited on the chip via sputter deposition (see Section 2.6.7). The metal is then patterned and etched to leave tracks connecting the μLED to the p- and n-bond-pads.

Characterisation: Micro-Transfer Printed Blue μLED

After μTP - integration, the blue-emitting μLED pixel is optically and electrically characterised. This μLED achieves an optical power of 0.71 mW at 15 mA, which is comparable to the optical power of the green μLED pixel at the same current ($\approx$

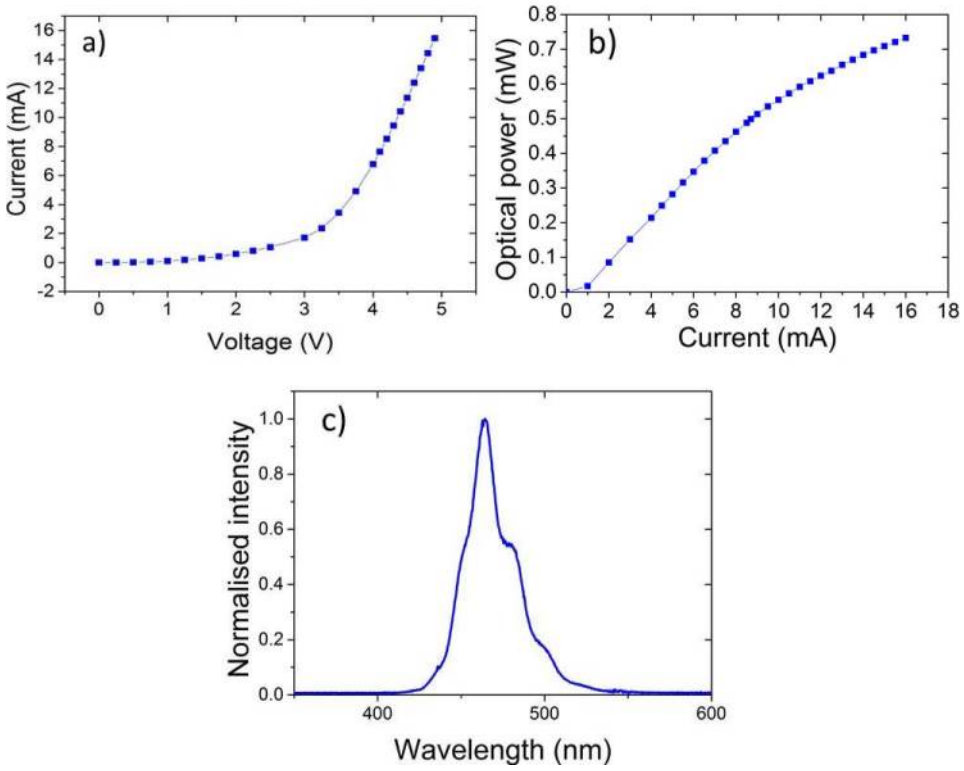

Figure 3.7: a) IV and b) LI characteristics of the blue-emitting μLED on the dual-colour integrated device. The emission spectrum (measured at 1 mA) is also shown c).

0.23 mW at 15 mA). The IV and LI characteristics of these μTP μLED pixels can be found in Figure 3.7. The turn-on voltage of these blue-emitting μLEDs is around 2.9 V, but as seen in Figure 3.7 a), there is a significant leakage current before the turn on voltage. This seems to indicate damage to the LED epistructure, and significantly the MQW active region, during the suspended μLED process, in particular during the KOH underetch described in Section 2.6.4. This increases the occurrences of non-radiative recombination and therefore increases current leakage. Because the KOH underetch is a vital step in the suspended μLED fabrication, the degradation seen in the IV characteristics is unavoidable but can be minimised by engineering the supporting anchors, when designing photolithography masks for the process, such that the time spent in the KOH solution is kept to a minimum.

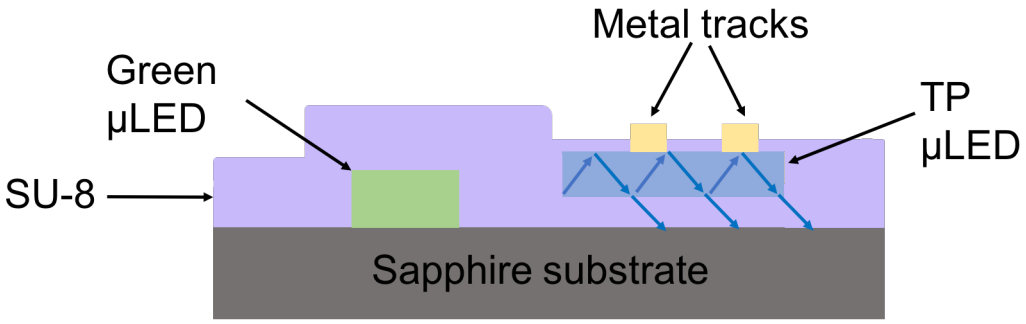

Figure 3.8: Cross-sectional schematic of the dual-colour μLED device. The Fabry-Perot cavity formed when the μLED is printed onto a partially reflective surface is shown, with the light rays shown as blue arrows. The refractive index of GaN is 2.4 and the refractive index of SU-8 is 1.67.

The spectral emission from this blue-emitting μLED is seen in Figure 3.7c) and shows a maximum peak at 460 nm. Fabry-Perot effects are seen when the μLED platelet is printed onto a receiver substrate because of the high refractive index contrast between the GaN LED epilayers and the receiver substrate. This is shown schematically in Figure 3.8. For a Fabry-Perot etalon, the free spectral range is given by:

$$\Delta\lambda = \frac{\lambda_0}{2nl\cos\theta} \tag{3.1}$$

where λ_0 is the wavelength of the central emission, n is the refractive index of the medium within the cavity, and l is the cavity length. If we assume normally incident light, n equal to 2.4 (the refractive index of GaN), and a cavity length of 2.4 μm (the thickness of the μLED), the free spectral range is then equal to 18 nm. This is the approximate separation between the peaks seen in the spectrum in Figure 3.7 c). This effect has previously been reported with similar μTP μLEDs printed on various non-native substrates by Trindade et al. [94].

The modulation bandwidth of the blue-emitting μLED pixels was also measured, in an identical way to the green-emitting pixels on the same device. The blue LED pixel achieves a modulation bandwidth of 146 MHz, as in Figure 3.9. When compared to comparably-sized blue-emitting μLEDs on their growth substrate, these μTP

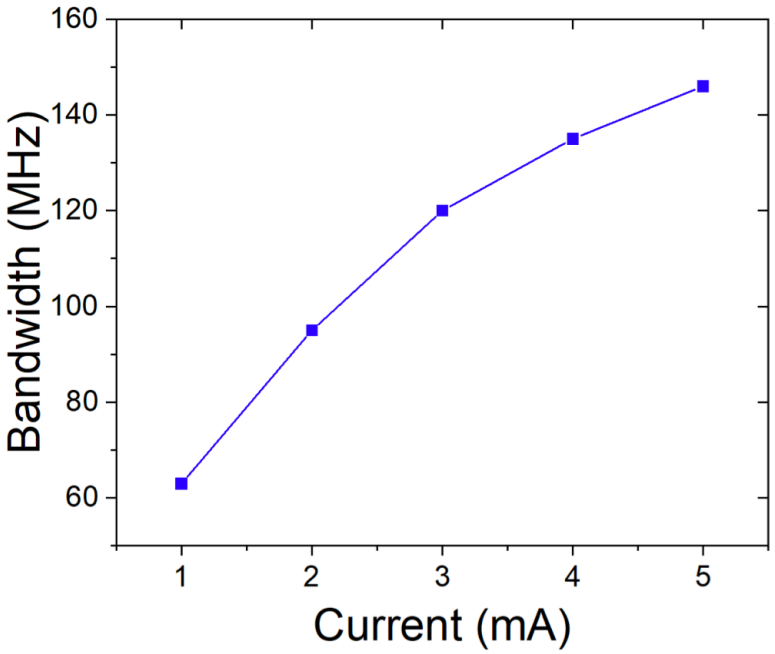

Figure 3.9: Modulation bandwidth characteristics of the blue-emitting μLED in the dual-colour device.

μLEDs have higher bandwidths (similarly-sized blue-emitting GaN-on-sapphire LEDs tend have modulation bandwidths of around a third of this at similar current densities [28, 117]). This we again attribute to the KOH underetch used to suspend these μLEDs, which damages the MQW active region in the μLEDs. This increases the occurrence of non-radiative recombinations which in turn drives up the modulation bandwidth but with detrimental effects on the optical power (see Figure 3.7 b)).

The blue-emitting μTP μLED pixels in this device are also much larger than the green-emitting μLED pixels, i.e. 100 x 100 μm^2 compared to 20 μm diameter, respectively.

3.4 Integrated LED device: Characterisation

After μTP integration, the device can then be addressed and, because of the individual p-pads, each μLED in the pair can be individually controlled and each μLED lit separately or as a pair, as in Figure 3.10. The dual-colour device can then be characterised

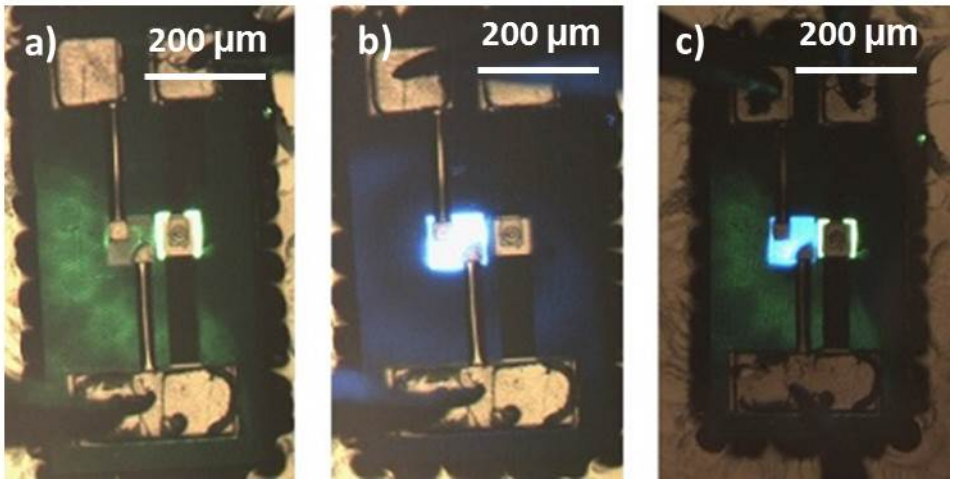

Figure 3.10: Plan view micrographs of the dual-colour integrated μLED device, showing a) the green-emitting μLED turned on, b) the blue-emitting μLED turned on, and c) both μLEDs turned on.

as follows.

3.4.1 Data Transmission

To show the potential of this device for VLC applications, the data transmission rate of the dual-colour device was tested under two different regimes:

- Ganging (when one steam of data is sent using both μLEDs)
- WDM (where a different stream of data is sent with each μLED)

These two regimes were tested in the laboratory at the LiFi R&D Centre at the University of Edinburgh and the experimental setup and results will be discussed below.

Ganging regime

The first demonstration of the capability of the dual-colour μLED device was to show it in ganging mode. This is a regime where a single APD is used to receive the light signal

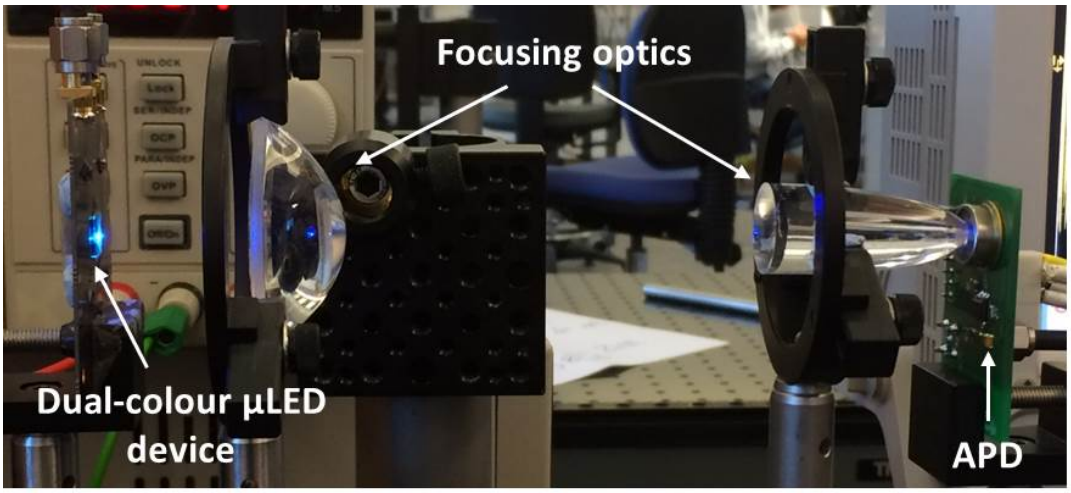

Figure 3.11: Setup used for data rate measurements on the dual-colour μLED device in ganging mode.

and all μLEDs in an array carry the same data. This increases the data transmission rate which can be detected by the reciever, compared to a single μLED because of the increase in optical power, which leads to an increased SNR. We should note that the increase in SNR is not linear, due to the implications of the Shannon theorem (see Equation 1.26 and Figure 1.24).

The setup seen in Figure 3.11 was used to measure the data rates from this device in ganging mode. The dual-colour μLED device is held in one place, and the emission sent over 16 cm to an APD (Hamamatsu S8664-50K) through focussing optics, first a lens to focus the Lambertian emission from the μLED device and then a second lens to collect the light and concentrate it onto the APD. As in all data transmission experiments discussed and presented in this thesis, each μLED is driven with both a DC and modulated AC signal via a bias-tee. The signal is modulated with an orthogonal frequency division multiplexing (OFDM) signal - (refer back to Section 1.9.3 for more details). This setup was first used to measure the data rates of the two μLED pixels in the device separately, and the results can be seen in Figure 3.12 (in the blue and green lines). The blue-emitting μLED achieves a data rate of 260 Mbps below the FEC, and the green-emitting μLED achieves 425 Mbps below this FEC level.

The same setup, as in the photograph in Figure 3.11, was then used to measure the achievable data rate from the combined device in ganging mode. The results of this experiment can be seen in the magenta line in Figure 3.12.

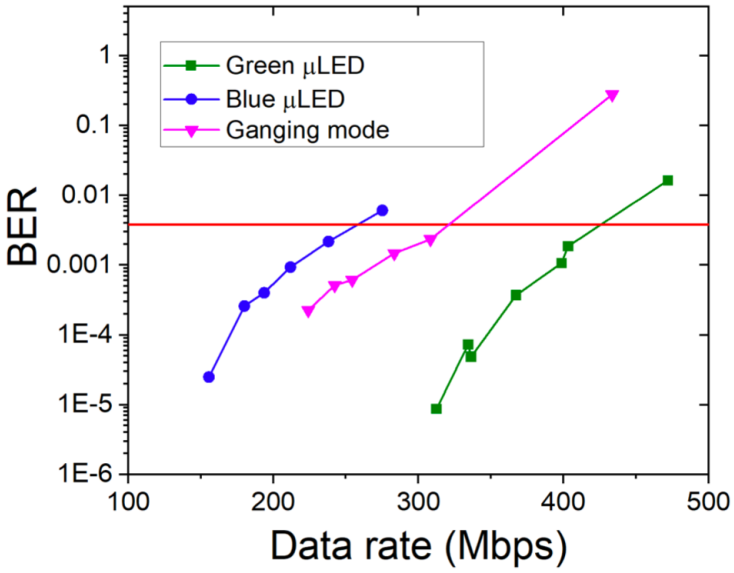

Figure 3.12: The data rate measurements from the respective blue-emitting and green-emitting μLEDs in the dual-colour μLED device, and the data rate of the dual-colour μLED device operating in ganging mode. The FEC level is shown in red.

As seen in Figure 3.12, the combined dual-colour μLED achieves a data rate of 360 Mbps under the FEC level of a BER of 3.8 x 10^{-3}. In this experiment the blue μLED pixel was driven with a DC bias of 6.17 V at a current of 4 mA. The green μLED pixel was driven with a DC bias of 5.65 V at 6 mA. These driving conditions were used as they produced an equal amount of blue and green light spectrally when both μLEDs were simultaneously driven, and thus provide an intermediate spectral emission for the combined device. If we compare the ganging data rate (360 Mbps) to the two separate data rates from the blue and green μLED pixels (260 Mbps and 425 Mbps, respectively) we see that the individual data rates do not sum to give the ganging result. This is due to the interference between the two μLEDs pixels. In particular, the SNR of the blue-emitting pixel does not follow the same trend as the SNR for the green pixel.

WDM regime

As described earlier in this chapter (Section 3.2) one of the main motivations for fabricating this dual-colour μLED device was to send multiple discrete communication streams from one device, through the WDM technique. Having two discrete emission wavelengths on a single chip, see Figures 3.4 c) and 3.7 c), means that it should be possible to send two distinct streams of data from this device. To run the WDM experiment, a similar setup was used to that for the ganging measurements but with the addition of filters to cut the emission of each μLED in turn at the APD to differentiate between the two data streams. A photograph of this setup is shown in Figure 3.13, and we see that using a long pass filter (i.e. one that will allow light to pass through with wavelengths above a cut-off, in this case 500 nm (FEL 500 nm)), only the green component of the light reaches the APD in the centre of the white dashed box while the light emitted from the μLED device can be seen to be blue-green.

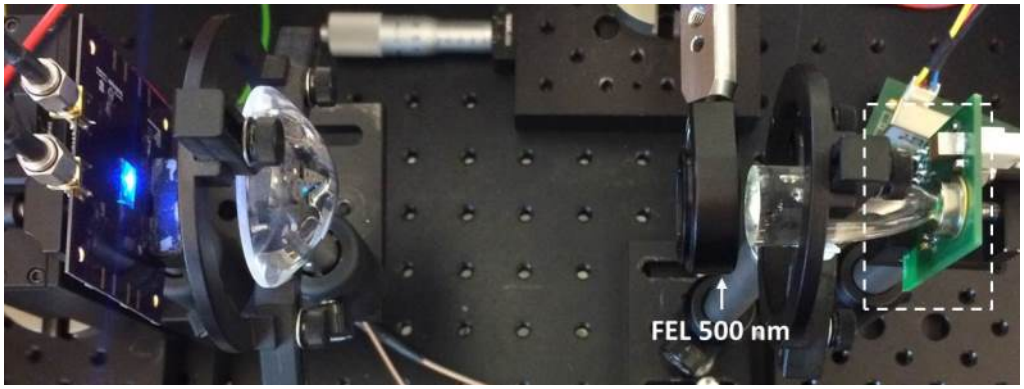

Figure 3.13: The setup used to measure the dual-colour μLED in a WDM experiment. The dual colour device is on the left and the APD receiver on the right.

In this WDM regime, as opposed to the ganging regime from the previous section, each μLED in the blue-green pair was driven with a different modulated signal and a different DC signal using two separate bias-tees. Therefore the combined dual-colour device is transmitting two separate discrete streams of data. The two different streams of data can be separated and are detected at the APD.

In this experiment, two different filters were used: an FEL 500 nm (as seen in Figure

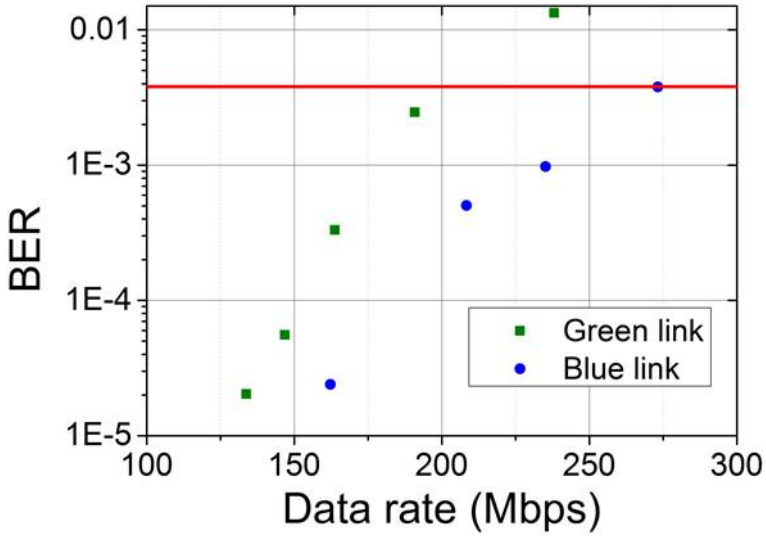

Figure 3.14: The dual-colour μLED device WDM data transmission.

3.13) to pass only the green contribution and an FES 500 nm (short-pass filter, at 500 nm) to pass only the blue contribution. The resulting data streams were measured to find the data rate achievable when the μLED pixels were driven at 4 mA for the blue and 6 mA for the green. The data transmission rate for this situation can be seen in Figure 3.14. We see from this graph that below the FEC level, the green pixel achieves 191 Mbps and the blue pixel achieves 273 Mbps. The overall data rate from the combined dual-colour μLED device is therefore 464 Mbps.

In the WDM regime, the data transmission rate for the green-emitting μLED is significantly lower than for the same device in the ganging regime. The use of the FEL 500 nm filter to cut the contribution at the APD from the blue-emitting μLED also cuts a large amount of the emission from the green-emitting μLED: as we can see in Figure 3.4, a significant portion of the emission is below 500 nm. To counteract this, and allow more of the green emission to reach the APD another long pass filter needs to be used, but a suitable one was not available at the time of measurement.

As the peaks of the green and blue emissions are close together, it is challenging to separate the contribution from each μLED. To maximise the WDM data transmission rate the two μLEDs would ideally have spectral peaks that are further apart. While the

blue-emitting GaN-on-Si is designed to emit at 450nm, the strain effects (as discussed in Section 2.6.5) when the μLED is removed from its growth substrate cause a redshift in the emission to 460 nm. This is a disadvantage here as it brings the emission of the blue μLED closer to that of the green μLED. Using a green LED wafer with a longer peak emission is perhaps the simplest way of alleviating this issue with the overlap of the spectra.

The issue with overlap aside, we can increase the data transmission rate of the combined device by running it in WDM mode. WDM allows us to combine two distinct streams of data and send them simultaneously, increasing the data rate from 360 Mbps when the device is driven in ganging mode (where only a single stream of data can be sent with the device) to 464 Mbps (when 2 separate streams of data can be sent simultaneously).

3.4.2 Colour-mixing

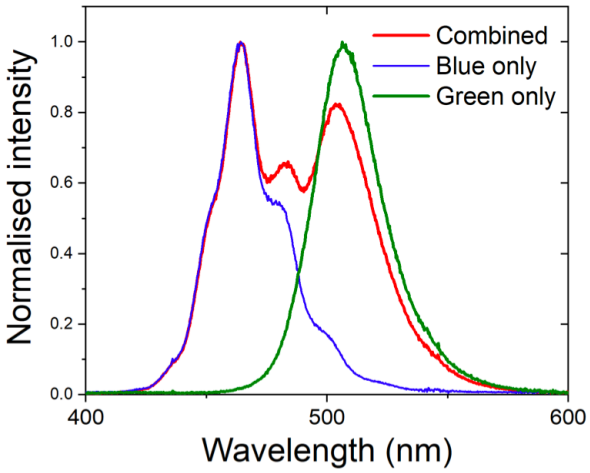

Figure 3.15: Combined spectrum from the blue-green dual-colour μLED device. These spectra were all taken at a drive current of 1 mA (with both μLEDs driven with 1 mA in the combined spectrum) and normalised to produce this figure.

As discussed, one advantage of this integrated dual-colour μLED device is that the μLED pixels are placed very close together (15 μm separation). This means that effective colour-mixing is achieved when both μLEDs are driven together. Figure 3.15 shows the emission spectrum when both pixels in the dual-colour device are driven

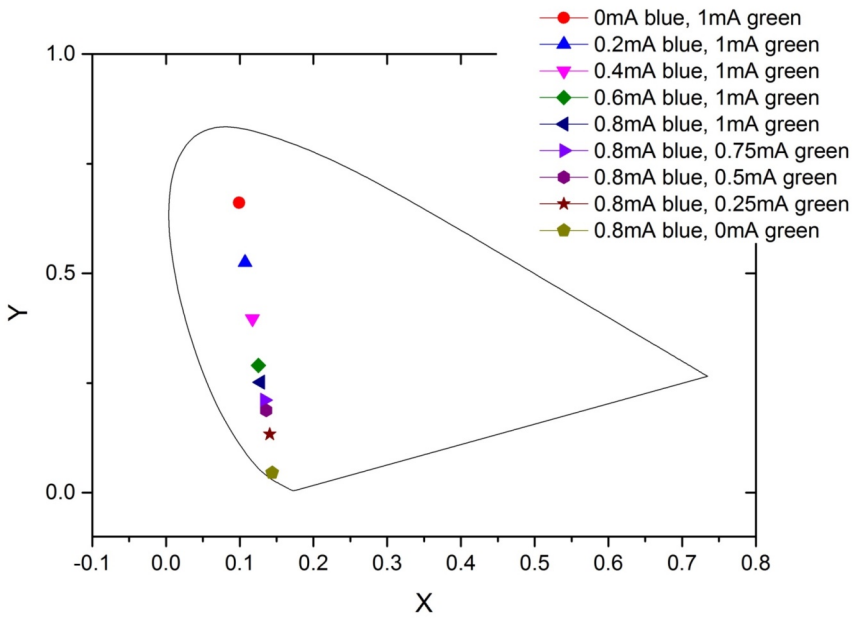

Figure 3.16: CIE characteristics of the dual-colour integrated μLED device.

simultaneously, overlayed with the spectra from the blue- and green-emiiting /muLED pixels. This spectrum was obtained by detecting the emission with a spectrometer (Avasoft 2048L) placed approximately 5 mm from the device at its sapphire side. Here we can see three distinct peaks, one at 460 nm and one at 520 nm which are the main spectral peaks from the green-emitting and blue-emitting μLED in the pair respectively (the individual spectra of which can be seen in Figure 3.4 c) and Figure 3.7 c)), and a third peak around 483 nm which is caused by the overlapping of the shoulder on the blue emission, as discussed previously and seen in Figure 3.7 c) and the tail on the green emission seen into the bluer end of the spectrum in Figure 3.4 c).

The individual control of each separate pixel means that the colour of the device emission can be tuned from 460 nm - 520 nm with the CIE coordinates of the device ranging from (0.09928, 0.6608) to (0.1441, 0.04532). These CIE coordinates can be seen in Figure 3.16 on the CIE colour-gamut (refer to Section 1.9.5 for information on these colour-gamuts). This means that from this one device we can produce a range of colours of light. This becomes even more interesting when we imagine the introduction

of a third, red-emitting μLED which would mean the device could be used to emit a wide range of colours and crucially white light. This will be discussed in Section 6.2.

3.5 Summary

In this chapter the fabrication and characterisation of an integrated dual-colour μLED device has been discussed. This device is fabricated by transfer printing 100 μm x 100 μm blue-emitting LEDs into an array of green-emitting μLEDs. The green μLEDs in this array achieve 0.25 mW at 20 mA, and the blue-emitting μLEDs achieve 0.71 mW at 15 mA. These μLEDs have modulation bandwidths of 400 MHz and 140 MHz respectively.

To show the potential of this dual-colour μLED device for VLC applications it was driven in two different regimes: ganging and WDM. Separately the green-emitting and blue-emitting μLED pixels have data rates of 425 Mbps and 260 Mbps, while in ganging mode the dual-colour device achieves a data rate of 360 Mbps. Sending two separate streams of data with the two different μLED pixels in a WDM experiment gives an overall data rate of 464 Mbps.

Chapter 4

Integrated Colour-converted Device

This chapter will introduce micro-transfer printing of integrated μLED-colour-converter devices. The μLEDs are transfer printed onto a colloidal quantum dot flexible colour-converting platform with an aim of applying the integrated device for VLC applications.

We will first discuss the concept of colour-conversion, and in particular, the used of colloidal quantum dots (CQDs) for colour-conversion including the basic physics behind CQDs. The fabrication of an integrated colour-converting device will then be described, with the device fabricated by μTP an array of μLEDs onto a glass-encapsulated CQD colour-converter. Three different colours of device have been fabricated: red, orange and green. These are used to convert light from blue-emitting μLEDs to output at longer wavelengths.

The characterisation of these devices will then be detailed, with electrical and optical characteristics discussed as well as the data transmission capabilities.

4.1 Colour Conversion for Visible Light Communication

As previously intimated, μLEDs have the potential to be used in fast VLC applications because of their high modulation bandwidths. By modulating the intensity of these μLEDs they can be used to send information. One of the main promises of VLC is that room lighting will not only be used for illumination, but will also be used to transmit data [62]. Conventional solid state white light sources make use of a blue-emitting LED combined with a yellow, down-converting rare earth phosphor to produce white light [118, 119]. However, as well as being based on finite resource materials, these phosphors have long upper state lifetimes (on the order of milliseconds) and cannot be modulated fast enough for optimised VLC. For white LED lighting to be used effectively for VLC applications, alternative fast colour-converters must be found. Colloidal quantum dots (CQDs) have much shorter lifetimes (on the order of nanoseconds, to tens of nanoseconds) and so can be modulated much faster than the slow colour-converting phosphors.

Another way of producing white light is by combining multiple colours of light from different sources; most commonly red, green and blue (RGB) [118]. CQDs can be produced to absorb blue light and emit light across the visible range, and are therefore attractive colour-converters for producing various wavelengths. They also have narrow linewidths giving very "pure" coloured emission. These characteristics make CQD colour-converters attractive for both improved/controlled colour rendering in VLC and also in WDM.

4.2 Colloidal Quantum Dots

CQDs are surface-functionalised and therefore solution processable nano-sized semiconductor crystals, typically with diameter between 2nm and 10nm. This size is comparable to the electron de Broglie wavelength in the semiconductor which leads to quantum

confinement, inducing a quantum size effect and producing discrete energy levels within the CQD [120,121]. As introduced in Chapter 1, the de Broglie wavelength is given by:

$$\lambda = \frac{h}{p} = \frac{h}{\sqrt{2m^* kT}} \tag{4.1}$$

where h and k are the Planck and Boltzmann constants, respectively, m^* is the carrier effective mass, and T is the temperature.

The quantum size effect can be described, as by Efros and Efros in 1982 [122], by the "particle in a box" model where charge is confined in three-dimensions.

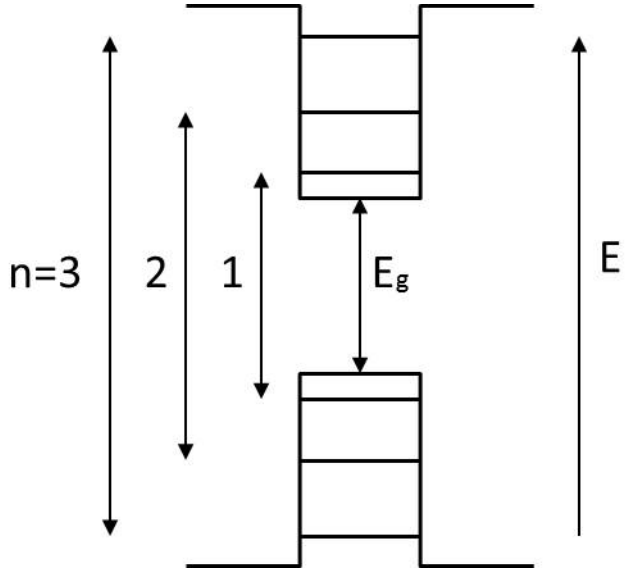

Figure 4.1: Band diagram of a quantum well structure presenting the energies of three optical transitions.

Figure 4.1 shows the transitions between the first few of these quantised energy levels, and their associated energies [123]. This confinement leads to a quantisation of energy levels. As discussed in Section 1.3, transitions can occur between the valence and conduction band in a semiconductor material, causing the emission of light with a wavelength dependant on the energy gap between these two bands. In an quantum dots of radius R, this energy gap is given by:

$$E_{\mathrm{g}}(QDs) = \frac{\hbar^2 n^2 \pi^2}{2 m_{\mathrm{eh}} R^2} + E_{\mathrm{g}}(Bulk); n = 1, 2, 3... \tag{4.2}$$

where

$$m_{\mathrm{eh}} = \frac{{m_{\mathrm{e}}}^* {m_{\mathrm{h}}}^*}{{m_{\mathrm{e}}}^* + {m_{\mathrm{h}}}^*} \tag{4.3}$$

Here ${m_e}^*$ and ${m_h}^*$ are the electron and hole effective masses, respectively. By controlling the size of the dot, the energy gap (and therefore the emission wavelength) can be tuned. As in the above equations, as the size of the dot decreases, the gap between energy levels increases. As we know, the colour of light emitted by a semiconductor material is determined by the separation of the energy levels within this material. The wavelength of emission from quantum dots can therefore be changed by altering the size of the dot, while keeping the same material system. This is illustrated in Figure 4.2.

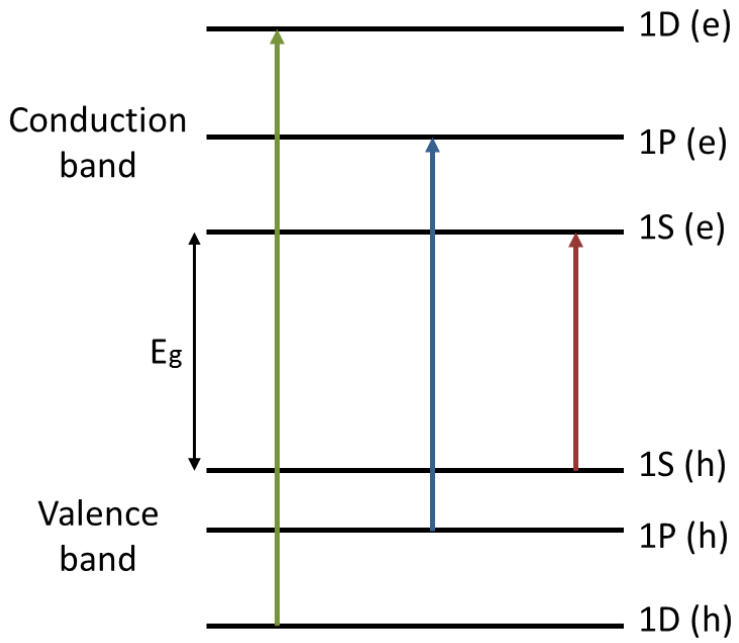

Figure 4.2: Representation of the discrete energy levels in a quantum dot.

The emission wavelength of CQDs can also by tuned by changing the composition of the dot while keeping the size the same. These two methods, size-tuning and changing

the material composition, mean that the emission wavelength of CQDs can be tuned to emit across the visible spectrum, as seen in Figure 4.3.

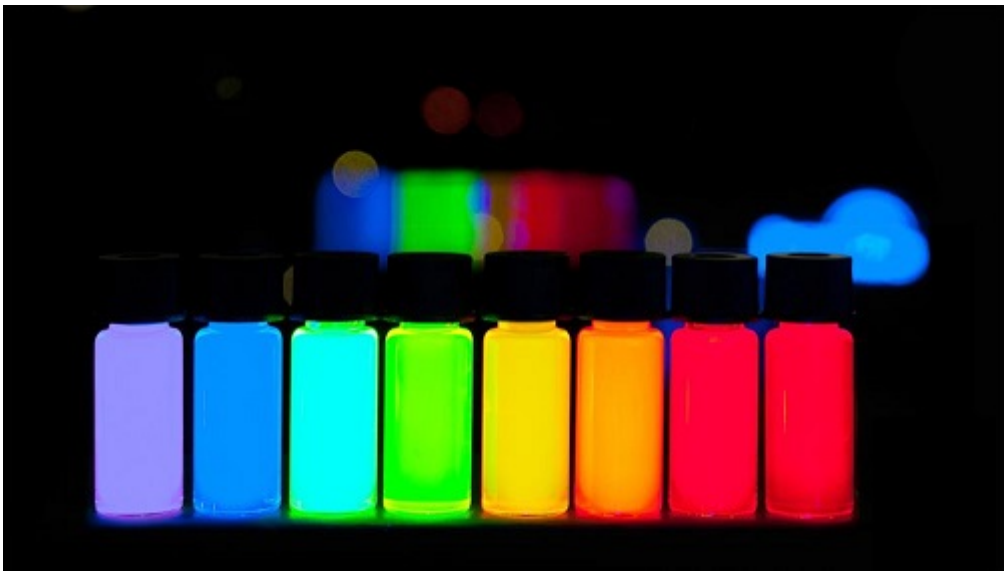

Figure 4.3: CQDs in solution emitting across the visible spectrum when illuminated with UV light. The Image from [124].

As seen in Figure 4.4, CQD materials cover a wide range of wavelengths from UV to mid-IR, and can be fabricated from a variety of semiconductor materials. The CdSSe (II-VI) materials, which are used in this work, can be tuned to emit approximately between 300 nm and 800nm.

The quantum dots used in this work are of the CdSSe/ZnS alloyed core/shell design. The emission wavelength is varied through the composition of the CdSSe core, and they are passivated and confined by a ZnSe shell. The passivation by an outer shell reduces surface carrier trapping, increasing the photoluminescence quantum yield [126, 127]. Organic ligands attached to the outer surface of the shell aid dispersion in solvents, which is required for this work [128].

CQDs are synthesised in solution by wet-chemistry processes involving the decomposition of metal-organics and calcogenides in organic solvents at high temperatures [120, 128]. The CQDs are usually provided by the vendor in solution, as in Figure 4.3, and are therefore compatible with solution processing and soft lithography techniques.

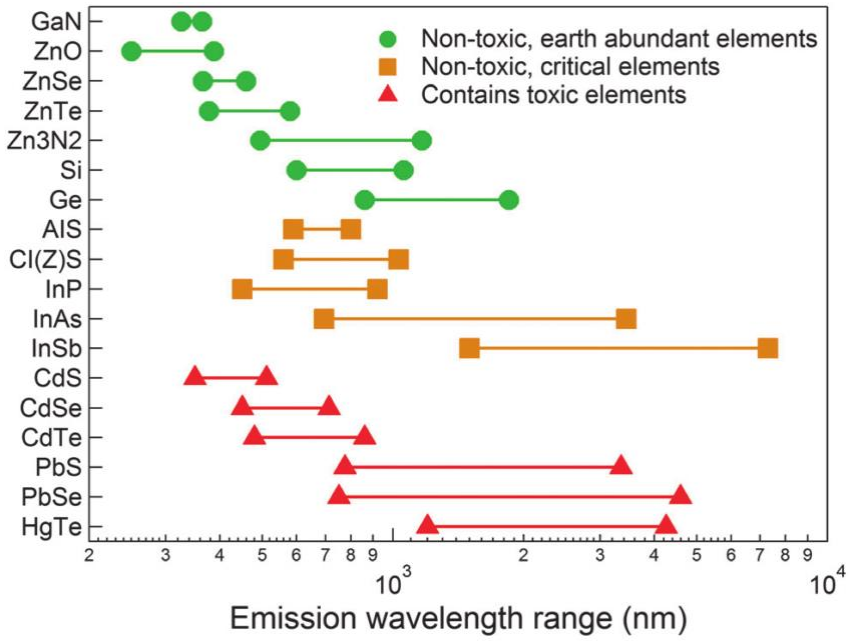

Figure 4.4: Wavelength coverage of various kinds of CQDs. Images from [125].

When the solvents are evaporated, the CQDs become free-standing "neat" CQD films.

Figure 4.5 shows a typical absorption/emission spectrum for CQDs of 4 different sizes, emitting in the blue, green, yellow and red. For any of these emission wavelengths we see strong absorption in the blue to UV region, making them ideal for excitation with InGaN μLED sources.

4.2.1 Colloidal Quantum Dots as Colour-converters

The CQDs utilised in the devices in this work are, as already mentioned, of the CdSSe/ZnS alloyed core/shell design, (Cytodiagnostics). The emission wavelength is varied through the composition of the CdSSe core. The mean size of these CQDs is 6 nm in diameter at all wavelengths used. Previous results from our group with similar CQDs (CdSe/ZnS) have been reported by Foucher et al. who demonstrated CQDs encapsulated in thin glass as wavelength tunable lasers [130] and Guilhabert et al. as a gain medium in DFB lasers for refractive index sensing applications [131]. When

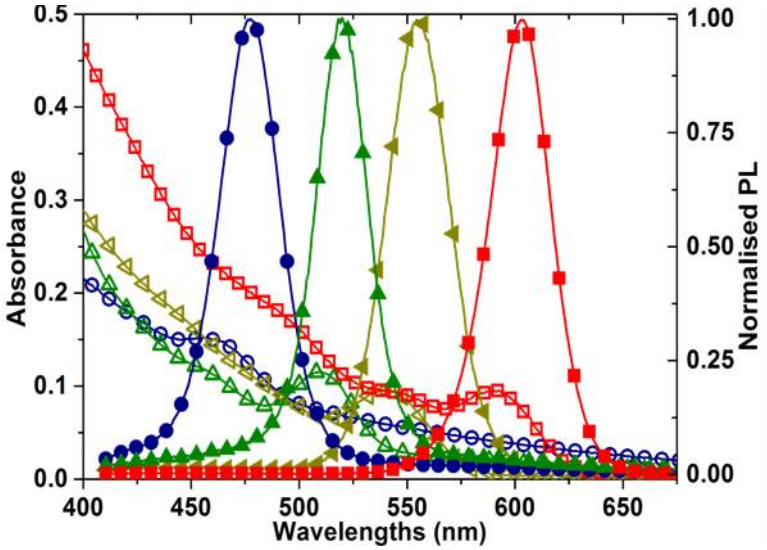

Figure 4.5: Typical absorbance and emission spectra of four different II-VI CQDs, emitting in the blue (481 nm), green (526 nm), yellow (561 nm), and red (591 nm). Adapted from [129].

incorporated into a PMMA matrix, these CQDs have been reported to achieve free-space optical data transmission rates of up to 500 Mbps when pumped with an external blue-emitting (λ = 450 nm) μLED [132].

4.3 Fabrication: Colour-converter-LED Integrated Device

4.3.1 Micro-transfer Printing LEDs on Flexible Glass

A 100 x 100 μm^2 μLED, fabricated as in Section 2.5, is transfer printed onto a single (1.5cm x 1.5cm) piece of 30 μm-thick mechanically flexible glass (AF32 thin glass from Schott). The μLED is printed directly onto the flexible glass without the aid of an adhesive interlayer, via Van der Waals' forces aided by capillary bonding. Capillary bonding occurs when a liquid is placed between two surfaces and, as the liquid evaporates, the surfaces are drawn together and eventually held together by a strong Van der Waals bond [133]. This is used in many fabrication processes, for example to attach

small samples to Si carrier wafers for processing structures on thin or fragile substrates. It has also been used for bonding thin II-VI laser structures to diamond, as reported by Jones et al. [134], and to integrate thin II-VI colour-converters with LEDs for VLC applications, as reported by Santos et al. [135].

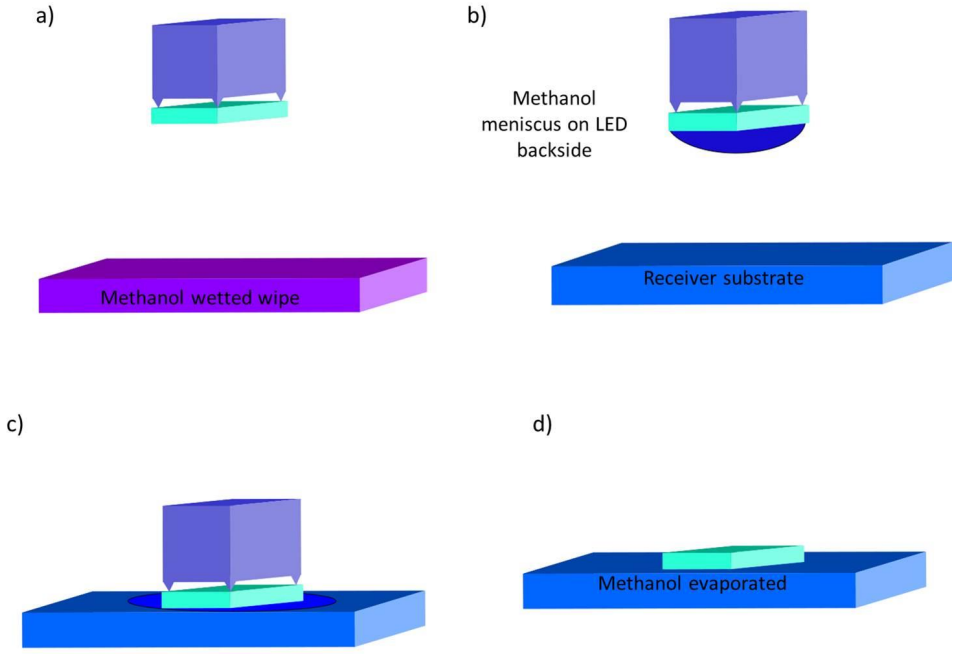

Figure 4.6: The capillary bonding process: a) μLED brought into contact with methanol-wetted wipe, b) backside wetting of μLED, c) μTP aided by capillary forces, and d) methanol evaporation.

During the μTP process, the capillary bonding is facilitated, as in Figure 4.6, by wetting the backside of the μTP μLED with methanol. The μLED backside is wetted by pressing it into contact with a methanol-soaked wipe, which has been pre-soaked by pipetting a few drops of methanol onto it. The methanol-soaked wipe is labelled in the right-hand photograph in Figure 2.7.

When the wetted μLED is brought into contact with the thin glass receiver substrate the surface tension of the methanol on the μLED backside is suddenly broken, pulling the μLED down towards the receiver surface. This is sufficient to force the μLED to detach from the stamp and, with a quick stamp withdrawl, it remains on the receiver

substrate. The sample is then heated slowly to completely evaporate the methanol from the sample and the μLED is left held to the flexible glass by the Van der Waals' force.

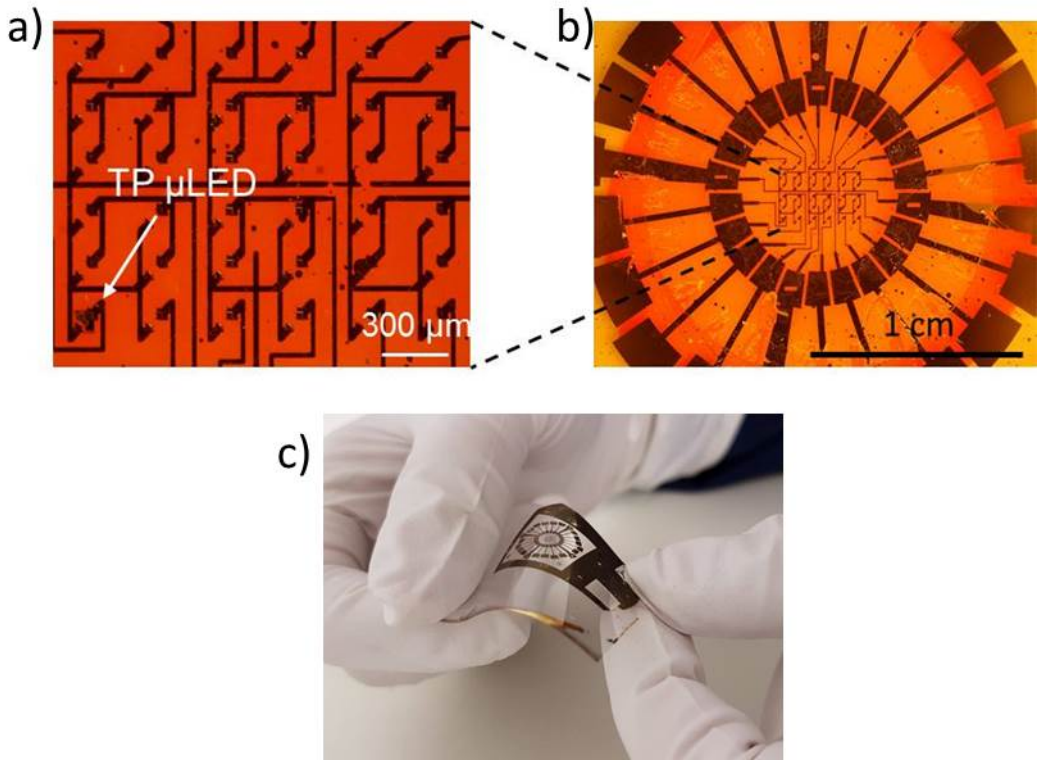

Figure 4.7: A μTP μLED array and metal tracks on 30 μm-thick thin glass. From a) to c) in decreasing magnification, c) shows the mechanical bendability of the integrated devices.

The typical μTP post processing, as described in section 3.3.2, with SU-8 insulation and metal track deposition, is then done to complete a fully addressable μLED array on the thin glass sheet. The μLED array on the thin glass, with metal tracks is seen in Figure 4.7. These μTP μLEDs are flip-chip, meaning the light emitted is directed down through the n-GaN and AlN buffer layers rather than up through the p-GaN layer. Light in these μLED on thin glass samples is therefore directed down through the glass (see Figure 4.11). To our knowledge, this is the first reported demonstration of transfer printing on this thin flexible glass.

4.3.2 Characterisation of micro-LEDs transfer printed onto flexible glass

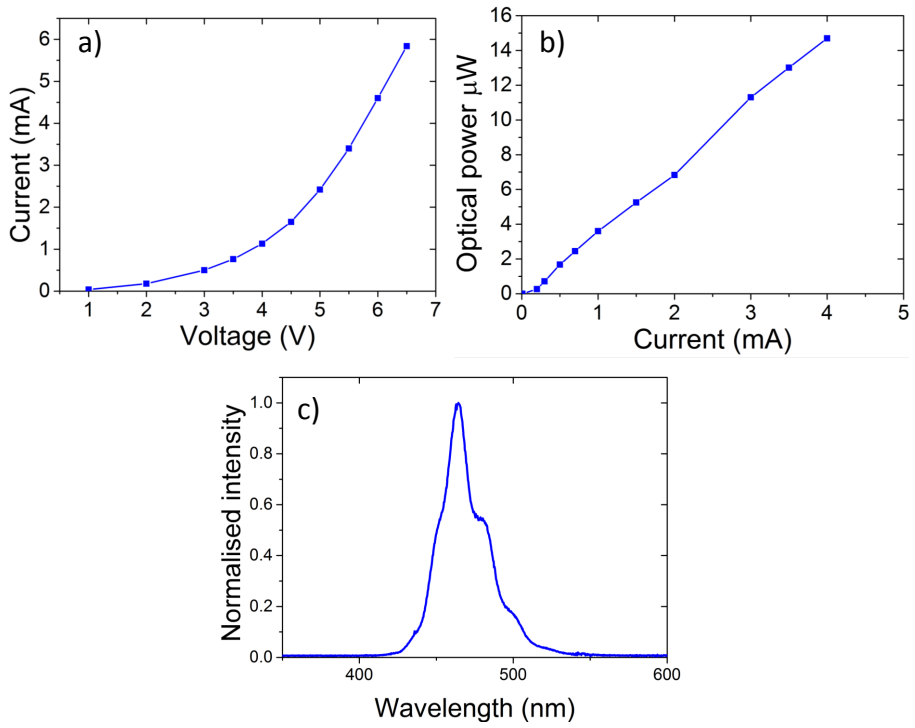

Figure 4.8: Characterisation of μLEDs when transfer printed onto flexible glass. a) I-V, b) L-I, and c) spectral characteristics are shown. The spectrum was measured with a drive current of 5 mA. The devices are of area 100 $\times$ 100 μm^2.

When micro-transfer printed onto flexible glass, these μLEDs achieve an optical power of over 15 μW at 4 mA, as seen in Figure 4.8 b). It is important to note here that the μLEDs used to obtain this result and the results discussed in Section 4.4.2 are not from the same fabrication batch as those used for all the other measurements presented in this thesis in Chapter 3 and Chapter 5. They were fabricated with different supporting anchors, which are tapered to aid pick-up during transfer printing rather than rectangular as are used in all the other μLEDs transfer printed in this PhD work. When fabricating these μLEDs with tapered anchors, all fabrication processes were identical to those described in Chapter 2 except that a much longer KOH underetch was required to suspend these μLEDs - approximately 110 minutes compared to approximately 48 minutes for those with rectangular anchors.

Figure 4.8 a) shows the IV characteristics of the μTP μLED on flexible glass. If we compare this IV to the related characteristic shown in Figure 3.7 a), where the μLEDs are printed on sapphire, we see that the turn on voltage is higher (tending to be close to 3.5 V rather than 2.9 V when printed on sapphire). This can be attributed to two main things. Firstly the different fabrication process, and secondly the thin glass receiver substrate. The thermal conductivity of this glass is low, and so the μLEDs heat up much faster, limiting the achievable optical power, as well as the current to which the μLEDs can be safely driven to before thermal roll-over or μLED damage. Again, we see a significant leakage current before the turn on voltage in Figure 4.8 a) which we attribute to the damage occurring during the KOH underetch.

As shown in Figure 4.8 c) these μLEDs emit at 460 nm but we see Fabry Perot effects which arise when the μLED is printed.

4.3.3 Integrated Colour-converter Fabrication

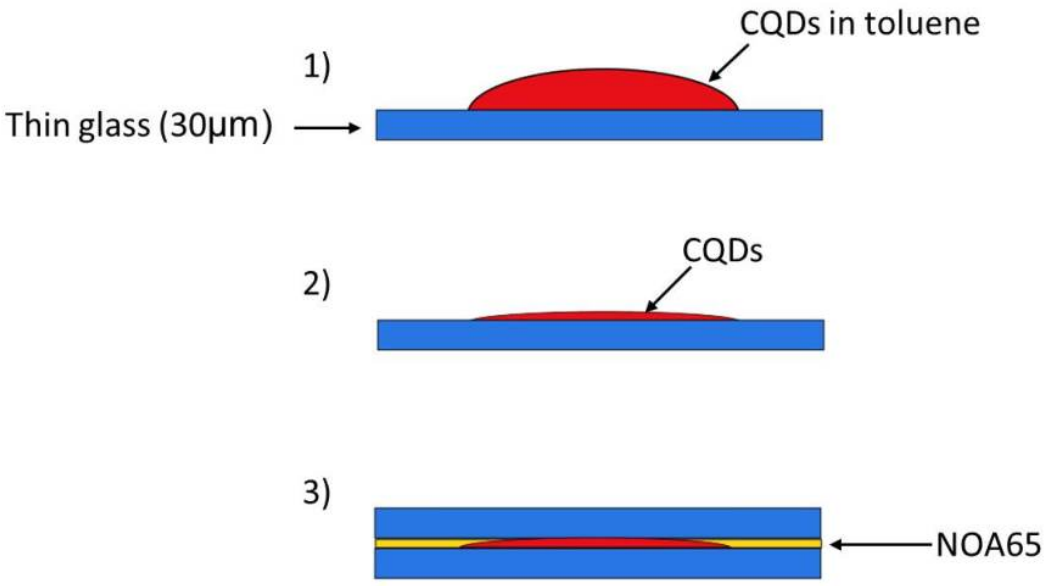

Figure 4.9: Integrated μLED-colour-converter device fabrication process. 1. The CQDs in solution with toluene are dropped onto a piece of thin glass, 2. the toluene is then evaporated, and 3. this is encapsulated by the piece of glass populated with μLEDs (as in Figure 4.7).

Three different colours of CQDs were used in this work: red(λ = 630 nm), orange(λ = 590 nm) and green(λ = 550 nm). Figure 4.9 shows the fabrication process for integrating the CQD colour-converters with the μTP μLEDs on thin glass:

1) A solution of CQDs in toluene at 40 mg/ml for the green sample and 30 mg/ml for the red and orange sample, was drop coated onto a second 30 μm-thick glass sheet, with an area of 1.5 $\times$ 1.5 cm^2 to match the area of the glass populated with μLEDs.

2) This was allowed to dry slowly at 5°C, inside a fridge, to evaporate the toluene and form a uniform "neat" layer of CQDs.

3) The thin glass sheet with the μTP μLED array on it was used to cover and encapsulate the CQDs and the "sandwich" was sealed with a UV curable epoxy NOA65(Norland Inc.), see Figure 4.9. The assembly of these colour-converters is done in ambient conditions. This fabrication gives a $<$ 70 μm-thick integrated μLED-colour-converter device.

Figure 4.10 shows the three completed devices, illuminated with UV light.

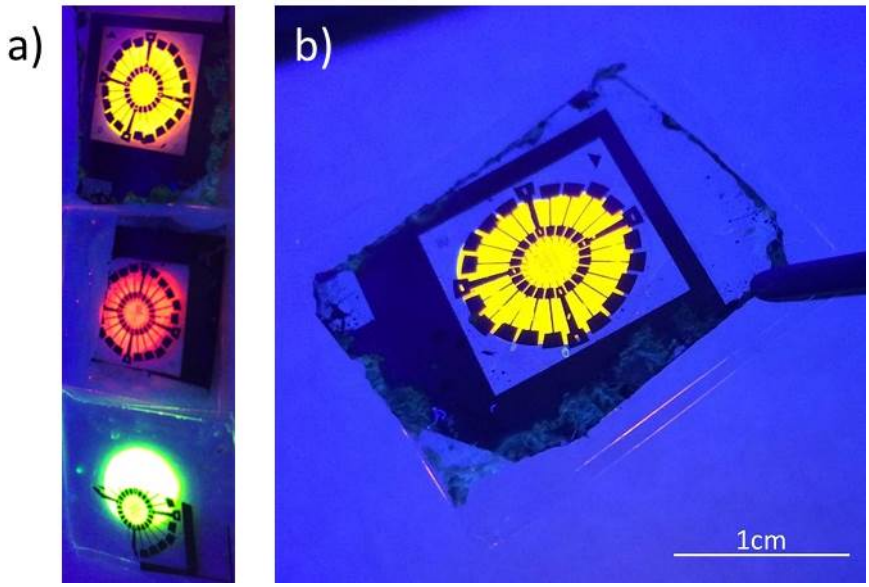

Figure 4.10: Integrated μLED-colour-converter device on thin glass. a) All three different coloured CQD samples, and b) the orange sample at higher magnification, when illuminated with UV light.

When the μLEDs are electrically driven, the blue light is absorbed by the CQDs and

emitted at a longer wavelength as seen in Figure 4.11 a) and b).

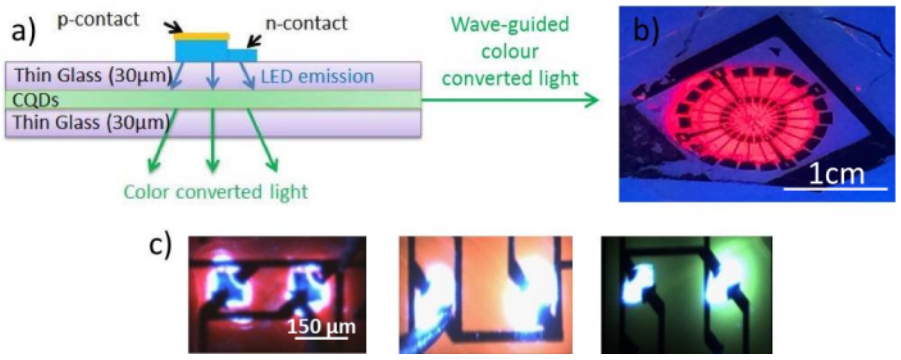

Figure 4.11: a) A schematic of the integrated device, b) the red sample illuminated with UV light, and c) a section of the μLED array lit on each of the different CQD samples.

4.4 Characterisation

4.4.1 Spectral Characterisation

Figure 4.12 shows the spectra from the three integrated μLED-CQD-colour-converter devices. The major emission peaks seen are at 640 nm, 590 nm and 550 nm for the red, orange, and green sample, respectively. The smaller peak around 460 nm, seen most clearly for the red colour-converter because of its relatively low optical power, is the spectral contribution from the unconverted blue light from the μLED.

4.4.2 Efficiency of the Integrated Colour-converter Devices

A reference sample, fabricated as in section 4.3, was made only excluding the CQDs. The IV and LI characteristics of the μTP μLEDs on the thin glass platform itself were then tested to give a base measurement, with the μTP μLEDs achieving an optical power of 26 μW at a maximum drivable current of 6 mA. Figure 4.13 shows the LI characteristics of three μLEDs transfer printed on the same thin glass sample. As we can see, below 1.5 mA the μLEDs behave in the same way. However, beyond this point

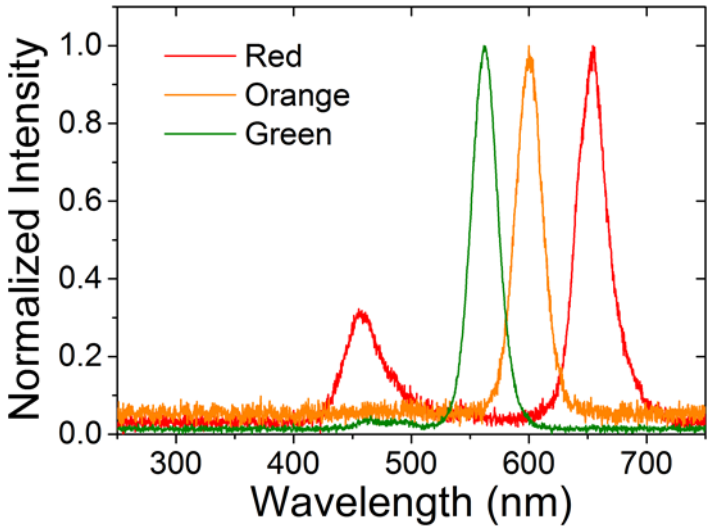

Figure 4.12: The spectra from the three integrated μLED-colour-converter samples. Each spectrum was taken with a μLED drive current of 5 mA.

the behaviour of the μLED cannot be predicted, with some rolling-over around 4 mA but others rolling-over or burning out at much smaller currents. We speculate that this is due to differences in the contact area between the μLED and the thin glass during the μTP of each μLED. Pressing the μLEDs down harder tends to increase the contact area between the devices and the receiver substrate, and this contact area contribute to the device's temperature during operation (as heat must be transferred from the device into the underlying substrate to stop it becoming damaged). This in turn has an effect on the current density we can drive the μLEDs to and the point of thermal rollover.

As touched upon previously in this chapter (Section 4.3.2) these μTP μLEDs cannot be driven to high current densities because of the removal of the Si substrate during the suspended μLED fabrication, as outlined in section 2.5, leaving them incapable of effectively managing heat. Given that small μLEDs can reach temperatures of 150°C [136] under a DC bias, irreparably degrading the electrical and optical characteristics of the μLED, the μTP μLEDs must be protected from being driven to high current densities which would heat them extremely rapidly to similarly high temperatures causing breakdown and μLED failure. This rapid overheating can be prevented by μTP the μLEDs onto thermally efficient substrates like diamond, as demonstrated by Trindade

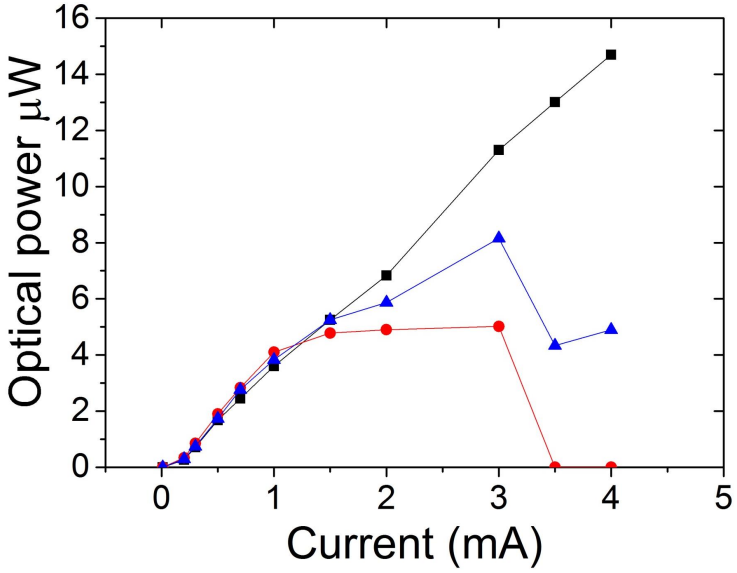

Figure 4.13: LI characteristics of 3 separate μTP μLEDs on a thin glass reference sample. These were fabricated identically on the same chip, and so are nominally the same.

et al. [95], which has a high thermal conductivity of 1000 $Wm^{-1}K$ and can effectively remove heat from the μLED. However, the thin glass used in the devices reported here has a much lower thermal conductivity (1.16 $Wm^{-1}K$ [137]) and a safe maximum driving current of 6 mA (corresponding to a current density of 77.5 Acm^{-2}) is used to control heat in the μLED and prevent degradation whilst in operation.

Because of the difference in LI characteristics of these μLEDs on the flexible glass, the following absorption and efficiency calculations are performed using data from a drive current of below 1.5 mA, where we can be sure the data collected will be comparable between different μLEDs.

The three different integrated μLED-colour-converter samples were then tested for the same IV and LI characteristics, see Figure 4.14, and compared to the reference sample. We again see the LI curve for the three colour-converter samples rolling over, which is likely attributable to the thermal roll-over of the μLEDs. The percentage absorption of the blue light by the respective CQDs is given by:

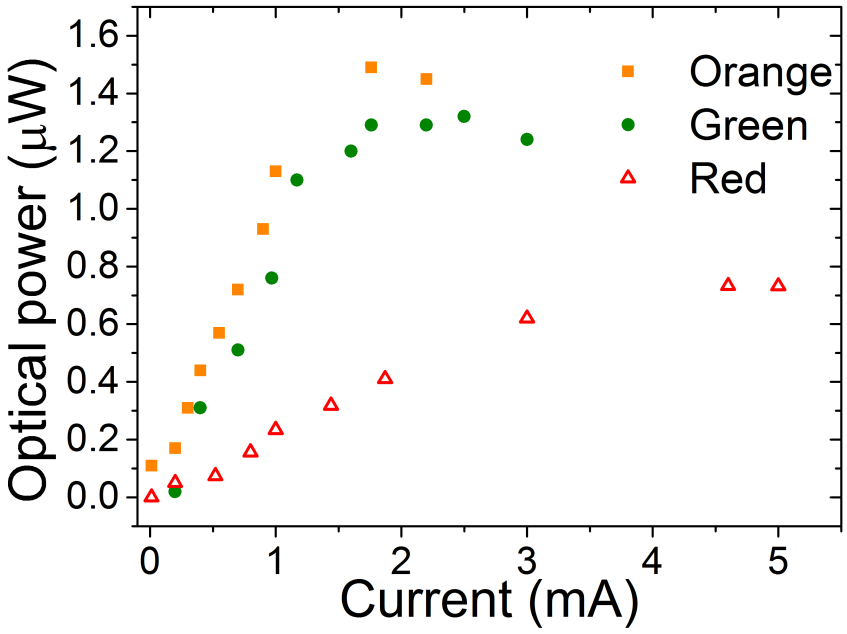

Figure 4.14: LI characteristics for the red, orange and green μLED-colour-converter samples, where the optical power is that of the respective colour-converted wavelengths and the current is that drawn by the μLED used for photoexcitation.

$$Absorption = 100 \times \frac{P_{\text{Blue}} - P_{\text{UC}}}{P_{\text{Blue}}} \tag{4.4}$$

where P_{Blue} and P_{UC} are the optical powers of the blue μTP μLED on the reference thin glass sample, and the unconverted blue light passing through the colour-converter sample respectively. The absorption was calculated as >95% for each of the three colour-converter samples (95 %, 98 % and 97 % for the red, orange, and green sample respectively).

Forward power conversion efficiency (i.e. light converted from blue, as emitted by the μLED, to light at a longer wavelength by passing through the CQD layer) is an indication of how efficient the colour-converting samples are at converting absorbed blue light into forward-directed emitted colour-converted light and is given by:

$$Efficiency = 100 \times \frac{P_{\text{CC}}}{P_{\text{Blue}} - P_{\text{UC}}} \tag{4.5}$$

where P_{CC} is the optical power of the colour-converted (red, green or orange) light. This was measured as 8.8% for the red, 15.0% for the orange and 14.6% for the green sample, respectively. The efficiency for each device were found by taking the optical power (P_{CC} and P_{UC}) at several μLED drive currents, and comparing them to the optical power (P_{Blue}) of the reference sample at the same μLED drive current. The quoted efficiencies are the average of those calculated.

The efficiency values are higher than what could be expected if only considering light within the escape cone of the flexible glass/CQD film structure (2 to 5% taking the geometry of the structure and PLQY between 20% and 60%). These higher values are attributed to photon recycling with some of the waveguided light being scattered out of the structure and some being reabsorbed by the CQDs and partially re-emitted in the forward direction. We note that it should be possible to increase the forward conversion efficiency by incorporating light extraction features in the film and/or the ultra-thin glass to increase the scattering, and/or by adding a dichroic coating on the backside of the structure to reflect converted light in the forward direction while letting the LED excitation light through to the CQDs.

4.5 Side-emission from the integrated LED/colour-converter device

As well as converting light, from blue to a longer wavelength, in the forward direction (i.e. down through both thin glass layers and the CQDs) the integrated device also traps some light in the CQD layer and it is waveguided through this layer and emitted at the side of the sample. When fabricating samples for the results discussed in this section, the CQDs were dropcoated so that they completely cover the bottom piece of flexible glass in the structure, and the light can therefore be guided in the CQD layer and emitted at the edge of the sample, as in Figure 4.11 a).

The emission from this wave-guided light was measured at the edge of the glass struc-

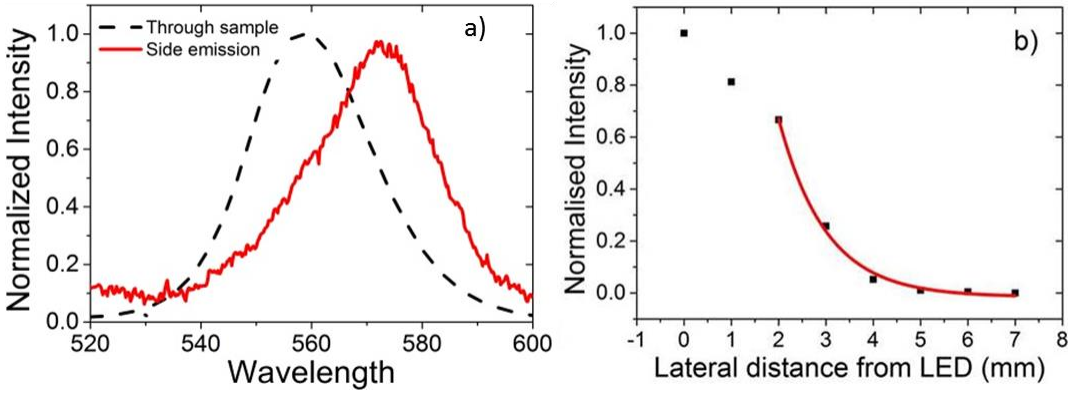

Figure 4.15: Emission from the edge of the green colour-converter sample. In a) we compare the spectrum of the edge emission to that obtained colinearly. In b) we take the light emission directly under the μLED and compare it to that at various lateral distances from the μLED (see Figure 4.16).

ture. The far-field spectrum corresponding to the light guided in the CQD film after 20 mm of propagation was also measured. There is a red-shift of this spectrum, due to self-absorption, when compared to the forward emission (as illustrated in Figure 4.15 a)) of 3 nm for the red sample, 5 nm for the orange sample and 10 nm for the green sample. It is also verified that the magnitude of the shift is affected by the propagation distance, Figure 4.15 b).

The losses in this waveguided light are measured by collecting the emission through the colour-converter structure, in the forward direction, as a function of the lateral distance from the μLED. This is shown schamatically in Figure 4.16. These losses are due to self-reabsorption and consequently they are wavelength dependent. Figure 4.15 b) shows the forward intensity at 555 nm versus the lateral distance from the μLED for the green sample. When the distance from the μLED is large enough so that forward light and leaky modes are not significantly coupled into the detector, the intensity decays exponentially. The loss can be extracted from this exponential decay. The guiding loss for each colour-converter waveguide is 1.50 cm^{-1}, 0.97 cm^{-1} and 1.05 cm^{-1} for the red (639 nm), orange (594 nm), and green (555 nm) respectively.

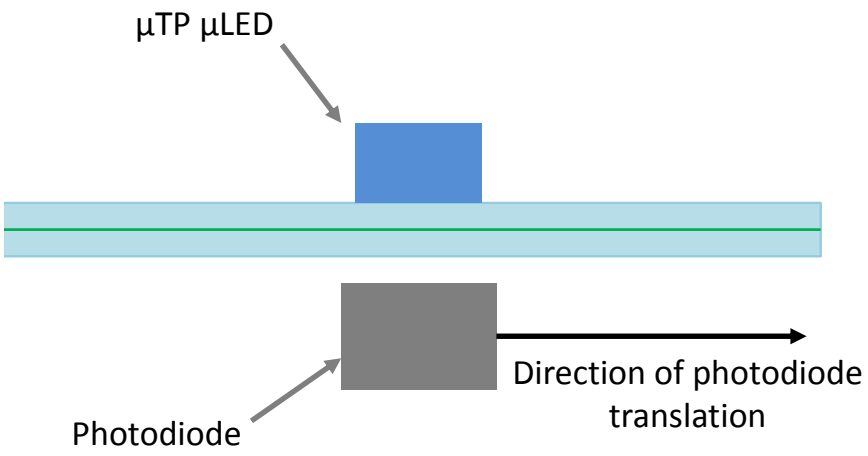

Figure 4.16: A schematic of the process for measuring the losses (as seen in Figure 4.15b)) in the waveguided light in the integrated μLED-colour-converter samples.

4.5.1 Data Transmission Measurements

Modulation Bandwidth

To show the potential of these integrated μLED-colour-converter samples for VLC applications the modulation bandwidth was measured. This measurement was done at the University of Glasgow with the same setup as described in Section 3.3.1 and shown in the schematic of Figure 1.21 a). A bias-tee was used to send both a DC and a modulated AC signal to the μLED with the frequency response measured to find the modulation bandwidth. Figure 4.17 shows the modulation bandwidths of the green and orange integrated μLED-colour-converter devices with respect to drive current. Both samples reach a modulation bandwidth of around 10 MHz (9.7 MHz for the green and 9.9 MHz for the orange). These values are similar to those expected from the carrier lifetime of these CQDs as in [138].

These measurements were taken with a Femto Si APD (HSA-X-S-1G4-SI) which will

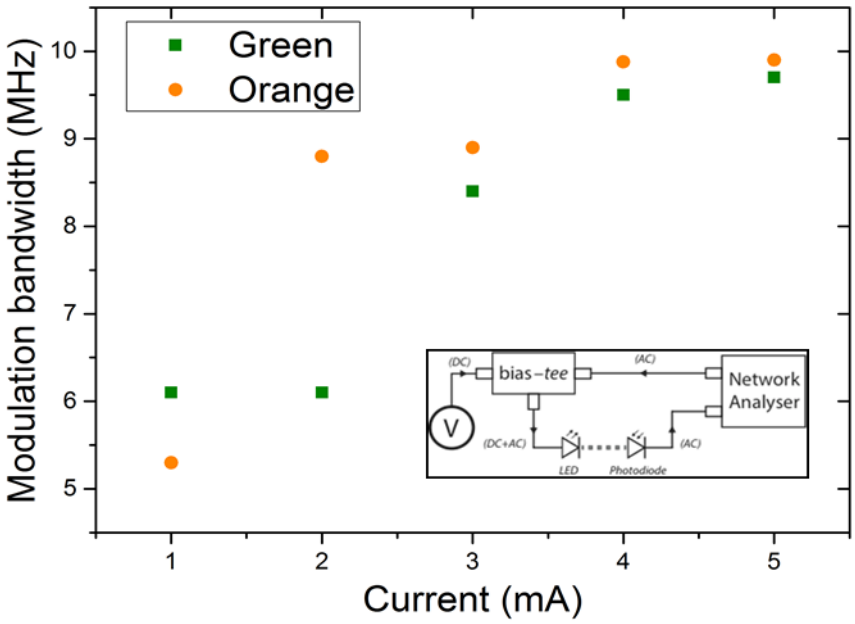

Figure 4.17: Modulation bandwidth results for CQD intgrated μLED-colour-converter devices. The setup used to measure this can be seen in the inset.

measure bandwidths from 10 kHz up to 1.4 GHz [139]. Because of the smaller forward power conversion efficiency, combined with the already low μLED power compared to similarly sized μLEDs fabricated on sapphire, the red sample's power is too low to be detected by this APD. An attempt was made using a more sensitive APD (Sensl-MicroFJ-SMA-30035) but the intrinsic bandwidth of the photodiode is only 4.1 MHz [140], which is lower than the expected modulation bandwidth expected from the integrated μLED-colour-converter devices.

When illuminated with an external μLED from close proximity, these red CQD colour-converters, fabricated identically but without μTP steps, have a modulation bandwidth of 16 MHz. [141]. It is assumed that the red integrated μLED-colour-converter device will have a similar modulation bandwidth.

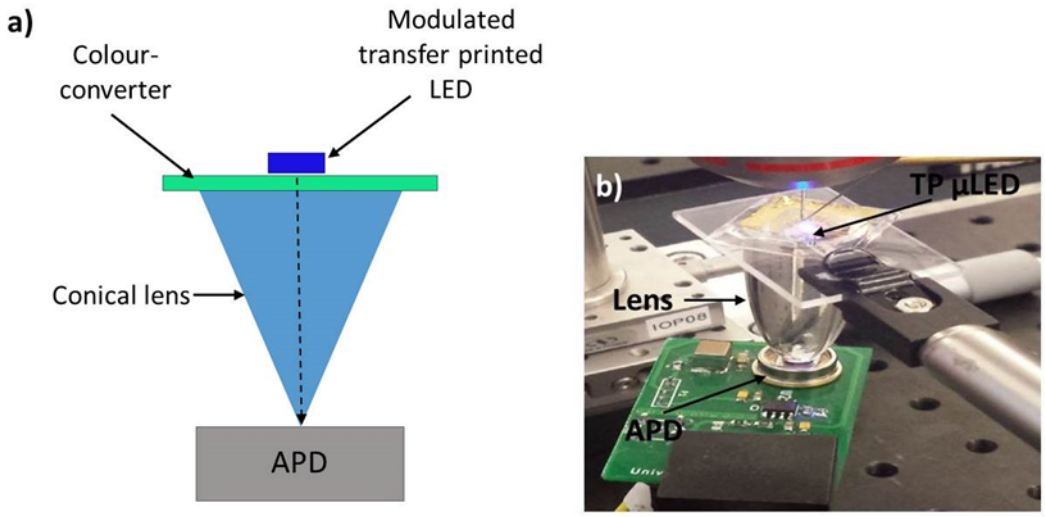

Figure 4.18: Setup used for OFDM measurements on μLED-colour-converter samples. Shown a) schematically and b) in a photograph.

Data Rate

To further demonstrate the VLC capabilities of these integrated μLED-colour-converter devices, the data transmission rates were measured. These were measured in the lab of collaborators at the University of Edinburgh, similarly to those measurements outlined in section 3.4.1.

OFDM measurements were acquired with the setup seen in Figure 4.18. Both a DC signal (drive current, 3 mA) and a modulated AC signal (through a bias-tee) were sent to the μTP μLED to modulate the light emitted by the integrated device. An incoming stream of bits was modulated using multi-level quadrature (M-QAM) before a Hermitian symmetry and inverse fast Fourier transformation (IFFT) operation was applied on N_{FFT} M-QAM symbols. Here $N_{FFT} = 1024$. The resulting OFDM stream was transmitted to the μLED through an arbitrary waveform generator (AWG), Agilent 81180A. The modulated light is then emitted by the integrated LED-colour-converter.

The sample was placed directly onto the top of a conical lens (a compound parabolic condenser (CPC)), and the modulated light collected at the bottom of the lens with

an avalanche photodiode (APD) (Hamamatsu S8664-50K). The detected signal is then sent to an oscilloscope (MS07104B) and demodulated offline.

Because of the comparatively low power of these devices, the working distance is shorter than the other OFDM measurements presented in this thesis (in Chapter 3 and 5), and the measurements are back-to-back i.e. where the emitting device is coupled to the APD through a lens, and travels through no free-space.

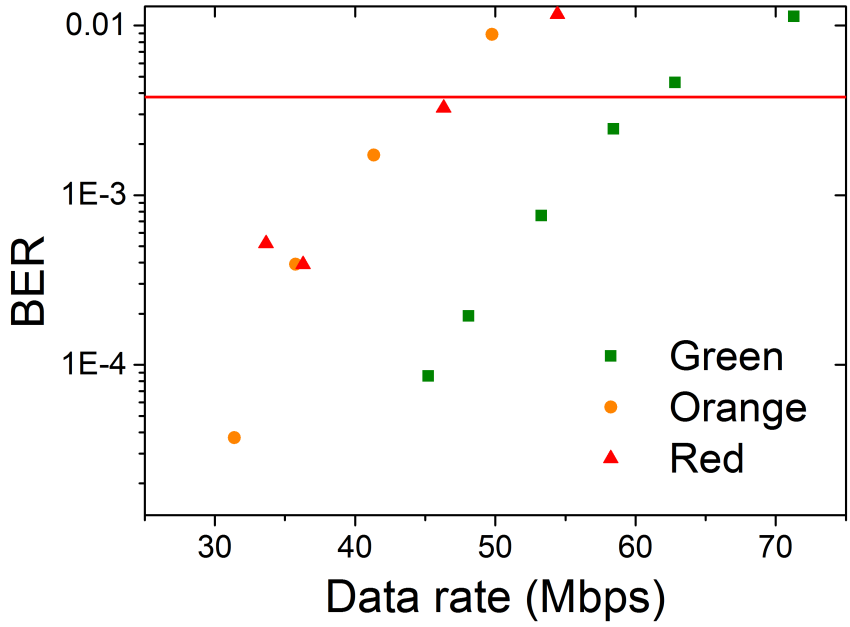

Figure 4.19: Data transmission rate measurements for the integrated μLED-colour-converter devices, at three different wavelengths. The FEC level is seen in red.

The OFDM data transmission rates measured for each integrated μLED-colour-converter sample with respect to BER are shown in Figure 4.19 and were measured to be 46 Mbps, 46 Mbps and 61 Mbps for the red, orange and green sample respectively.

As seen in Figure 4.19, the data rates are realistically limited to a BER of $3.8\text{x}10^{-3}$ and so although the figure shows data rates higher than those previously stated for these samples they would not necessarily be achievable in real-world applications (for more information, refer back to the details on FEC at the end of Section 1.9.3).

4.6 Summary

In this work, a novel colour-converting structure is demonstrated, which has potential for visible light communications and possibly photonic chip applications. The colour-converting structure has been fabricated by integrating, through a μTP process, an ultra-thin blue-emitting InGaN μLED with a thin glass platform functionally enhanced with CQD colour-converters.

Three different colours of CQDs have been used in this work to fabricate three different integrated μLED-colour-converter devices: red (λ = 630 nm), orange(λ = 590 nm) and green (λ = 550nm). Once fully contacted, these hybrid μLED-colour-converter devices achieve absorptions of over 95% of the μLED light and have forward power conversion efficiencies of 9% for the red CQD sample, 12% for the orange CQD sample, and 16% for the green CQD sample. The potential for these integrated μLED-colour-converter devices for visible light communications applications has been discussed and demonstrated, with data rates of 46 Mbps, 44 Mbps and 61 Mbps being achieved for the red, orange and green samples respectively.

Chapter 5

Integrated Optical Transceiver

This chapter deals with the fabrication of an optical transceiver. The μTP technique is used to integrate blue-emitting μLEDs with a fluorescent optical concentrator to fabricate a device that can both transmit modulated blue light (from the μTP μLED) and receive incident modulated light (from an external μLED).

The concept of an optical transceiver is first introduced, before the different elements used during the fabrication are described. The characterisation of the optical transceiver device will also be discussed.

Finally, the idea of using this optical transceiver device as an optical relay is introduced, where the modulated signal from the μTP μLED is detected at an APD and that signal is fed into the external μLED and repeated.

5.1 Optical Concentrators

In order to fully utilise the available bandwidth from μLEDs, it is vital that the signal to noise ratio (SNR) at the receiver is as large as possible. The easiest way of increasing the SNR is to increase the amount of signal arriving at the receiver. However, large

area photodiodes are expensive and slow (which limits the bandwidth) [142] (the APD used throughout this work has an active area of 5 mm diameter) and therefore we must find an alternative way to increase the SNR. We can increase the SNR in the receiver by concentrating light onto the receiver using an optical element - conventionally a lens or compound parabolic condenser (CPC).

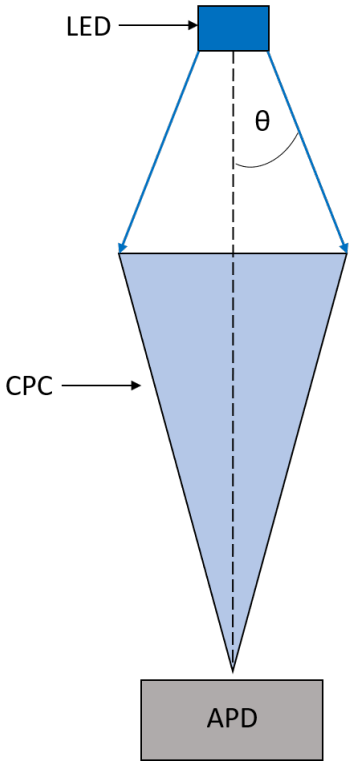

Figure 5.1: Schematic of light from an LED being concentrated by a CPC onto an APD.

Figure 5.1 shows a schematic of such a situation. For such optical elements with refractive index n (i.e. the refractive index of the CPC in the case of Figure 5.1), the maximum optical gain (the input area, A_{in}, compared to the output area, A_{out}), is limited by étendue:

$$Gain = \frac{n^2}{sin^2\theta} \tag{5.1}$$

where θ is the semi-angle defining the field of view. Therefore increasing the optical

gain in a system will reduce the field of view [143]. This is not practical in VLC applications over any real distance. A way to circumvent these limits, and increase the field of view while still increasing the gain is to use a new kind of condensing optical element - an optical concentrator (also sometimes called an optical antenna). This is because they make use of a fluorescent material, which is accompanied by a Stoke's shift and colour-conversion, and do not rely exclusively on reflection or refraction.

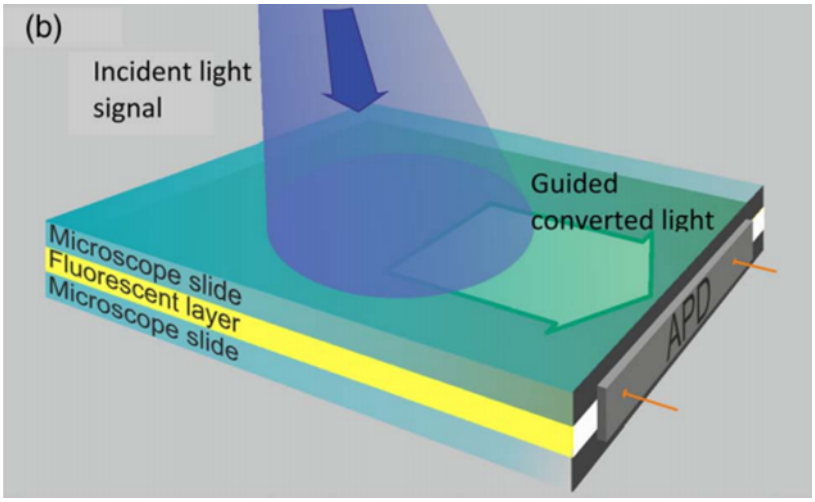

Figure 5.2: Schematic of an optical concentrator. Light from an external source is collected by the concentrator and converted by the fluorescent layer. It is then guided to the end of the concentrator and concentrated (focussed) onto the APD, placed close to the end facet. Image from [143]

These concentrators use a thin layer of fluorescent material sandwiched between two pieces of glass cladding, see Figure 5.2, absorbing incident light and re-emitting at a longer wavelength. The fluorescent material is chosen to have strong absorption at the wavelength of the incident light (in the case of VLC applications, and in this work, peaking typically around 450 nm to match the emission of InGaN-based blue-emitting μLEDs) but weak reabsorption at its own emission wavelength. It must also have a refractive index higher than the surrounding glass cladding such that the light is partly trapped by total internal reflection and only escape at the end facets of the antenna. A uniform, thin layer of this fluorescent material is important to be able to guide and concentrate the incident light, from a field of view too wide for a small detector, to a small area suitable for a small detector, thus increasing the signal-to-noise ratio. For

VLC applications it is also important that a fluorescent material is chosen with a short upper state lifetime (ideally less than 10 ns) so that it can be modulated fast enough for fast data transmission. Recent results of work with these optical concentrators can be found in [143, 144].

5.2 Fabricating an Optical Transceiver

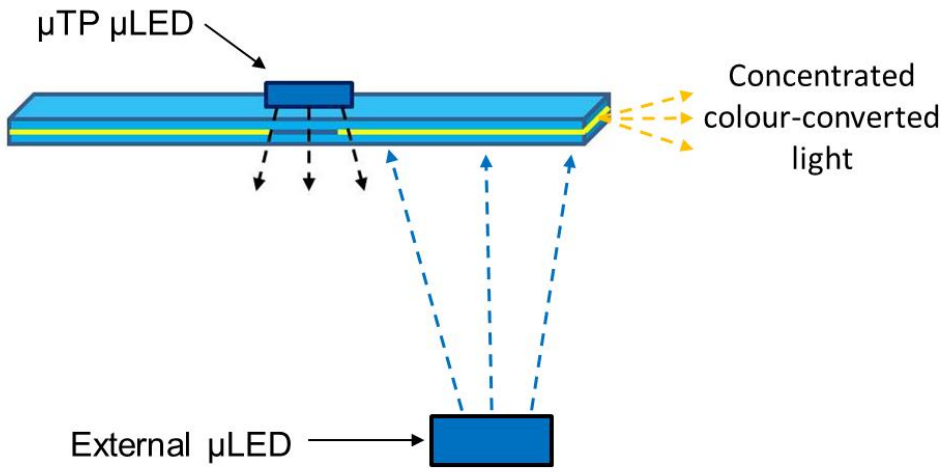

Figure 5.3: Concept for an optical transceiver. Light is emitted by the μTP μLED, and light is collected from an external μLED and colour-converted and concentrated onto the end facet of the structure.

The optical concentrator, as fabricated by collaborators at the University of St Andrews in [143], will be used to receive light from an external source (a blue-emitting μLED) and guide it to the edge facet where it can be detected by an APD.

Transfer printed μLEDs are printed on the top of one of these optical concentrators, and used to emit light i.e. they are the transmitter part of the integrated device.

Figure 5.3 shows the optical transceiver concept discussed below. The transfer printed μLED can be seen on the top of the transceiver structure, which can be modulated to transmit data. Modulated light from an external μLED is incident on the receiver part

of the transceiver (the optical concentrator) and is guided along in the fluorescent layer to the edge facet of the concentrator.

5.2.1 Transfer Printing LEDs on Microscope Slide

To fabricate the integrated optical transceiver, a single 100 × 100 μm^2 μLED was printed onto the top surface of a thick glass microscope slide. This was done using μTP aided by capillary bonding, identically to the process described in Figure 4.6. The same SU-8 insulation and metal deposition as in the previous two chapters was done following μTP to deposit metal tracks to address the μLED, see Figure 5.4.

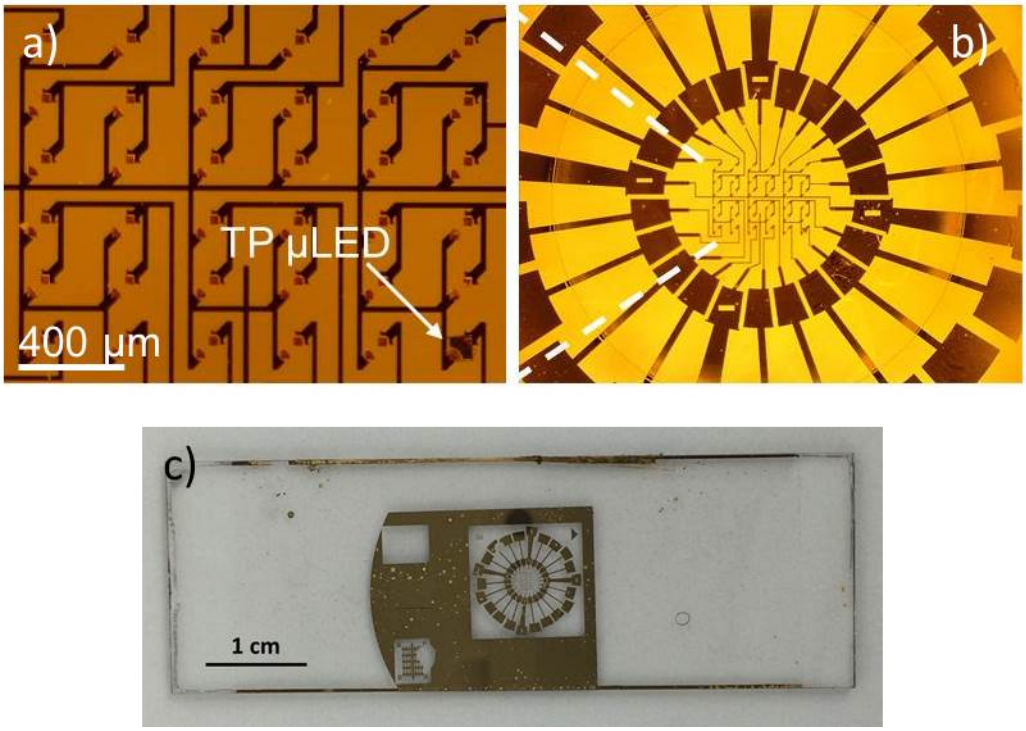

Figure 5.4: a), b) and c) show decreasing magnification of images of the μTP μLED printed onto a microscope slide.

Characterisation of μLEDs on Microscope Slide

After μTP on the microscope slide, the electrical and optical characteristics of the μLEDs were measured. These can be seen in Figure 5.5. The μLEDs have a main spectral peak around 460 nm. In Figure 5.5 c) we again see the Fabry-Perot effects occurring when the μLED is printed onto the microscope slide.

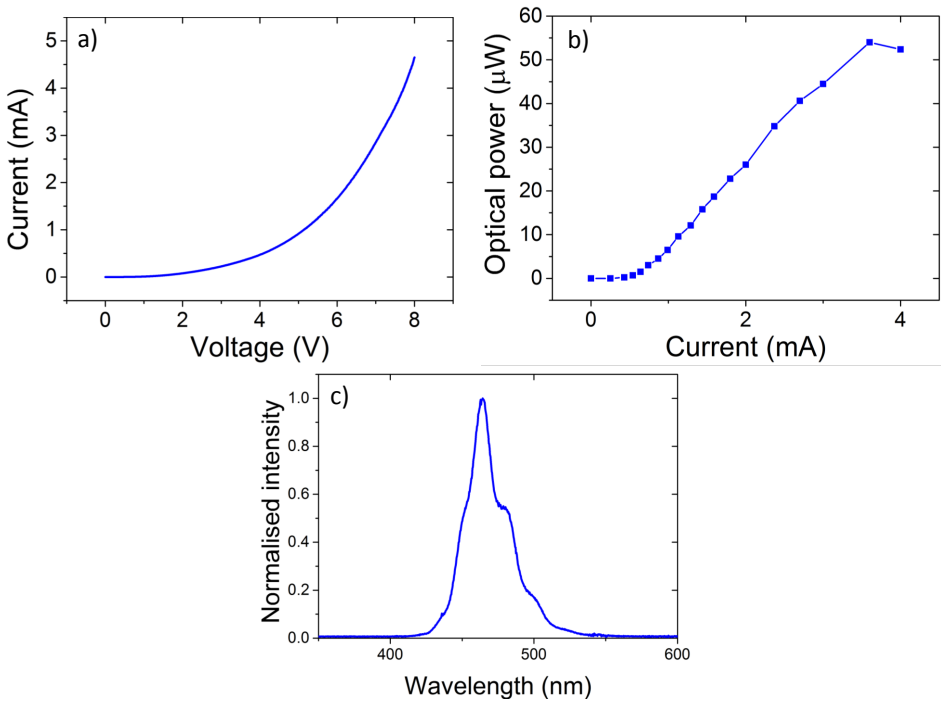

Figure 5.5: The a) IV, b) LI and c) spectral characteristics of a μLED transfer printed onto a microscope slide. The spectrum was taken with a μLED drive current around 4 mA.

These μLEDs are from the same fabrication batch as those used in Chapter 3 and so we can therefore compare the LI graphs from both. As seen in Figure 5.5b) these μLEDs achieve an optical power of 54 μW at 3.6 mA when printed on the thick glass microscope slide. This is approximately 3 times less than the optical power at a comparable drive current of the μLEDs on the device in Chapter 3 (these achieve 152 μW at 3 mA, see Figure 3.7 b)). Printed on glass, these μLEDs can also be seen to roll-over before 4 mA - again much lower than on the integrated μLED device in Chapter 3. The differences

in LI characteristics between these two devices can be attributed to the difference in thermal coefficient between glass (1.4 W/mK) and sapphire (23 W/mK), as discussed in Chapter 4. The inferior heat-sinking capability of glass means that μLEDs printed on it will heat up quicker, meaning they cannot be driven to such high current densities before the μLED becomes damaged. These μTP μLEDs on thick microscope slides have an optical power of $\approx$ 25 μW at 2 mA, see Figure 5.5b). At the same current, similar devices micro-transfer printed onto thin glass (as in Chapter 4, Figure 4.8) have a lower current density of $\approx$ 5 μW. This majority of this difference can be attributed to the different thermal coefficients of these two glasses. We must note here that, as previously discussed, the μLEDs used in Chapter 4 were fabricated slightly differently to those used in this chapter and so a direct comparison is difficult to make.

5.2.2 Transceiver Fabrication

The receiver part of the optical transceiver was fabricated by Dr Pavlos Manousiadis, at St Andrews University. A thin film of the fluorescent material commonly known as "super yellow" was blade coated onto a microscope slide. "Super yellow" (SY) is a conjugated polymer, aquired commercially from Merck KGaA (PDY 132). SY has a short radiative lifetime ($\approx$1 ns) which means it can be modulated quickly. It also has a high fluorescence quantum yield and is highly absorbant at 450nm, which matches the emission band of blue-emitting InGaN-based μLEDs and thus makes it an appropriate colour-converting material for some VLC applications [145]. Figure 5.6 shows the absorption and emission spectra for SY.

Initially, a 4 mg/ml solution of the fluorescent material was prepared by dissolving SY in chlorobenzene. An automatic film applicator (Zehntner GmbH ZAA 2300) was then used to blade coat the solution onto the microscope slide. During blade coating, the temperature was set to 40°C, the speed of the blade to 30 mm/s and the height of the blade to be 100 μm above the microscope slide. This produced a homogeneous film about 70 nm thick.

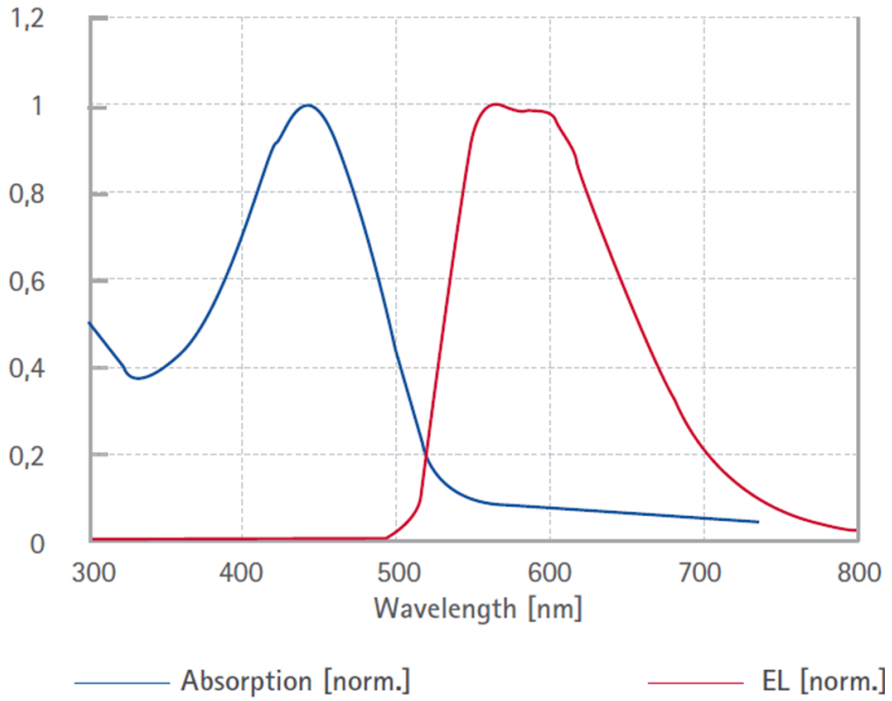

Figure 5.6: Absorption and emission spectra for SY. The blue curve is the absorption spectrum, and the red curve is the emission spectrum. Data from Merck SY data sheet (see appendix).

The emission from the transfer printed μLED transmitter and the emission from the external μLED that will be received and collected by the optical concentrator part of the transceiver are at 460 nm and 450 nm respectively. Because of the similarity in peak emission wavelengths, the emission from each μLED used in any VLC demonstration with this optical transceiver cannot be distinguished from one another if both μLEDs are driven simultaneously. To lower interference because of this during data acquisition experiments, a small circular area (diameter $\approx$ 3 mm) of the SY film that would be positioned directly under the μTP μLED was mechanically removed from the microscope slide. This is seen schematically in Figure 5.3.

The microscope slide with the SY film was then spin coated with the optical epoxy NOA 13685 (Norland Inc.), attached to the backside of the microscope slide where the μTP μLED was transfer printed, and UV cured (365 nm, 7 Jcm^{-2}). The completed optical transceiver can be seen in the photograph in Figure 5.7. The low refractive

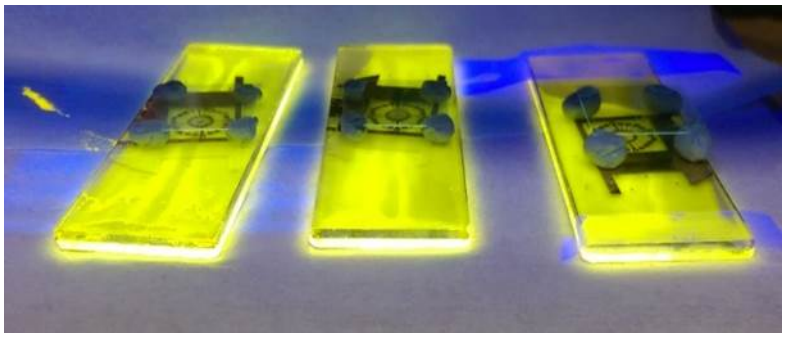

Figure 5.7: Photograph of the completed optical transceiver.

index of the NOA 13685 further reduces the interference caused by the transfer printed μLED and the unavoidably coupled light in the microscope slide it was transfer printed on, trapping most received light in the SY film on the bottom microscope slide. In Figure 5.7 we can see that most of the incident light collected by the fluorescent SY is trapped in the bottom microscope slide by the high refractive index NOA 13685 layer.

5.3 Characterisation of the Transceiver

5.3.1 Spectral Characteristics

A spectrum was taken directly under the μTP μLED and at one end facet of the transceiver, which will be referred to hereafter as detector position A and detector position B respectively. These positions are marked APD A and APD B in Figure 5.8 and correspond to light transmitted by the transfer printed μLED (spectrum A) and light collected and concentrated by the optical concentrator part of the transceiver device (spectrum B). These spectra can be seen in Figure 5.9 and were measured with an Avantes spectrometer (Avasoft 2048L).

The light at detector position A peaks at 460 nm (from the blue-emitting μTP μLED) and the spectrum taken at detector position B has two peaks, the major one at 563 nm from the colour-converted SY light and a smaller peak at 543 nm from unconverted blue light from the incident μLED, Figure 5.9. Perhaps one simple way to reduce the

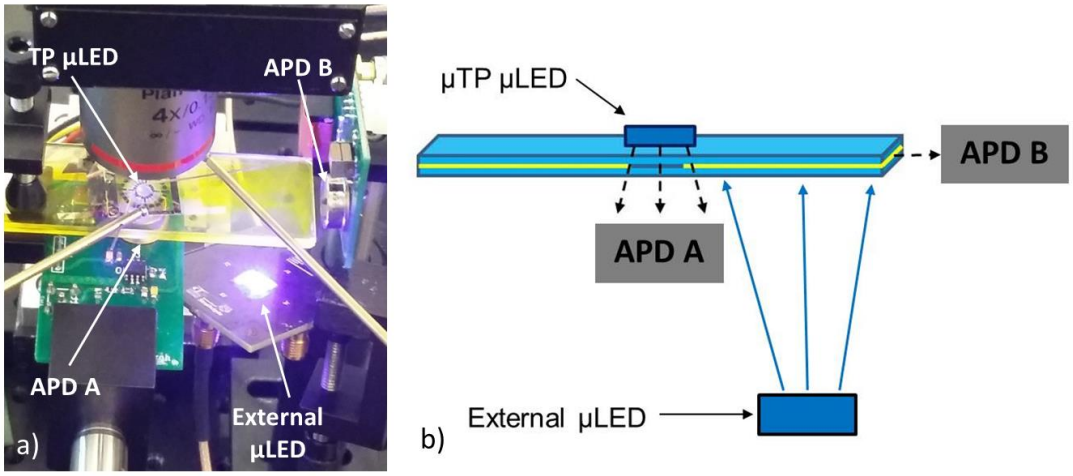

Figure 5.8: A a) photograph and b) schematic diagram of the setup used to demonstrate the optical transceiver device. APD A is used to detect light emitted from the μTP μLED, APD B is used to detect light received from the external μLED and concentrated onto the end facet of the transceiver device.

interference between both μLEDs (μTP and external) would be to use an external μLED emitting in the violet region rather than the 450 nm μLED used in this experiment.

5.3.2 Data Transmission

To demonstrate this optical transceiver, the data transmission rate was measured at detector point A and detector point B (as seen in Figure 5.8) with the μTP μLED and the external blue-emitting μLED simultaneously emitting modulated light. As in the other data transmission rate measurements discussed throughout this work, the μLEDs are driven by sending both a DC and a modulated AC signal from a DC power supply and AC signal generator respectively through a bias-tee. The setup used in these measurements is shown in Figure 5.8.

The data transmission rate, using OFDM, was measured for each μLED link: the μTP μLED straight through the transceiver structure to APD A (referred to in the following as link A), and colour-converted light from the μLED concentrated at the end facet of

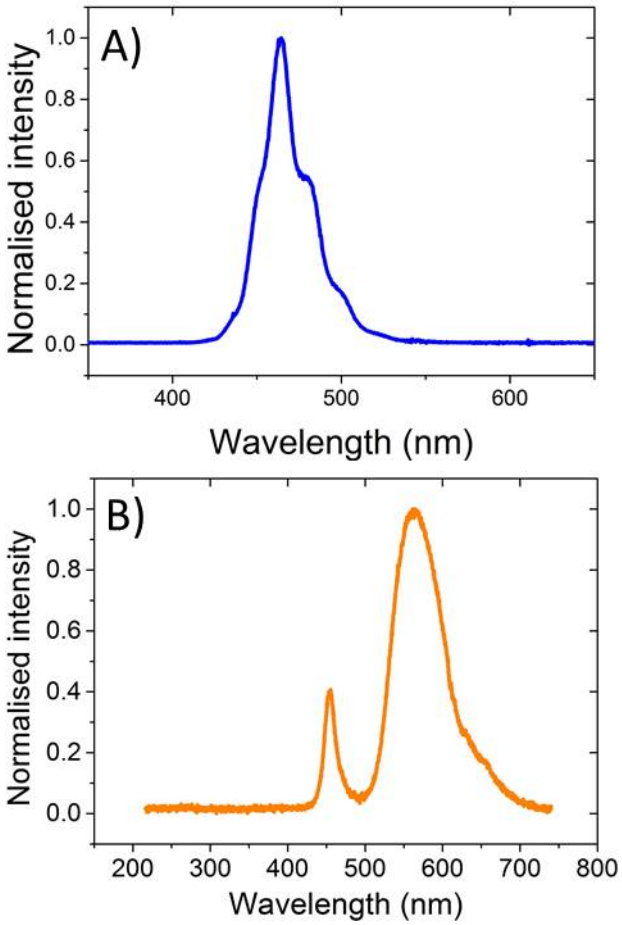

Figure 5.9: A) The spectrum taken at detector point A. B) The spectrum at detector point B.

the transceiver structure at APD B (referred to in the following as link B). The position of APD A, and APD B, is seen in Figure 5.8. The DC driving conditions for the μTP μLED are 6.1 V and 3 mA and the driving conditions for the external μLED are 4.1 V and 24 mA (as is required for these μTP μLEDs, the driving current was kept to below a safe upper-limit of 5 mA to prevent overheating).

The data transmission rates for these two μLED links are 165 Mbps and 413 Mbps for link A (the μTP μLED) and link B (external μLED link) respectively below the FEC level. These data transmission rates can be seen in Figure 5.10. The μTP μLED link data rate is limited to 165 Mbps because, as it is only driven at 3 mA, the optical power at APD A is fairly modest and the SNR not as high as for the external μLED.

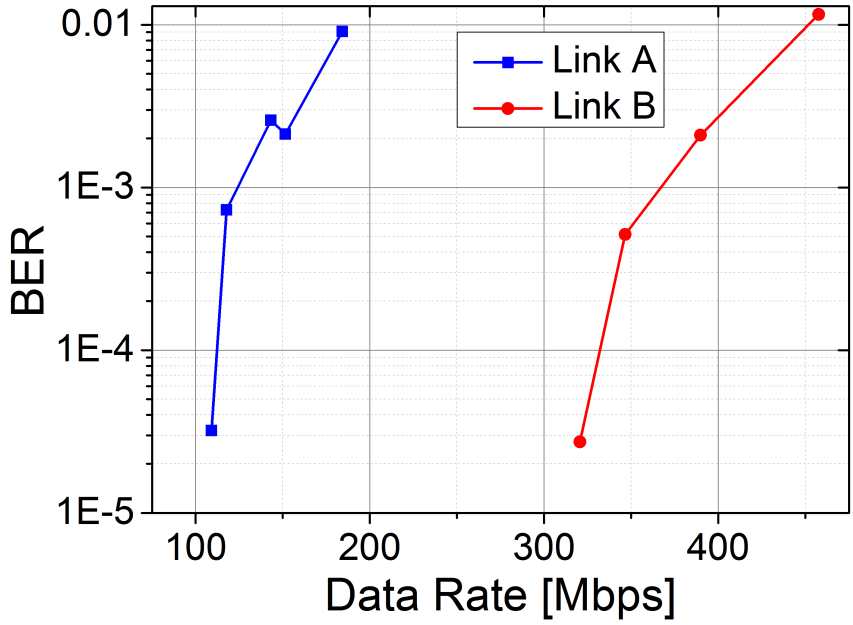

Figure 5.10: The data transmission vs BER results for link A and link B.

The APDs used in this demonstration, and used in all data transmission rate measurements with this transceiver, are from Hamamatsu (S8664-50K). This has a bandwidth of 60 MHz. The OFDM bandwidth used for both the μTP μLED and the external μLED is 45 MHz.

5.4 Optical Repeater

To show the functionality of the optical transceiver further, it was demonstrated as an optical repeater in a decode and forward regime. A schematic of this device can be seen in Figure 5.11. The setup for this demonstration is exactly the same as that for the demonstration of the device as an optical transceiver as in Figure 5.8. An incoming stream of bits is modulated into M-ary quadrature amplitude modulated (M-QAM) symbols before a Hermitian symmetry and fast Fourier transformation (FFT) operation is applied on N-FFT M-QAM symbols, where M is the constellation size. The resulting OFDM stream is transmitted to the transfer printed μLED through an

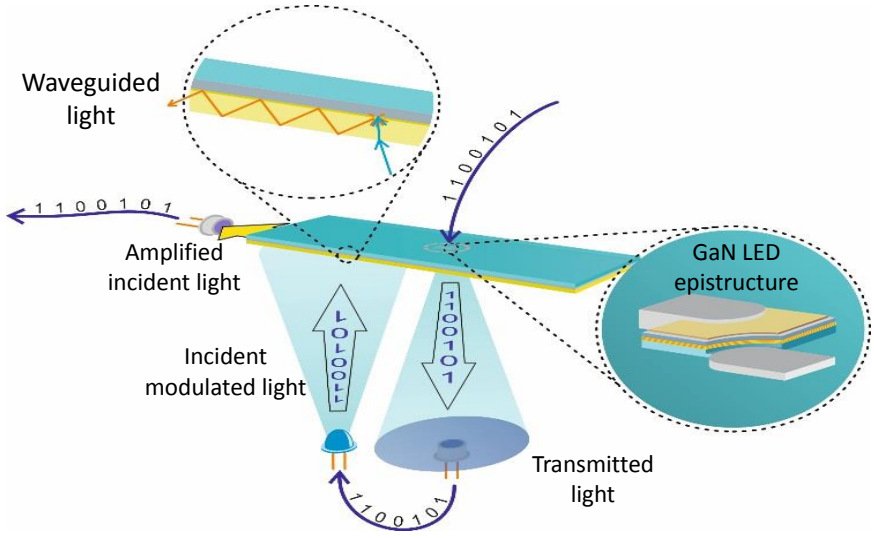

Figure 5.11: Concept for an optical transceiver and repeater. Data is transmitted from μTP μLED, and then relayed to the external μLED and collected by the concentrator.

arbitrary waveform generator (AWG) Agilent 81180A with a sampling frequency 720 MS/sec. A root raised cosine (RRC) pulse shaping filter is used with an oversampling factor of 8 which results in a single side modulation bandwidth of 45 MHz. This modulated signal is then fed to the μTP μLED which transmits this data, as seen in Figure 5.11. This is then detected by APD A (as seen in Figure 5.8).

The detected signal is sent to a Keysight 1 GHz mixed-signal oscilloscope (MSO7104B) and demodulated offline in MATLAB®, where all the signal processing operations are performed in a similar fashion to as in [146]. The demodulated M-QAM symbols are then remodulated and fed to the external μLED. The emitted light of the external μLED is collected by the concentrator and the data is detected at APD B. This transmission from the μTP μLED and re-transmission of the same data from the external μLED shows a proof-of-concept of the device working as an optical relay. Note that the relay concept was demonstrated in this way as the μTP μLED has the lower data transmission rate of the two μLEDs, and so was modulated first with the data then sent to the external μLED. In an ideal optical relay, the external μLED would have

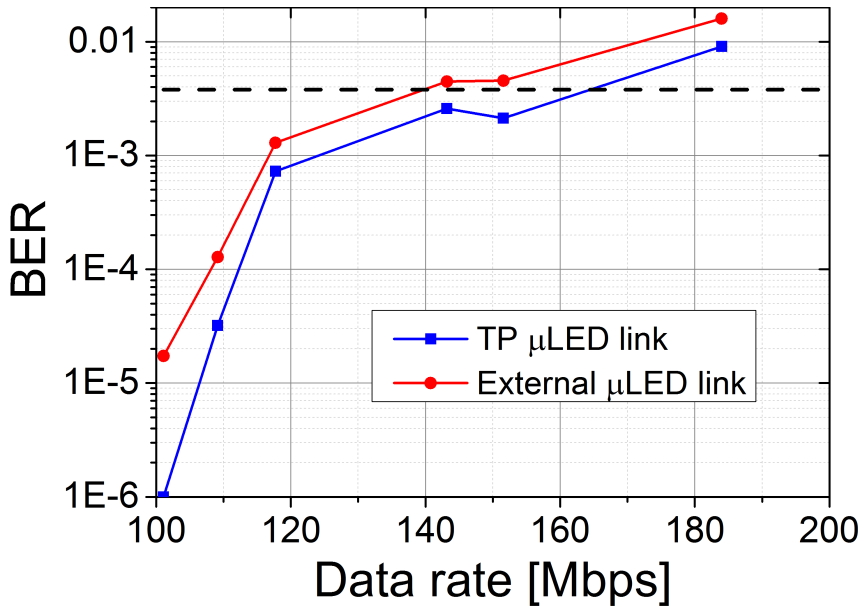

Figure 5.12: Data rates for the received and transmitted light in the optical relay system. The dashed line shows the FEC level.

been modulated first, with the collected data from it being retransmitted by the μTP μLED. However, with the performances of these μLEDs as shown in Figure 5.10, it was decided that to reduce issues the relay would be demonstrated as described above and shown in Figure 5.11. The Matlab® coding and data transmission results were led by Mr Mohamed Islim and Mr Yiang Lin from the LiFi R&D Centre at the University of Edinburgh.

Figure 5.12 shows the data transmission rates from the external μLED at APD B and the relayed data from the μTP μLED at APD A, which are limited to 140 Mbps and 165 Mbps below the FEC level. This data rate limitation is is due to the lower data transmission rate of the μTP μLED. The data transmission rate for the external μLED link when not in the relay, as quoted in Section 5.3.2, is plotted in the inset.

Figure 5.13 shows the transmitted and demodulated M-QAM symbols for both Links A and B. The symbols demodulated at APD B exhibit higher noise variance due to the additional demodulation process in the optical relay.

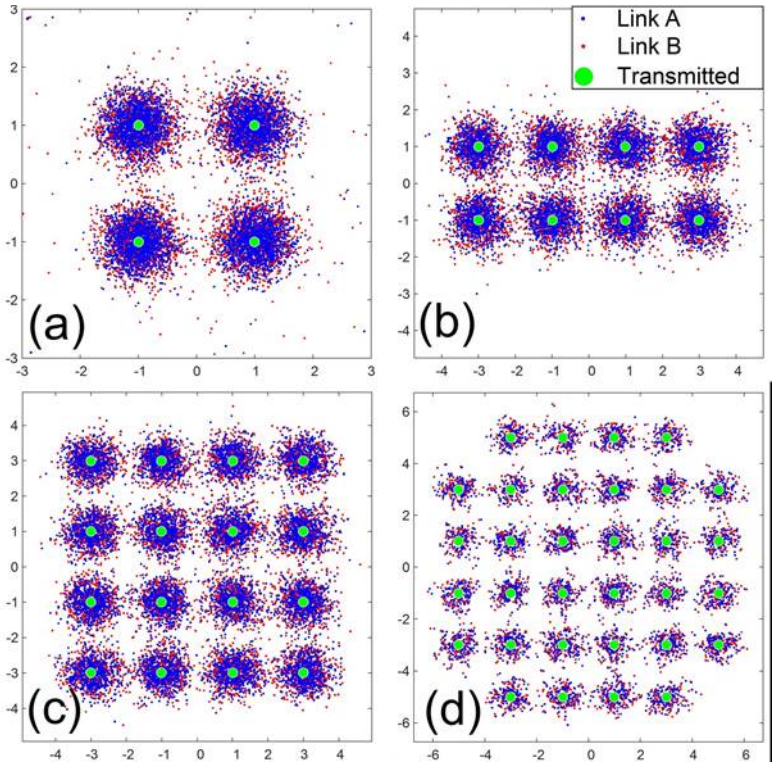

Figure 5.13: Received signal constellations for Link A and link B.(a) 4-QAM;(b) 8-QAM;(c) 16-QAM;(d) 32-QAM.

The QAM constellations for the received signal for link A and link B can be seen in Figure 5.13. These show us the noise variance in transmitted and received signals, the received signals from link B show more difference to the transmitted signal due to the additional demodulation and remodulation steps required.

5.5 Summary

In this Chapter, the concept of an optical transceiver has been discussed. The μTP technique has enabled an extra transmitting function to be added to an optical concentrator, where a blue-emitting μLED has been printed onto one. This creates a device capable of simultaneously transmitting modulated light from the μTP μLED and capturing modulated light from an external μLED.

The spectral and data transmission characteristics of this integrated transceiver device have been explored and we have shown that it is possible to distinguish two separate data streams from both the μTP μLED (165 Mbps) and the light received from the external μLED (413 Mbps). The transceiver device as an optical repeater has also been investigated.

Chapter 6

Conclusion and outlook

6.1 Conclusion

The work presented here has focused on the heterogenous integration of blue-emitting InGaN-based μLEDs onto various non-native substrates for VLC applications. This work built on previous efforts over the past decade or so in pioneering the transfer printing technique and the use of elastomeric stamps with reversible adhesion to pick-up and print micro-and nano-scale semiconductor devices. In particular, the transfer printing done throughout this PhD work makes use of a modified nano-lithography system and expands on techniques developed by Dr. António Trindade [94, 95] during his PhD project at the Institute of Photonics.

Chapter 1 gave an introduction to the basic operating principles of LEDs and their properties, with a particular focus on those fabricated from the III-nitrides. The operation of electrically addressed LEDs was described, introducing the bandgap in semiconductor materials and how material structure therefore contributes to the light emission from LEDs. The physics of the pn junction was also discussed with attention paid to it in the context of LED operation. Material growth techniques for InGaN based LEDs were discussed at length, as well as the growth of III-nitride material-based alloys in

general. This materials system is important as it can cover the entire visible spectrum, and the quantum well engineering required to yield LED emission across this range from this materials system was covered. When discussing the growth of InGaN LED epistructures, the advantages and disadvantages of growth on silicon was looked into, as this is the basis for the LEDs fabricated for the work presented in this thesis. The challenges associated with strain when growing InGaN LEDs on various substrates, as well as the strain associated with the fabrication of the LEDs for the transfer printing process were discussed.

The first chapter then gives an introduction to the concept of VLC. The basic ideas and motivations behind this communication method were discussed, introducing the idea of the RF bottleneck caused by the ever increasing desire for more and more data communications bandwidths. The introduction of how optical sources, and in particular LEDs, can be used to transmit information through fibres or free-space by modulating the emission intensity was given. The two main ways of determining the suitability of an LED for VLC were then introduced: modulation bandwidth and data transmission rate measurements. The experimental techniques for taking these sets of measurements were described. The chapter ended with a discussion on a few data encoding techniques for fast data transmission with μLED sources, including OFDM which is the technique used for data transmission with the μLEDs fabricated and used throughout this work.

During the second chapter, the μTP technique was introduced. For the implementation of the transfer printing technique used throughout this work, several cleanroom fabrication techniques were used. These were described in detail in this chapter. Micro-transfer printing is facilitated by elastomeric stamps, made from PDMS, and the ability to kinetically control the adhesion between various surfaces. The theory behind these stamps was detailed in this chapter, along with the cleanroom fabrication process used to fabricate them for my transfer printing work.

Suspended μLEDs are fabricated for the transfer printing work in this thesis using a variety of dry and wet cleanroom processes. The μLEDs are patterned using standard UV photolithography: spin coating, exposure and development. Various plasma etching

processes are implemented to etch the n-mesa and define the supporting anchors for the suspended array of the μLEDs. To suspend these μLEDs the underlying silicon substrate is removed, and the wet underetch process is described in this chapter.

Chapter 3 reports the fabrication and characterisation of a dual-colour integrated μLED device. This device was designed with the intention of it being used for VLC applications and the motivation for it was described at the beginning of this chapter. The fabrication process for this dual-colour device was then detailed. First a 2 x 4 array of green-emitting μLEDs was fabricated from an InGaN LED wafer on sapphire. The IV and LI characteristics of these green μLEDs were then studied, as well as the modulation bandwidth. Blue-emitting μLEDs were then transfer printed into this array, between the green pixels. This gives 2 x 8 array of alternating blue and green μLED pixels. The post transfer printing process to electrically address the μLED array with metal tracks was outlined. The characterisation of the blue-emitting μLEDs in the array was done similarly to with the green-emitting pixels with IV, LI and modulation bandwidths measured. The combined device was then characterised, with spectral and data transmission measurements taken. The data transmission rate from the device was measured in ganging regime first, where a single stream of data was sent with both LEDs simultaneously driven. The device was then used to demonstrate WDM, where two discrete streams of data are sent from a μLED pair. In the ganging regime, the device has an optical data transmission rate of 360 Mbps. When measured in a WDM regime, the device transmits data at 464 Mbps.

Chapter 4 deals with the fabrication and characterisation of more devices intended for VLC applications, this time μLEDs integrated with a CQD flexible glass platform. This work is the first time μLEDs have been reported transfer printed onto flexible glass. The physics behind CQDs was discussed, before the concept of them as colour converters. In these colour-converting integrated devices, the μLEDs are transfer printed directly onto thin glass without the aid of an adhesive interlayer. This is facilitated via liquid capillary bonding which is discussed in this chapter. The flexible glass with μLEDs printed on it is then used to encapsulate CQDs, with this process detailed. The

characterisation of the integrated μLED-colour-converter devices was then discussed. The absorption and forward power efficiency was measured as well as the modulation bandwidth and data transmission rates achieved by these integrated devices.

The final chapter in this thesis expands on the ideas from chapter 4. An integrated optical transceiver is fabricated by transfer printing a μLED onto an optical antenna. These optical antennae are discussed at length at the beginning of the chapter, along with the motivations for fabricating the dual-purpose optical transceiver. In depth characterisation of the data transmission and receiving capabilities of the transceiver was done.

6.2 Future work

With the advances in μTP over the past few years, it should now be possible to print semiconductor devices on virtually any flat enough substrate, possibly without the use of an adhesive interlayer. In terms of future prospects for the μTP of LEDs and other semiconductor devices onto new and capability enhancing substrates, the potential impact of μTP as a technique for heterogenous integration is great. As an additive fabrication technique, new forms of mechanical stacking and assembly become possible. With several papers being published over the past few years demonstrating its potential for the integration of III-Vs with Si, for example in [93, 147], its clear that this is an area where the technique will have an impact.

In terms of taking the work discussed in the earlier chapters of this thesis forward, one major follow up step would be to expand on the dual colour integrated device. One immediate plan is to make a device for a dual-colour MIMO experiment. MIMO (multiple input, multiple output) is a technique used to increase capacity in a data transmission link by using multiple sources and multiple receivers. Specially designed μLED arrays, as in [148], such that the spatial separation of multiple pixels can be used to send multiple data streams simultaneously. By this theory, a dual-colour array, with

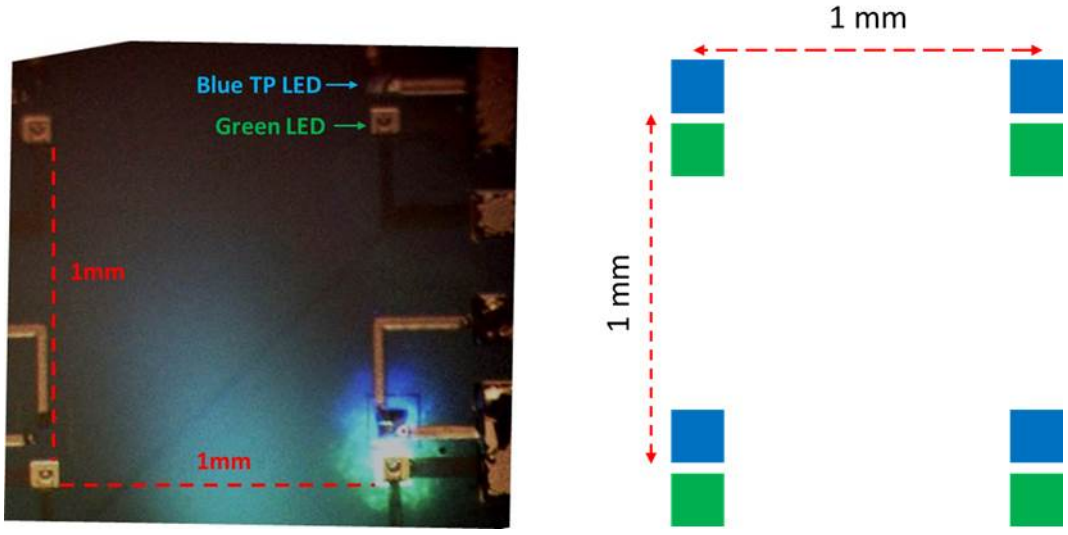

Figure 6.1: Concept for a dual-colour MIMO μLED array.

known separation between each dual-colour pair of μLED pixels can be used to send twice the streams of data than a single-colour μLED array. The array that will soon be fabricated by colleagues at the Institute of Photonics, using techniques similar to those outlined in Section 3.3 is shown in the microscope image in Figure 6.1. This 2 x 2 array of blue-green pairs allows detectors to both spatially and spectrally separate which data came from each μLED and so 8 streams of data can be sent simultaneously from the device. As Figure 6.1 shows, the entire array is a little over 1 mm in size, and so has the potential for larger arrays on small chips to send large amounts of simultaneous data.

This dual-colour device could also be extended to produce a RGB array, by using μTP to mechanically stack an AlGaInP red colour-converting membrane and a blue-emitting μLED ontop of one another into the array. Tests on μTP these red AlGaInP colour-converting membranes have been done at the IoP already and, while challenging, further work should lead to the ability to accurately print these.

As just discussed, MIMO is a form of spatial multiplexing which allows for high speed parallel data transmission by modulating multiple individual μLEDs simultaneously. To address multiple μLEDs like this, the use of complementary metal-oxide-semiconductor

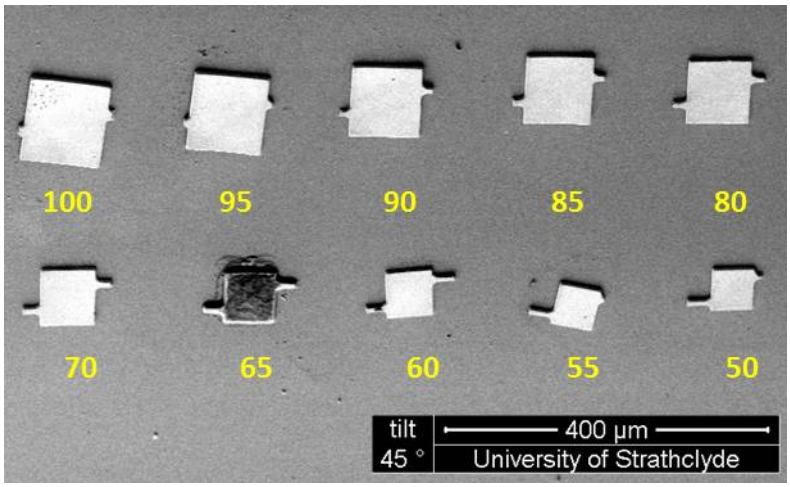

Figure 6.2: SEM image of different sizes of platelets fabricated from GaN-on-Si printed on glass via capillary bonding.

(CMOS) controlled μLED arrays has been reported by colleagues [28, 149]. CMOS enables the driving of multiple μLEDs via a computer interface. μTP can be used to print μLEDs directly onto CMOS, and is already starting to be demonstrated here at the Institute of Photonics. The aim is to demonstrate high-density parallel μTP onto CMOS, by printing large arrays at once with specially designed elastomeric stamps, rather that one at a time as has predominantly been done so far.

The use of smaller μLEDs offers clear advantages, they can be driven to higher current densities and therefore can be modulated faster for high speed data communications. Colleagues at the IoP have already begun work on producing and printing platelets down from 100 μm to 30 μm, with several different platelets in different sizes seen in Figure 6.2.

The ability to fabricate and print smaller μLEDs means that they can be utilised on smaller surfaces. This is being realised in an ongoing PhD project of Antoine Boudet at the Institute of Photonics on printing blue-emitting 50 μm onto diamond neural probes for optogenetics experiments. Neural probes with μLEDs have been fabricated already from GaN-on-Si, as by *McAlinden et al* [150], with μTP being used to fabricate similar probes by Kim et al. [90].

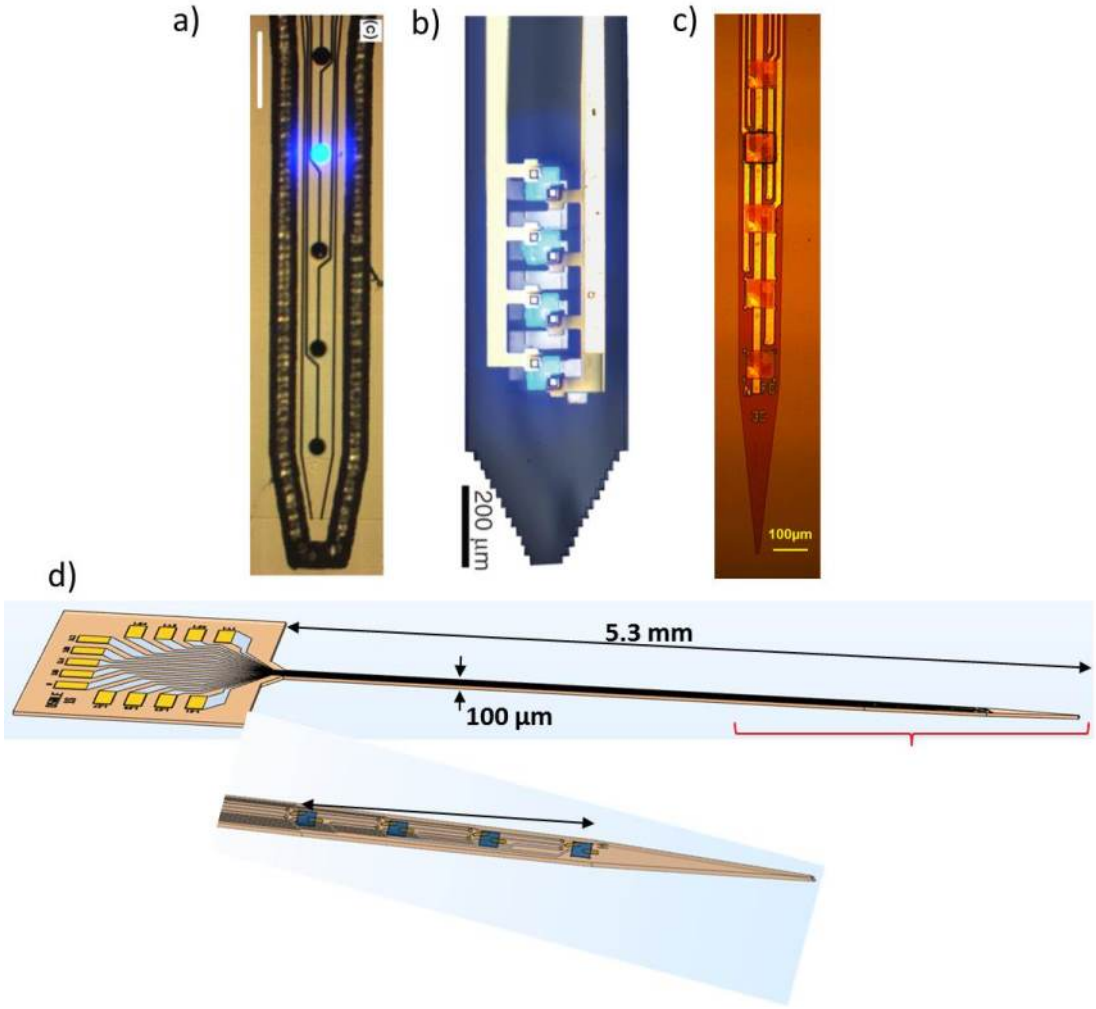

Figure 6.3: a) A neural probe with μLEDs, b) a neural probe fabricated via μTP, c) a test neural probe design for d) a μTP-diamond-neural probe.

Figure 6.3 shows these neural probes with μLEDs as fabricated directly from GaN-on-Si (Figure 6.3 a)), using μTP to print μLEDs onto flexible probes (Figure 6.3 b))and printing a test μLED array on diamond (Figure 6.3 c)) to fabricate a probe as seen schematically in Figure 6.3 d). Using diamond as the main probe material will spread heat more effectively, allowing for more efficient light emission from the μTP μLEDs as well as preventing heat damage to the neural tissue from the μLED.

Bibliography

[1] H. J. Round, "A note on carborundum," *Electrical World*, vol. 1, no. 49, p. 309, 1907.

[2] R. A. Logan, H. G. White, and W. Wiegmann, "Efficient green electroluminescence in nitrogen-doped gap p-n junctions," *Applied Physics Letters*, vol. 13, no. 4, pp. 139–141, 1968.

[3] W. O. Groves, A. H. Herzog, and M. G. Craford, "The effect of nitrogen doping on GaAs1-xPx electroluminescent diodes," *Applied Physics Letters*, vol. 19, no. 6, pp. 184–186, 1971.

[4] "The Nobel Prize in Physics 2014." [Online]. Available: https://www.nobelprize.org/nobel{_}prizes/physics/laureates/2014/

[5] H. Amano, N. Sawaki, I. Akasaki, and Y. Toyoda, "Metalorganic vapor phase epitaxial growth of a high quality GaN film using an AlN buffer layer," *Applied Physics Letters*, vol. 48, no. 5, pp. 353–355, 1986.

[6] H. Amano, M. Kito, K. Hiramatsu, and I. Akasaki, "P-Type Conduction in Mg-Doped GaN Treated with Low-Energy Electron Beam Irradiation (LEEBI)," *Japanese Journal of Applied Physics*, vol. 28, no. Part 2, No. 12, pp. L2112–L2114, 1989.

[7] S. Nakamura, T. Mukai, and M. Senoh, "Candela-class high-brightness InGaN/AlGaN double-heterostructure blue-light-emitting diodes," *Applied Physics Letters*, vol. 64, no. 13, pp. 1687–1689, 1994.

[8] J. J. Wierer, J. Y. Tsao, and D. S. Sizov, "Comparison between blue lasers and light-emitting diodes for future solid-state lighting," *Laser and Photonics Reviews*, vol. 7, no. 6, pp. 963–993, 2013.

[9] E. Matioli and C. Weisbuch, "Impact of photonic crystals on LED light extraction efficiency: approaches and limits to vertical structure designs," *Journal of Physics D: Applied Physics*, vol. 43, no. 35, p. 354005, 2010.

[10] C.-H. Chiu, C.-Y. Lee, C.-Y. Liu, B.-W. Lin, C.-C. Lin, W.-C. Hsu, and J.-K. Sheu, "Enhancing light extraction from LEDs," *SPIE*, vol. 1, pp. 2–4, 2010.

[11] Y.-C. Lee, C.-H. Ni, and C.-Y. Chen, "Enhancing light extraction mechanisms of GaN-based light-emitting diodes through the integration of imprinting microstructures, patterned sapphire substrates, and surface roughness." *Optics Express*, vol. 18 Suppl 4, pp. A489–A498, 2010. [Online]. Available: http://www.ncbi.nlm.nih.gov/pubmed/21165080

[12] M. Auf Der Maur, A. Pecchia, G. Penazzi, W. Rodrigues, and A. Di Carlo, "Efficiency Drop in Green InGaN/GaN Light Emitting Diodes: The Role of Random Alloy Fluctuations," *Physical Review Letters*, vol. 116, no. 2, p. 027401, 2016.

[13] Osram, [Online]. Available: https://www.osram.com/osram{_}com/products/led-technology/lamps/consumer-led-lamps-with-classic-bulbs/led-star-classic-a/index.jsp

[14] "Inhabitat: LED traffic lights take to Taiwan." [Online]. Available: http://inhabitat.com/taiwans-led-traffic-lights/

[15] "Samsung US: 2015 LED TV (J400x Series) Owner information." [Online]. Available: http://www.samsung.com/us/support/owners/product/2015-led-tv-j400x-series

[16] "Audi: Lighting." [Online]. Available: https://www.audi.co.uk/about-audi/latest-news/ding-dong-merrily-on-high-beam-with-the-audi-lighting-pioneers.html

[17] J. K. Kim and E. F. Schubert, "Transcending the replacement paradigm of solid-state lighting." *Optics express*, vol. 16, no. 26, pp. 21 835–21 842, 2008.

[18] H. T. Whelan, J. M. Houle, N. T. Whelan, D. L. Donohoe, J. Cwiklinski, M. H. Schmidt, L. Gould, D. Larson, G. a. Meyer, V. Cevenini, and H. Stinson, "The NASA Light-Emitting Diode Medical Program Progress in Space Flight and Terrestrial Applications," *Journal Of Neurosurgery*, pp. 1995–1999, 1999.

[19] M.-K. Lu, F.-C. Chang, W.-Z. Wang, C.-C. Hsieh, and F.-J. Kao, "Compact light-emitting diode lighting ring for video-assisted thoracic surgery," *Journal of biomedical optics*, vol. 19, no. 10, p. 105004, 2014.

[20] A. C. H. Lee, D. S. Elson, M. A. Neil, S. Kumar, B. W. Ling, F. Bello, and G. B. Hanna, "Solid-state semiconductors are better alternatives to arc-lamps for efficient and uniform illumination in minimal access surgery," *Surgical Endoscopy and Other Interventional Techniques*, vol. 23, no. 3, pp. 518–526, 2009.

[21] P. Swain, R. Austin, K. Bally, and R. Trusty, "Development and testing of a tethered, independent camera for NOTES and single-site laparoscopic procedures," *Surgical Endoscopy and Other Interventional Techniques*, vol. 24, no. 8, pp. 2013–2021, 2010.

[22] "Cree News: Cree First to Break 300 Lumens-Per-Watt Barrier." [Online]. Available: http://www.cree.com/News-and-Events/Cree-News/Press-Releases/2014/March/300LPW-LED-barrier

[23] "Lumileds: LUXEON 3535L Line." [Online]. Available: http://www.lumileds.com/products/mid-power-leds/luxeon-3535l

[24] "The energy saving trust: Low energy lighting." [Online]. Available: http://www.energysavingtrust.org.uk/sites/default/files/reports/ESTLightingGuide-theRightLight.

[25] E. F. Schubert, J. K. Kim, H. Luo, and J.-Q. Xi, "Solid-state lightinga benevolent technology," *Reports on Progress in Physics*, vol. 69, no. 12, pp. 3069–3099, 2006.

[26] D. Zhu, D. J. Wallis, and C. J. Humphreys, "Prospects of III-nitride optoelectronics grown on Si," *Reports on Progress in Physics*, vol. 76, no. 10, p. 106501, 2013. [Online]. Available: http://stacks.iop.org/0034-4885/76/i=10/a=106501?key=crossref.71ea08c680fd69e84d5d8d40070a2905

[27] C. Du, Z. Ma, J. Zhou, T. Lu, Y. Jiang, P. Zuo, H. Jia, and H. Chen, "Enhancing the quantum efficiency of InGaN yellow-green light-emitting diodes by growth interruption," *Applied Physics Letters*, vol. 105, no. 7, p. 071108, 2014. [Online]. Available: http://dx.doi.org/10.1063/1.4892830

[28] J. J. D. McKendry, D. Massoubre, S. Zhang, B. R. Rae, R. P. Green, E. Gu, R. K. Henderson, A. E. Kelly, and M. D. Dawson, "Visible-Light Communications Using a CMOS-Controlled Micro-Light- Emitting-Diode Array," *Journal of Lightwave Technology*, vol. 30, no. 1, pp. 61–67, 2012.

[29] J. J. D. McKendry, D. Tsonev, R. Ferreira, S. Videv, A. D. Griffiths, S. Watson, E. Gu, A. E. Kelly, H. Haas, and M. D. Dawson, "Gb/s single-LED OFDM-based VLC using violet and UV Gallium nitride micro- LEDs," in *2015 IEEE Summer Topicals Meeting Series*, vol. 1, 2015, pp. 175–176.

[30] H. Young and R. Freedman, *University Physics with Modern Physics*. Pearson Education, 2007.

[31] E. F. Schubert, *Light-Emitting Diodes*, 2nd ed. Cambridge University Press, 2006.

[32] H. Masui, S. Nakamura, and S. P. DenBaars, "Technique to evaluate the diode ideality factor of light-emitting diodes," *Applied Physics Letters*, vol. 96, no. 7, pp. 1–4, 2010.

[33] K. Mayes, A. Yasan, R. McClintock, D. Shiell, S. R. Darvish, P. Kung, and M. Razeghi, "High-power 280 nm AlGaN light-emitting diodes based on an asymmetric single-quantum well," *Applied Physics Letters*, vol. 84, no. 7, pp. 1046–1048, 2004.

[34] D. Zhu, J. Xu, A. N. Noemaun, J. K. Kim, E. F. Schubert, M. H. Crawford, and D. D. Koleske, "The origin of the high diode-ideality factors in GaInN/GaN multiple quantum well light-emitting diodes," *Applied Physics Letters*, vol. 94, no. 8, pp. 2007–2010, 2009.

[35] X. A. Cao, J. M. Teetsov, M. P. D'Evelyn, D. W. Merfeld, and C. H. Van, "Electrical characteristics of InGaN/GaN light-emitting diodes grown on GaN and sapphire substrates," *Applied Physics Letters*, vol. 85, no. 1, pp. 7–9, 2004.

[36] Y.-j. LIU, C.-c. HUANG, T.-y. CHEN, C.-s. HSU, S.-y. CHENG, K.-w. LIN, J.-k. LIOU, and W.-c. LIU, "Improved performance of GaN-based light-emitting diodes by using short-period superlattice structures," *Progress in Natural Science: Materials International*, vol. 20, pp. 70–75, 2010. [Online]. Available: http://www.sciencedirect.com/science/article/pii/S1002007112600094

[37] Y. Taniyasu, M. Kasu, and T. Makimoto, "An aluminium nitride light-emitting diode with a wavelength of 210 nanometres." *Nature*, vol. 441, no. 7091, pp. 325–328, 2006.

[38] S. Nakamura, Y. Harada, and M. Seno, "Novel metalorganic chemical vapor deposition system for GaN growth," *Applied Physics Letters*, vol. 58, no. 18, pp. 2021–2023, 1991.

[39] "http://www.palomartechnologies.com/blog/bid/146914/
The-ABCs-of-LEDs-MOCVD-Matrix-LED-Assemblies-Niche-Markets

[40] S. Nakamura and G. Fasol, *The Blue Laser Diode: GaN Based Light Emitters and Lasers*, 2nd ed. Springer-Verlag Berlin Heidelberg, 2000.

[41] S. A. Kukushkin, A. V. Osipov, V. N. Bessolov, B. K. Medvedev, V. K. Nevolin, and K. A. Tcarik, "Substrates for epitaxy of gallium nitride: New materials and techniques," *Reviews on Advanced Materials Science*, vol. 17, no. 1-2, pp. 1–32, 2008.

[42] F. A. Ponce and D. P. Bour, "Nitride-based semiconductors for blue and green light-emitting devices," *Nature*, vol. 386, pp. 351–359, 1997.

[43] K. S. Ramaiah, Y. K. Su, S. J. Chang, B. Kerr, H. P. Liu, I. G. Chen, K. S. Ramaiah, Y. K. Su, S. J. Chang, and B. Kerr, "Characterization of InGaN / GaN multi-quantum-well blue-light-emitting diodes grown by metal organic chemical vapor deposition Characterization of InGaN/GaN multi-quantum-well blue-light-emitting diodes grown by metal organic chemical vapor deposition," *Applied Physics Letters*, vol. 3307, no. 2004, pp. 6–9, 2013.

[44] T. Egawa, B. Zhang, and H. Ishikawa, "High performance of InGaN LEDs on (111) silicon substrates grown by MOCVD," *IEEE Electron Device Letters*, vol. 26, no. 3, pp. 169–171, 2005.

[45] H. Ishikawa, G.-Y. Zhao, N. Nakada, T. Egawa, T. Jimbo, and M. Umeno, "GaN on Si Substrate with AlGaN / AlN Intermediate Layer Surfaces by Metalorganic Hydrogen Chloride Vapor-Phase Epitaxy GaN on Si Substrate with AlGaN / AlN Intermediate Layer," *Japanese Journal of Applied Physics*, vol. 38, no. 5A, pp. L492–L494, 1999.

[46] D. Zhu, C. McAleese, M. Haberlen, C. Salcianu, T. Thrush, M. Kappers, A. Phillips, P. Lane, M. Kane, D. Wallis, T. Martin, M. Astles, N. Hylton, P. Dawson, and C. Humphreys, "Efficiency measurement of GaN-based quantum well and light-emitting diode structures grown on silicon substrates," *Journal of Applied Physics*, vol. 109, no. 1, p. 014502, 2011. [Online]. Available: http://link.aip.org/link/JAPIAU/v109/i1/p014502/s1{&}Agg=doi

[47] T. Egawa, T. Moku, H. Ishikawa, K. Ohtsuka, and T. Jimbo, "Improved characteristics of blue and green InGaN-based light-emitting diodes on Si grown by metalorganic chemical vapor deposition," *Japanese Journal of Applied Physics, Part 2: Letters*, vol. 41, no. 6 B, pp. 4–6, 2002.

[48] A. Dadgar, M. Poschenrieder, A. Reiher, J. Bläsing, J. Christen, A. Krtschil, T. Finger, T. Hempel, A. Diez, and A. Krost, "Reduction of stress at the initial

stages of GaN growth on Si(111)," *Applied Physics Letters*, vol. 82, no. 1, pp. 28–30, 2003.

[49] S. X. Jin, J. Li, J. Z. Li, J. Y. Lin, and H. X. Jiang, "GaN microdisk light emitting diodes," *Applied Physics Letters*, vol. 76, no. 5, pp. 631–633, 2000. [Online]. Available: http://aip.scitation.org/doi/10.1063/1.125841

[50] H. X. Jiang and J. Y. Lin, "Nitride micro-LEDs and beyond–a decade progress review," *Optics express*, vol. 21, no. S3, pp. A475–84, 2013. [Online]. Available: http://www.ncbi.nlm.nih.gov/pubmed/24104436

[51] M. D. Dawson and M. a. a. Neil, "Micro-pixellated LEDs for science and instrumentation," *Journal of Physics D: Applied Physics*, vol. 41, no. 9, pp. 090 301–090 301, 2008. [Online]. Available: http://stacks.iop.org/0022-3727/41/i=9/a=090301?key=crossref.3c1c08222e0f30ae32e6f893598c4322

[52] S. Rajbhandari, J. J. D. Mckendry, J. Herrnsdorf, H. Chun, G. Faulkner, H. Haas, I. M. Watson, D. O. Brien, and M. D. Dawson, "A review of Gallium Nitride LEDs for multi-gigabit-per-second visible light data communications," *Semiconductor Science and Technology*, pp. 1–44, 2016.

[53] H. X. Zhang, D. Massoubre, J. McKendry, Z. Gong, B. Guilhabert, C. Griffin, E. Gu, P. E. Jessop, J. M. Girkin, and M. D. Dawson, "Individually-addressable flip-chip AlInGaN micropixelated light emitting diode arrays with high continuous and nanosecond output power." *Optics express*, vol. 16, no. 13, pp. 9918–9926, 2008.

[54] S. X. Jin, J. Li, J. Y. Lin, and H. X. Jiang, "InGaN/GaN quantum well interconnected microdisk light emitting diodes," *Applied Physics Letters*, vol. 77, no. 20, p. 3236, 2000. [Online]. Available: http://link.aip.org/link/APPLAB/v77/i20/p3236/s1{&}Agg=doi

[55] S. X. Jin, J. Shakya, J. Y. Lin, and H. X. Jiang, "Size dependence of III-nitride microdisk light-emitting diode characteristics," *Applied Physics Letters*, vol. 78, no. 22, pp. 3532–3534, 2001.

[56] M. Vaculovicova, M. Akther, P. Maaskant, D. Brabazon, and M. Macka, "Fibre coupled micro-light emitting diode array light source with integrated band-pass filter for fluorescence detection in miniaturised analytical systems," *Analytica Chimca Acta*, pp. 85–92, 2015. [Online]. Available: http://ac.els-cdn.com/S0003267015002226/1-s2.0-S0003267015002226-main.pdf?{_}tid=b8292d60-88c4-11e7-88b0-00000aab0f6b{&}acdnat=1503576594{_}4b8efea8d5e70eb04d52a264f552f3f4

[57] J. Day, J. Li, D. Y. C. Lie, C. Bradford, J. Y. Lin, and H. X. Jiang, "III-Nitride full-scale high-resolution microdisplays," *Applied Physics Letters*, vol. 99, no. 3, pp. 1–4, 2011.

[58] M. Meneghini, A. Tazzoli, G. Mura, G. Meneghesso, and E. Zanoni, "A review on the physical mechanisms that limit the reliability of GaN-based LEDs," *IEEE Transactions on Electron Devices*, vol. 57, no. 1, pp. 108–118, 2010.

[59] P. Tian, A. Althumali, E. Gu, I. M. Watson, M. D. Dawson, and R. Liu, "Aging characteristics of blue InGaN micro-light emitting diodes at an extremely," *Semiconductor Science and Technology*, vol. 31, p. 7, 2016.

[60] J. J. D. McKendry, R. P. Green, A. E. Kelly, Z. Gong, B. Guilhabert, D. Massoubre, E. Gu, and M. D. Dawson, "High-speed visible light communications using individual pixels in a micro light-emitting diode array," *IEEE Photonics Technology Letters*, vol. 22, no. 18, pp. 1346–1348, 2010.

[61] S. Fletcher, "Cellular Architecture and Key Technologies for 5G Wireless Communication Networks," *IEEE Communications Magazine*, vol. 1, no. February, pp. 122–130, 2014.

[62] H. Haas, L. Yin, Y. Wang, and C. Chen, "What is LiFi ?" *Journal of Lightware Technology*, vol. 34, no. 6, pp. 1533–1544, 2015.

[63] G. Pang, T. Kwan, C.-h. Chan, and H. Liu, "Title LED Traffic Light as Communication Device," in *IEEE/IEEJ/JSAI Int. Conf. on Intelligent Transportation Systems*, 1999.

[64] H. Chun, S. Rajbhandari, G. Faulkner, D. Tsonev, E. Xie, J. J. D. McKendry, E. Gu, M. D. Dawson, D. C. O'Brien, and H. Haas, "LED based wavelength division multiplexed 10 Gb/s visible light communications," *Journal of Lightwave Technology*, vol. 34, no. 13, pp. 3047–3052, 2016.

[65] D. Tsonev, S. Videv, and H. Haas, "Towards a 100 Gb/s visible light wireless access network," *Optics Express*, vol. 23, no. 2, p. 1627, 2015. [Online]. Available: http://www.opticsinfobase.org/abstract.cfm?URI=oe-23-2-1627

[66] G. Cossu, W. Ali, R. Corsini, and E. Ciaramella, "Gigabit-class optical wireless communication system at indoor distances (15 4 m)," *Optics Express*, vol. 23, no. 12, p. 15700, 2015.

[67] S. Hranilovic and F. Kschischang, "A pixelated MIMO wireless optical communication system," *IEEE Journal of Selected Topics in Quantum Electronics*, vol. 12, no. 4, pp. 859–874, 2006. [Online]. Available: http://ieeexplore.ieee.org/lpdocs/epic03/wrapper.htm?arnumber=1668130

[68] S. Rajbhandari, A. V. N. Jalajakumari, H. Chun, G. Faulkner, K. Cameron, R. Henderson, D. Tsonev, H. Haas, E. Xie, J. J. D. Mckendry, J. Herrnsdorf, R. Ferreira, M. D. Dawson, and D. O. Brien, "A Multi - Gigabit / sec Integrated Multiple - Input Multiple - Output VLC Demonstrator," *Journal of Lightwave Technology*, vol. 35, no. 20, pp. 4358–4365, 2017.

[69] J. M. Senior and M. Y. Jamro, *Optical Fiber Communications: Principles and Practice*. Pearson, 2009.

[70] R. P. Green, J. J. D. McKendry, D. Massoubre, E. Gu, M. D. Dawson, and A. E. Kelly, "Modulation bandwidth studies of recombination processes in blue and green InGaN quantum well micro-light-emitting diodes," *Applied Physics Letters*, vol. 102, no. 9, pp. 1–5, 2013.

[71] I. Reklaitis, F. Nippert, R. Kudzma, T. Malinauskas, S. Karpov, I. Pietzonka, H. J. Lugauer, M. Strassburg, P. Vitta, R. Tomasiunas, and A. Hoffmann, "Dif-

ferential carrier lifetime in InGaN-based light-emitting diodes obtained by small-signal frequency-domain measurements," *Journal of Applied Physics*, vol. 121, no. 3, p. 035701, 2017.

[72] R. X. G. Ferreira, E. Xie, J. J. D. McKendry, S. Rajbhandari, H. Chun, G. Faulkner, S. Watson, A. E. Kelly, E. Gu, R. V. Penty, I. H. White, D. C. O'Brien, and M. D. Dawson, "High bandwidth GaN-based micro-LEDs for multi-Gbps visible light communications," *IEEE Photonics Technology letters*, vol. 28, no. 19, pp. 2023–2026, 2016.

[73] M. Islim, R. Ferreira, X. He, S. Videv, S. Viola, M. S. Islim, R. X. Ferreira, X. He, E. Xie, S. Videv, S. Viola, S. Watson, N. Bamiedakis, R. V. Penty, I. H. White, A. E. Kelly, E. Gu, H. Haas, and M. D. Dawson, "Towards 10 Gb/s OFDM-based Visible Ligth Communication using a GaN Violet micro-LED," *Photonics Research*, vol. 5, no. 2, pp. A35–A43, 2017.

[74] D. Tse and P. Viswanath, "Chapter 05: Capacity of wireless channels," in *Fundamentals of Wireless Communication.* Cambridge University Press, 2005, pp. 166–227.

[75] G. P. Agrawal, *Fiber-Optic Communications Systems, Third Edition.* Wiley, 2002, vol. 6.

[76] "Revolution wifi: How OFDM Subcarriers Work." [Online]. Available: http://www.revolutionwifi.net/revolutionwifi/2015/3/how-ofdm-subcarriers-work

[77] "Radio-electronics: Orthogonal frequency division multiplexing." [Online]. Available: http://www.radio-electronics.com/info/rf-technology-design/ofdm/ofdm-basics-tutorial.php

[78] W. Shieh and I. Djordjevic, *OFDM for optical communications.* Elsevier, 2009.

[79] X. Li, R. Mardling, J. Armstrong, and S. Member, "Channel Capacity of IM / DD Optical Communication Systems and of ACO-OFDM," in *IEEE International Conference on Communications*, vol. 1, 2007, pp. 2128–2133.

[80] I. Wegrzecka, M. Wegrzecki, and M. Grynglas, "Design and properties of silicon avalanche photodiodes," *Opto-Electronics Review*, vol. 12, no. 1, pp. 95–104, 2004. [Online]. Available: http://mes.wat.edu.pl/review/optor/12(1)95.pdf

[81] C. R. Belton, G. Itskos, G. Heliotis, P. N. Stavrinou, P. G. Lagoudakis, J. Lupton, S. Pereira, E. Gu, C. Griffin, B. Guilhabert, I. M. Watson, a. R. Mackintosh, R. a. Pethrick, J. Feldmann, R. Murray, M. D. Dawson, and D. D. C. Bradley, "New light from hybrid inorganic-organic emitters," *Journal of Physics D: Applied Physics*, vol. 41, no. 9, p. 094006, 2008. [Online]. Available: http://dx.doi.org/10.1088/0022-3727/41/9/094006{%}5Cnhttp://stacks.iop.org/0022-3727/41/i=9/a=094006?key=crossref.79846b7bc25f706340197f2bcc83997c

[82] S. Nizamoglu, G. Zengin, and H. V. Demir, "Color-converting combinations of nanocrystal emitters for warm-white light generation with high color rendering index," *Applied Physics Letters*, vol. 92, no. 3, p. 031102, 2008.

[83] H.-s. Kim, E. Brueckner, J. Song, Y. Li, S. Kim, C. Lu, J. Sulkin, K. Choquette, Y. Huang, R. G. Nuzzo, and J. a. Rogers, "Unusual strategies for using indium gallium nitride grown on silicon (111) for solid-state lighting," *Proceedings of the National Academy of Sciences*, vol. 108, no. 25, pp. 10 072–10 077, 2011. [Online]. Available: http://www.pnas.org/cgi/doi/10.1073/pnas.1102650108

[84] M. a. Meitl, Z.-T. Zhu, V. Kumar, K. J. Lee, X. Feng, Y. Y. Huang, I. Adesida, R. G. Nuzzo, and J. a. Rogers, "Transfer printing by kinetic control of adhesion to an elastomeric stamp," *Nature Materials*, vol. 5, no. 1, pp. 33–38, 2006.

[85] E. Menard, K. J. Lee, D. Y. Khang, R. G. Nuzzo, and J. A. Rogers, "A printable form of silicon for high performance thin film transistors on plastic substrates," *Applied Physics Letters*, vol. 84, no. 26, pp. 5398–5400, 2004.

[86] D. Kang, B. Gai, B. Thompson, S. M. Lee, N. Malmstadt, and J. Yoon, "Flexible Opto-Fluidic Fluorescence Sensors Based on Heterogeneously Integrated Micro-VCSELs and Silicon Photodiodes," *ACS Photonics*, vol. 3, no. 6, pp. 912–918, 2016.

[87] M. Armstrong, C. O'Dwyer, W. Macklin, and J. Holmes, "Evaluating the performance of nanostructured materials as lithium-ion battery electrodes," *Nano Research*, vol. 7, pp. 1–62, 2014. [Online]. Available: http://link.springer.com/article/10.1007/s12274-013-0375-x

[88] T. I. Kim, S. Hyun Lee, Y. Li, Y. Shi, G. Shin, S. D. Lee, Y. Huang, J. A. Rogers, and J. Su Yu, "Temperature- and size-dependent characteristics in ultrathin inorganic light-emitting diodes assembled by transfer printing," *Applied Physics Letters*, vol. 104, no. 5, p. 051901, 2014.

[89] S.-I. Park, Y. Xiong, R.-H. Kim, P. Elvikis, M. Meitl, D.-H. Kim, J. Wu, J. Yoon, C.-J. Yu, Z. Liu, Y. Huang, K.-c. Hwang, P. Ferreira, X. Li, K. Choquette, and J. A. Rogers, "Printed assemblies of inorganic light-emitting diodes for deformable and semitransparent displays." *Science (New York, N.Y.)*, vol. 325, no. 5943, pp. 977–81, 2009. [Online]. Available: http://science.sciencemag.org/content/325/5943/977.abstract

[90] T.-i. Kim, J. G. Mccall, Y. H. Jung, X. Huang, R. Edward, Y. Li, J. Song, Y. M. Song, H. A. Pao, R.-h. Kim, C. Lu, S. D. Lee, I.-s. Song, G. C. Shin, R. Al-hasani, and S. Louis, "Injectable, Cellular-scale Optoelectronics with Applications for Wireless Optogenetics," *NIH Public Access*, vol. 340, no. 6129, pp. 211–216, 2014.

[91] T.-h. Kim, K.-s. Cho, E. K. Lee, S. J. Lee, J. Chae, J. W. Kim, D. H. Kim, J.-y. Kwon, G. Amaratunga, S. Y. Lee, B. L. Choi, Y. Kuk, J. M. Kim, and K. Kim, "Full-color quantum dot displays fabricated by transfer printing," *Nature Photonics*, vol. 5, no. February, pp. 176–182, 2011. [Online]. Available: http://dx.doi.org/10.1038/nphoton.2011.12

[92] A. De Groote, P. Cardile, A. Z. Subramanian, A. M. Fecioru, C. Bower, D. Delbeke, R. Baets, and G. Roelkens, "Transfer-printing-based integration of single-mode waveguide-coupled III-V-on-silicon broadband light emitters,"

Optics Express, vol. 24, no. 13, pp. 13 754–13 762, 2016. [Online]. Available: https://www.osapublishing.org/abstract.cfm?URI=oe-24-13-13754

[93] R. Loi, J. O'Callaghan, B. Roycroft, C. Robert, A. Fecioru, A. J. Trindade, A. Gocalinska, E. Pelucchi, C. A. Bower, and B. Corbett, "Transfer Printing of AlGaInAs/InP Etched Facet Lasers to Si Substrates," *IEEE Photonics Journal*, vol. 8, no. 6, pp. 1–10, 2016. [Online]. Available: http://ieeexplore.ieee.org/document/7742401/

[94] A. J. Trindade, B. Guilhabert, D. Massoubre, D. Zhu, N. Laurand, E. Gu, I. M. Watson, C. J. Humphreys, and M. D. Dawson, "Nanoscale-accuracy transfer printing of ultra-thin AlInGaN light-emitting diodes onto mechanically flexible substrates," *Applied Physics Letters*, vol. 103, no. 25, p. 253302, 2013.

[95] A. J. Trindade, B. Guilhabert, E. Y. Xie, R. Ferreira, J. J. D. McKendry, D. Zhu, N. Laurand, E. Gu, D. J. Wallis, I. M. Watson, C. J. Humphreys, and M. D. Dawson, "Heterogeneous integration of gallium nitride light-emitting diodes on diamond and silica by transfer printing." *Optics express*, vol. 23, no. 7, pp. 9329–9338, 2015. [Online]. Available: http://www.scopus.com/inward/record.url?eid=2-s2.0-84928024638{%}7B{&}{%}7DpartnerID=tZOtx3y1

[96] B. Guilhabert, A. Hurtado, D. Jevtics, Q. Gao, H. H. Tan, C. Jagadish, and M. D. Dawson, "Transfer Printing of Semiconductor Nanowires with Lasing Emission for Controllable Nanophotonic Device Fabrication," *ACS Nano*, p. acsnano.5b07752, 2016. [Online]. Available: http://pubs.acs.org/doi/abs/10.1021/acsnano.5b07752

[97] M. B. Tucker, D. R. Hines, and T. Li, "A quality map of transfer printing," *Journal of Applied Physics*, vol. 106, no. 10, p. 103504, 2009.

[98] M. Shikida, K. Sato, K. Tokoro, and D. Uchikawa, "Differences in anisotropic etching properties of KOH and TMAH solutions," *Sensors and Actuators, A: Physical*, vol. 80, no. 2, pp. 179–188, 2000.

[99] "Silicon solutions: RTV615A silicone rubber compound." [Online]. Available: https://www.momentive.com/products/show-technical-datasheet.aspx?id=10333

[100] C. A. Bower, D. Gomez, K. Lucht, B. Cox, and D. Kneeburg, "Transfer-Printed Integrated Circuits for Display Backplanes," *Applied Physics Letters*, vol. 1, pp. 1203–1206, 2010.

[101] J.-H. Ahn, H.-S. Kim, K. J. Lee, S. Jeon, S. J. Kang, Y. Sun, R. G. Nuzzo, and J. A. Rogers, "Heterogeneous Three-Dimensional Electronics by Use of Printed Semiconductor Nanomaterials," *Science*, vol. 314, no. 5806, pp. 1754–1757, 2006. [Online]. Available: http://www.sciencemag.org/cgi/doi/10.1126/science.1132394

[102] Zeiss, "Zeiss: Mercury Arc Lamps," 2017. [Online]. Available: http://zeiss-campus.magnet.fsu.edu/articles/lightsources/mercuryarc.html

[103] "PECVD - Oxford Instruments." [Online]. Available: https://www.oxford-instruments.com/products/etching-deposition-and-growth/plasma-etch-deposition/pecvd

[104] J. Foggiato, "Handbook of thin film deposition," in *Handbook of thin film deposition*, 2nd ed., K. Seshan, Ed. Elsevier, 2001

[105] S. Franssila, *Introduction to Microfabrication*. Wiley, 2010.

[106] "Reactive Ion Etching (RIE): Oxford Instruments." [Online]. Available: https://www.oxford-instruments.com/products/etching-deposition-and-growth/plasma-etch-deposition/rie

[107] "Inductively Coupled Plasma (ICP) Etching : Oxford Instruments." [Online]. Available: https://www.oxford-instruments.com/products/etching-deposition-and-growth/plasma-etch-deposition/icp-etch

[108] "Semiconductor Doping Technology." [Online]. Available: http://www.iue.tuwien.ac.at/phd/wittmann/node7.html

[109] R. E. Oosterbroek, J. W. Berenschot, H. V. Jansen, A. J. Nijdam, G. Pandraud, A. Van Den Berg, and M. C. Elwenspoek, "Etching methodologies in [111]-oriented silicon wafers," *Journal of Microelectromechanical Systems*, vol. 9, no. 3, pp. 390–398, 2000.

[110] "Brigham Young University: KOH Etching of Silicon wafers, Silicon Dioxide (SiO2) and Silicon Nitride (SiN)." [Online]. Available: http://www.cleanroom.byu.edu/KOH.phtml

[111] L. T. Romano, C. G. Van de Walle, J. W. Ager, W. Gotz, and R. S. Kern, "Effect of Si doping on strain, cracking, and microstructure in GaN thin films grown by metalorganic chemical vapor deposition," *Journal of Applied Physics*, vol. 87, no. 11, p. 7745, 2000. [Online]. Available: http://link.aip.org/link/JAPIAU/v87/i11/p7745/s1{&}Agg=doi

[112] Y. Fu, D. a. Gulino, and R. Higgins, "Residual stress in GaN epilayers grown on silicon substrates," *Journal of Vacuum Science & Technology A: Vacuum, Surfaces, and Films*, vol. 18, p. 965, 2000.

[113] "Fiber Cabling Solution: WDM Archives." [Online]. Available: http://www.fiber-optic-cable-sale.com/tag/wdm

[114] X. Li, N. Bamiedakis, J. Mckendry, E. Xie, R. Ferreira, E. Gu, M. Dawson, R. Penty, and I. H. White, "11 Gb/s WDM Transmission Over SI-POF Using Violet, Blue and Green μLEDs," *Optical Fiber Communication Conference*, p. Tu2C.5, 2016. [Online]. Available: http://www.osapublishing.org/abstract.cfm?uri=OFC-2016-Tu2C.5

[115] N. Bamiedakis, X. Li, R. V. Penty, S. Member, and I. H. White, "High-Aggregate-Capacity Guided-Wave Visible Light Communication Links," in *Conference on Transparent Optical Networks*, 2016, pp. 8–11.

[116] Y. Wang, X. Huang, L. Tao, J. Shi, and N. Chi, "45-Gb/s RGB-LED based WDM visible light communication system employing CAP modulation and RLS based

adaptive equalization," *Optics Express*, vol. 23, no. 10, p. 13626, 2015. [Online]. Available: https://www.osapublishing.org/abstract.cfm?URI=oe-23-10-13626

[117] Y. Pei, S. Zhu, H. Yang, L. Zhao, X. Yi, J. Junxi Wang, and J. Li, "LED Modulation Characteristics in a Visible-Light Communication System," *Optics and Photonics Journal*, vol. 03, no. 02, pp. 139–142, 2013. [Online]. Available: http://www.scirp.org/journal/PaperDownload.aspx?DOI=10.4236/opj.2013.32B034

[118] Osram, http://www.osram-os.com/osram{_}os/en/news--events/spotlights/technology/2016/lab-news-rare-earth-reduced-white-leds/index.jsp

[119] P. lumiled, "Lumileds: Phosphors," 2017. [Online]. Available: http://www.lumileds.com/technology/luxeon-technology/phosphor

[120] C. B. Murray, C. R. Kagan, and M. G. Bawendi, "Synthesis and Characterisation of Monodisperses Nanocrystals and Close-Packed Nanocrystal Assemblies," *Annual Review of Materials Science*, vol. 30, pp. 545–610, 2000.

[121] X. Lan, S. Masala, and E. H. Sargent, "Charge-extraction strategies for colloidal quantum dot photovoltaics," *Nat Mater*, vol. 13, no. 3, pp. 233–240, 2014. [Online]. Available: http://www.ncbi.nlm.nih.gov/pubmed/24553652

[122] A. Efros and A. Efros, "Interband absorption of light in a semiconductor sphere," *SPIE milestone series*, vol. 180, pp. 71–74, 1982. [Online]. Available: http://cat.inist.fr/?aModele=afficheN{&}cpsidt=18785991

[123] D. A. B. Miller and T. B. Laboratories, "Optical Physics of Quantum Wells," *Quantum Dynamics of Simple Systems*, pp. 239–266, 1996. [Online]. Available: http://www-ee.stanford.edu/{~}dabm/181.pdf

[124] "Will quantum dots make for a brighter future?" [Online]. Available: http://www.renishaw.com/en/will-quantum-dots-make-for-a-brighter-future--38605

[125] J. Q. Grim, L. Manna, and I. Moreels, "A sustainable future for photonic colloidal nanocrystals," *Chem. Soc. Rev.*, vol. 44, no. 16, pp. 5897–5914, 2015. [Online]. Available: http://xlink.rsc.org/?DOI=C5CS00285K

[126] B. O. Dabbousi, J. Rodriguez-Viejo, F. V. Mikulec, J. R. Heine, H. Mattoussi, R. Ober, K. F. Jensen, and M. G. Bawendi, "(CdSe)ZnS CoreShell Quantum Dots: Synthesis and Characterization of a Size Series of Highly Luminescent Nanocrystallites," *The Journal of Physical Chemistry B*, vol. 101, no. 46, pp. 9463–9475, 1997. [Online]. Available: http://pubs.acs.org/doi/abs/10.1021/jp971091y

[127] M. A. Hines and P. Guyot-Sionnest, "Synthesis and Characterization of Strongly Luminescing ZnS-Capped CdSe Nanocrystals," *The Journal of Physical Chemistry*, vol. 100, no. 2, pp. 468–471, 1996. [Online]. Available: http://pubs.acs.org/doi/abs/10.1021/jp9530562

[128] C. B. Murray, D. J. Norris, and M. G. Bawendi, "Synthesis and characterization of nearly monodisperse CdE (E = sulfur, selenium, tellurium) semiconductor nanocrystallites," *Journal of the American Chemical Society*, vol. 115, no. 19, pp. 8706–8715, 1993. [Online]. Available: http://pubs.acs.org/doi/abs/10.1021/ja00072a025

[129] B. Guilhabert, D. Elfström, A. J. C. Kuehne, D. Massoubre, H. X. Zhang, S. R. Jin, A. R. Mackintosh, E. Gu, R. A. Pethrick, and M. D. Dawson, "Integration by self-aligned writing of nanocrystal/epoxy composites on InGaN micro-pixelated light-emitting diodes." *Optics express*, vol. 16, no. 23, pp. 18 933–18 941, 2008.

[130] C. Foucher, B. Guilhabert, N. Laurand, and M. D. Dawson, "Wavelength-tunable colloidal quantum dot laser on ultra-thin flexible glass," *Applied Physics Letters*, vol. 104, no. 14, pp. 1–5, 2014. [Online]. Available: http://dx.doi.org/10.1063/1.4871372

[131] B. Guilhabert, C. Foucher, a M Haughey, E. Mutlugun, Y. Gao, J. Herrnsdorf, H. D. Sun, H. V. Demir, M. D. Dawson, and N. Laurand, "Nanosecond colloidal

quantum dot lasers for sensing." *Optics express*, vol. 22, no. 6, pp. 7308–19, 2014. [Online]. Available: http://www.ncbi.nlm.nih.gov/pubmed/24664078

[132] J. M. Santos, M. Leitao, C. Foucher, S. Rajbhandari, H. Chun, D. Vithanage, and B. Guilhabert, "Fast colour conversion of InGaN sources using semiconductor nanocrystals," in *UK Nitrides Consortium*, vol. 1, 2016, pp. 10–11.

[133] Z. L. Liau, "Semiconductor wafer bonding via liquid capillarity," *Applied Physics Letters*, vol. 77, no. 5, pp. 651–653, 2000. [Online]. Available: http://scholar.google.com/scholar?hl=en{&}btnG=Search{&}q=intitle:Semiconductor+wafer+bonding+via+liquid+capillarity{#}0

[134] B. E. Jones, P. J. Schlosser, J. De Jesus, T. A. Garcia, M. C. Tamargo, and J. E. Hastie, "Processing and characterisation of II-VI ZnCdMgSe thin film gain structures," *Thin Solid Films*, vol. 590, pp. 84–89, 2015. [Online]. Available: http://dx.doi.org/10.1016/j.tsf.2015.07.013

[135] J. M. M. Santos, B. E. Jones, P. J. Schlosser, S. Watson, J. Herrnsdorf, B. Guilhabert, J. J. D. McKendry, J. De Jesus, T. A. Garcia, M. C. Tamargo, A. E. Kelly, J. E. Hastie, N. Laurand, and M. D. Dawson, "Hybrid GaN LED with capillary-bonded IIVI MQW color-converting membrane for visible light communications," *Semiconductor Science and Technology*, vol. 30, no. 3, p. 035012, 2015. [Online]. Available: http://stacks.iop.org/0268-1242/30/i=3/a=035012?key=crossref.bcec2903108c087e85a3d6ef9da2be4d

[136] Z. Gong, S. Jin, Y. Chen, J. McKendry, D. Massoubre, I. M. Watson, E. Gu, and M. D. Dawson, "Size-dependent light output, spectral shift, and self-heating of 400 nm InGaN light-emitting diodes," *Journal of Applied Physics*, vol. 107, no. 1, p. 013103, 2010.

[137] "Mark optics: Specification Physical and chemical properties." [Online]. Available: http://www.markoptics.com/files/SchottAF32ecoPCP.pdf

[138] M. F. Leitao, J. M. M. Santos, B. J. E. Guilhabert, S. Watson, A. E. Kelly, M. S. Islim, H. Haas, M. D. Dawson, and N. Laurand, "Gb/s Visible Light

Communications with Colloidal Quantum Dot Color Converters," *IEEE Journal of Selected Topics in Quantum Electronics*, pp. 1–1, 2017. [Online]. Available: http://ieeexplore.ieee.org/document/7907282/

[139] "Laser components." [Online]. Available: https://www.lasercomponents.com/de/?embedded=1{&}file=fileadmin/user{_}upload/home/Datasheets/femto/photoreciever/hsa-x-s-1g4-si.pdf{&}no{_}cache=1

[140] "SensL: MicroFJ-SMA-300XX APD." [Online]. Available: http://sensl.com/estore/microfj-sma-300xx/

[141] C. Foucher, "Colloidal quantum dot with flex-glass encapsulation as color-converter for micro-LED source in visible light communications - KnowledgeBase, University of Strathclyde."

[142] "Hamamatsu Photonics: Si APD." [Online]. Available: http://www.hamamatsu.com/jp/en/product/category/3100/4003/4110/index.html

[143] P. P. Manousiadis, S. Rajbhandari, R. Mulyawan, D. A. Vithanage, H. Chun, G. Faulkner, D. O'Brien, G. A. Turnbull, S. Collins, and I. D. W. Samuel, "Wide field-of-view fluorescent antenna for visible light communications beyond the étendue limit," *Optica*, vol. 3, no. 7, pp. 702–706, 2016.

[144] T. Peyronel, K. J. Quirk, S. C. Wang, and T. G. Tiecke, "Luminescent detector for free-space optical communication," *Optica*, vol. 3, no. 7, pp. 787–792, 2016. [Online]. Available: http://www.osapublishing.org/optica/abstract.cfm?URI=optica-3-7-787

[145] H. Chun, P. Manousiadis, S. Rajbhandari, D. a. Vithanage, G. Faulkner, D. Tsonev, J. J. D. McKendry, S. Videv, E. Xie, E. Gu, M. D. Dawson, H. Haas, G. a. Turnbull, I. D. W. Samuel, and D. C. O'Brien, "Visible Light Communication Using a Blue GaN LED and Fluorescent Polymer Color Converter," *IEEE Photonics Technology Letters*, vol. 26, no. 20, pp. 2035–2038, 2014. [Online]. Available: http://ieeexplore.ieee.org/lpdocs/epic03/wrapper.htm?arnumber=6871350

[146] D. Tsonev, H. Chun, S. Rajbhandari, J. J. D. McKendry, S. Videv, E. Gu, M. Haji, S. Watson, A. E. Kelly, G. Faulkner, M. D. Dawson, H. Haas, and D. O'Brien, "A 3-Gb/s Single-LED OFDM-Based Wireless VLC Link Using a Gallium Nitride <formula formulatype="inline"> <img src="/images/tex/21416.gif" alt="\mu{\rm LED}"> </formula>," *IEEE Photonics Technology Letters*, vol. 26, no. 7, pp. 637–640, 2014.

[147] R. Lerner, S. Eisenbrandt, S. Bonafede, M. A. Meitl, A. Fecioru, A. J. Trindade, R. Reiner, P. Waltreit, and C. A. Bower, "Heterogeneous Integration of Microscale Gallium Nitride Transistors by Micro-Transfer-Printing," *Proceedings - Electronic Components and Technology Conference*, vol. 2016-Augus, no. c, pp. 1186–1189, 2016.

[148] S. Rajbhandari, H. Chun, G. Faulkner, K. Cameron, V. N. Jalajakumari, R. Henderson, D. Tsonev, M. Ijaz, Z. Chen, H. Haas, E. Xie, J. J. D. Mckendry, E. Gu, M. D. Dawson, and D. O. Brien, "R1.High-Speed Integrated Visible Light Communication System : Device Constraints and Design Considerations," *IEEE Journal on Selected Areas in Communications*, vol. 33, no. 9, pp. 1750–1757, 2016.

[149] S. Zhang, S. Watson, J. J. D. McKendry, D. Massoubre, A. Cogman, E. Gu, R. K. Henderson, A. E. Kelly, and M. D. Dawson, "1.5 Gbit/s multi-channel visible light communications using CMOS-controlled GaN-based LEDs," *Journal of Lightwave Technology*, vol. 31, no. 8, pp. 1211–1216, 2013.

[150] N. McAlinden, D. Massoubre, E. Richardson, E. Gu, S. Sakata, M. D. Dawson, and K. Mathieson, "Thermal and optical characterization of micro-LED probes for in vivo optogenetic neural stimulation." *Optics letters*, vol. 38, no. 6, pp. 992–4, 2013. [Online]. Available: http://www.ncbi.nlm.nih.gov/pubmed/23503284

Publications and Presentations

Publications

June 2017

InGaN micro-LEDs integrated onto colloidal quantum dot functionalised ultra-thin glass
K. Rae, C.Foucher, B. Guilhabert, M. S. Islim, L. Yin, D. Zhu, D. J. Wallis, R. A. Oliver, N. Laurand, and M. D. Dawson, Optics Express, vol. 16, pp.19179-19184, August 2017.

December 2017

Visible light communications integrated transceiver fabricated by transfer printing
K. Rae, P. Manousiadis, M. S. Islim, L. Yin, N. Laurand, G. A. Turnbull, I. D. W. Samuel, H. Haas, and M. D. Dawson, Photonics Research, in preparation.

Conference Presentations

April 2015

Ultra-thin InGaN light-emitting diodes transfer printed onto polymer optical fibres
SIOE, Cardiff, UK

October 2015

Integrated dual-color InGaN light-emitting diode array through transfer printing

IEEE Photonics, Reston, Virginia, USA

June 2016

Integrated dual-color InGaN light-emitting diode array through transfer printing

UKNC Summer meeting, Sheffield, UK

September 2016

Nano-scale accuracy transfer printing of ultra-thin InGaN light-emitting diodes onto colloidal quantum dot colour-converters

IoP Photon '16, Leeds, UK

October 2016

InGaN micro-LEDs integrated onto an ultra-thin, colloidal quantum dot functionalized glass platform

IEEE Photonics, Waikoala, Hawaii, USA

November 2016

Transfer printed multi-color integrated devices for visible light communication applications

OSA Light, Energy and the Environment Congress, Leipzig, Germany